UNIVERSITY of CALIFORNIA
Santa Barbara

Understanding atomic disorder in polar and magnetic oxides

A Dissertation submitted in partial satisfaction of the
requirements for the degree

Doctor of Philosophy
in
Materials

by

Daniel P. Shoemaker

Committee in charge:

Professor Ram Seshadri, Chair
Doctor Anna Llobet
Professor Christopher J. Palmstrøm
Professor Susanne Stemmer
Professor Galen D. Stucky

December 2010

The dissertation of Daniel P. Shoemaker is approved.

Doctor Anna Llobet

Professor Christopher J. Palmstrøm

Professor Susanne Stemmer

Professor Galen D. Stucky

Professor Ram Seshadri, Committee Chair

December 2010

Understanding atomic disorder in polar and magnetic oxides

by

Daniel P. Shoemaker

for my family and friends

Acknowledgements

I would first like to thank Ram for his invaluable guidance over the last four years. My knowledge and research habits have changed completely since I arrived in Ram's group, and nearly all of it is in a positive direction. Those traits can probably be traced to Ram's infectious enthusiasm, and his desire to bring out the best in his students and open doors for them. When people compliment Ram on his body of work, he often responds "it's easy: I have the best students!" That may be true. If so, it a reflection of his tireless efforts to improve us, make us work independently, and spend our time on worthwhile projects while somehow retaining our sanity and happiness.

I must thank my family for their tireless love and support. The rides to school, science fair projects, and band practice have long since gone, but my life is built on that foundation and they are never far from my thoughts. It has been such a pleasure to have you visit me from time to time and see what a special place Santa Barbara has been.

Thank you Jenn for being my partner in adventure. I'm excited to see where the next chapter in life will take us and I'm amazed that I found such a great person to share it with me.

I would specifically like to thank Mike, Brent, Zeric, and Josh for being fan-

tastic friends. I could always count on our fellow incoming materials students Jim, Sam, John Day, and Roger to improve any party, cookout, or other fiesta. I could not have asked for a better group to accompany me through graduate school.

My fellow Illinois alumni Eric Pressly, Shawn Mack, and Mark Nowakowski are all partially responsible for my decision to come to UCSB. So too was Ryan Haggerty. Shawn and Mark, thanks for hosting me when I first arrived homeless and for all the volleyball games. Thank you Lesa Banks, Michelle Dillard, Rebecca Richardson, and Myra Soderlund for convincing me that I could make science my career. Thank you Mike, Jasmine, Josh, Becca, Eric, Rob, Melissa, and Brad for company on snowy trips north.

The total scattering group at the Lujan Center provided invaluable assistance while I was in Los Alamos. Kate Page and Efrain Rodriguez took me under their wings and taught me everything about total scattering and how to navigate the bizarre landscape of Los Alamos. Anna Llobet, Thomas Proffen, and Joan Siewenie were always ready to answer my questions, fill out my paperwork, and help me with the instruments.

I must thank Tony and Maureen for making the MRL such a special place to work. Jamie Neilson and Josh Kurzman have been great friends and always

willing to tolerate my meandering thought process in scientific discussions. So too were my interns Maddie, Jenni, Ivana, and Stephanie. They were always eager to test my ideas, with seemingly no regard for the lack of results that often ensued. Joe Doyle has been a fantastic asset for all of us in the MRL. Without Joe, all of Ram's students would probably add a year to their graduate career.

I am endebted to Matt Tucker and Andrew Goodwin not only for their development of RMC software and technical support, but for their encouragement and generosity. Thank you Serena Corr for being a great friend and host during my visit to Canterbury. Thank you to Tom Bennett and the Cheetham group and Sam Chong and Robert Szczecinski and the Rosseinsky group for hosting me in Cambridge and Liverpool.

To everyone else, thank you for being part of the last four years.

Curriculum Vitæ

Daniel P. Shoemaker

Education

2006-2010	Ph.D. in Materials, University of California Santa Barbara, CA
2002-2006	B.S. (Honors) in Materials Science and Engineering, University of Illinois Urbana-Champaign, IL

Publications

10. D. P. Shoemaker, M. Tachibana, A. L. Hector, and R. Seshadri, *Working title:* Incoherent Bi off-centering in $Bi_2Ti_2O_6O'$ and $Bi_2Ru_2O_6O'$: Insulator versus metal. *(in preparation)* (2010)

9. J. R. Neilson, B. C. Melot, D. P. Shoemaker, J. Kurzman, R. Seshadri, and D. E. Morse, *Working title:* Understanding complex magnetic order through analyses of local atomic structure. *(in preparation)* (2010)

8. D. P. Shoemaker and R. Seshadri, Total scattering descriptions of local and cooperative distortions in the oxide spinel $Mg_{1-x}Cu_xCr_2O_4$ with dilute

Jahn-Teller ions. *(submitted)* (2010) arXiv:1008.5363

7. S. A. Corr, D. P. Shoemaker, B. C. Melot, and R. Seshadri, Real-space investigation of structural changes at the metal-insulator transition in VO_2, *Phys. Rev. Lett.* **105** (2010) 056404(1–4)

6. D. P. Shoemaker, A. L. Hector, C. J. Fennie, A. Llobet, Th. Proffen, and R. Seshadri, Atomic displacements in the charge ice pyrochlore $Bi_2Ti_2O_6O'$ studied by neutron total scattering, *Phys. Rev. B* **81** (2010) 144113(1–9) [Editor's Suggestion]

5. S. A. Corr, D. P. Shoemaker, E. S. Toberer, and R. Seshadri, Spontaneously formed porous and composite materials, *J. Mater. Chem.* **20** (2010) 1413–1422 [Feature article, cover art]

4. D. P. Shoemaker, E. E. Rodriguez, R. Seshadri, I. Sabaj Abumohor, and Th. Proffen, Intrinsic exchange bias in $Zn_xMn_{3-x}O_4$ ($x \leq 1$) solid solutions. *Phys. Rev. B* **80** (2009) 144422(1–9) [Editor's Suggestion]

3. D. P. Shoemaker, J. Li, and R. Seshadri, Unraveling atomic positions in an oxide spinel with two Jahn-Teller ions: Local structure investigation of $CuMn_2O_4$. *J. Am. Chem. Soc.* **131** (2009) 11450–11457

2. D. P. Shoemaker, S. A. Corr, and R. Seshadri, Porosity through reduction in metal oxides. *Mater. Res. Soc. Symp. Proc.* **1148E** (2009) PP10-01(1–8)

1. D. P. Shoemaker, M. Grossman, and R. Seshadri, Exchange biasing of single-domain Ni nanoparticles spontaneously grown in an antiferromagnetic MnO matrix. *J. Phys. Cond. Mat.* **20** (2008) 195219(1-9)

Abstract

Understanding atomic disorder in polar and magnetic oxides

by

Daniel P. Shoemaker

The functional properties of materials rely upon the composition, coordination, and connectivity of their constituent atoms. Understanding the atomic structure of condensed materials permits an understanding of how that structure influences macroscopic properties. The field of crystallography seeks to define the repeating lattice of periodic materials using a unit cell model with the minimum number of specified atomic positions. For magnetic and electronic materials, the arrangement of atoms and dipoles are often both ordered over long ranges and amenable to a traditional crystallographic description. However, interesting phenomena emerge when materials experience disorder due to chemical substitution, phase competition, nanostructuring, interfaces, or valence disproportionation. In those cases, the long-range symmetry of the material is interrupted and traditional crystallographic methods struggle to incorporate disorder into the unit cell model.

I will discuss how disorder can be identified and quantified in functional materials. Each study includes examination of the real-space pair distribution function (PDF), which provides a weighted histogram of all atom-atom distances in a sample. Models are created by simultaneous fits to the Bragg profile and the PDF, thereby constraining the atomic positions by reciprocal- and real-space scattering descriptions. The reverse Monte Carlo method drives stochastic fits to scattering data using tens of thousands of atoms. Once simulation is complete, crystallographic metrics can be extracted from the supercell in real space.

This approach is discussed in the case of site mixing and valence disproportionation in the Jahn-Teller active spinel $CuMn_2O_4$, local Jahn-Teller distortions of CuO_4 tetrahedra in the solid solution $Mg_{1-x}Cu_xCr_2O_4$, nanoscale phase coexistence at the metal-insulator transition in VO_2, and static displacements and lone-pair activity in the pyrochlores $Bi_2Ti_2O_6O'$ and $Bi_2Ru_2O_6O'$.

Contents

List of Figures

List of Tables

Chapter 1

Crystallography and atomic disorder

Materials science explores the interplay between atomic structure and properties. Understanding macroscopic properties, predicting new compounds, and engineering complex composites are all predicated on the assumption that the underlying atomic structure makes materials what they are. All condensed materials have structure, from liquids with weak van der Waals forces to diamond with a rigid covalent framework. The true location of $\sim 10^{23}$ atoms in a macroscopic material can never be known. Even in a nanoparticle with a small number of atoms, thermal motion prevents pinpointing their exact positions. Describ-

ing structure is therefore an exercise in approximation. This chapter discusses that approximation: the field of crystallography. Traditional crystallographic techniques provide excellent descriptions of materials that can be considered perfectly periodic. However, novel materials properties are often seen when phases possess chemical, displacive, or magnetic disorder. Structural dsecriptions of these materials require alternative means of characterization. To that end, methods of modeling materials using the reverse Monte Carlo (RMC) technique are introduced and the systematics of RMC simulations are outlined.

1.1 Introduction

The preamble to modern crystallography began in the seventeenth century, when Johannes Kepler and Robert Hooke proposed that snowflakes and crystals owed their faceted shapes to some internal ordering that shared the symmetry of the macroscopic solid. It was not until the early twentieth century that their theories were proven. In 1913, Max von Laue used X-ray diffraction to show that crystals consist of periodic arrangements of atoms [1] and was awarded the Nobel Prize in physics one year later. The X-ray diffractometer quickly emerged as the preferred method of investigating crystal structures because the wavelength of X-rays are on the order of atomic separations.

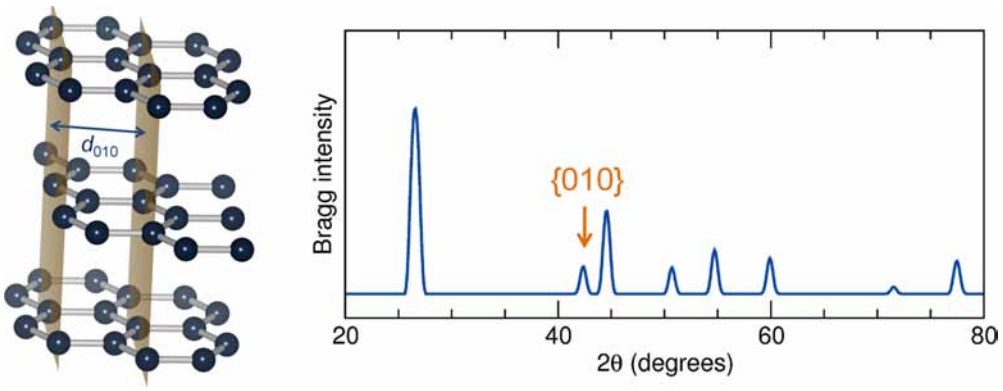

Figure 1.1: The calculated Bragg pattern of graphite (as would be measured by laboratory Cu-Kα X-ray diffraction) has peaks that correspond to inter-plane spacings in an infinitely periodic lattice.

Diffraction occurs by the interference of an incident wave with a periodic potential. A diffraction pattern is the Fourier transform of the scattering potential. The calculated diffraction pattern for graphite is shown in Figure 1.1, and the intensity is dominated by peaks of Bragg scattering. The Bragg peaks that are observed in reciprocal space arise from crystalline lattices that are effectively infinite in their extent compared to the wavelength of the X-ray. This is a key aspect of traditional crystallography. However, many crystalline materials are disordered over long ranges and their structure is not completely described by Bragg intensity. This chapter describes how Bragg analysis can be supplemented by local structure modeling.

1.2 Reciprocal-space crystallography

1.2.1 Crystalline structure, Bragg scattering, and Rietveld refinement

Crystals are periodic arrangements of atoms and are typically represented as infinitely tiled unit cells. This is an excellent way to characterize the structure of the the vast majority of crystalline materials. If an actual crystal closely approximates a perfectly periodic lattice, greater resolution is available from the diffraction pattern. For instance, the lattice parameter of Si at $T = 300$ K is known to be 5.4310206(1) Å, [2] and this precision arises because Si can be grown as more perfect crystals than any known substance. Periodicity is required by traditional crystallographic analysis and its requirement can often be a hindrance. For example, the structure of DNA was discovered only after it had been prepared in a crystalline form. [3]

The diffraction patterns of crystalline materials contain Bragg peaks that can be indexed to particular lattice planes. Rietveld refinement is performed by using a least-squares algorithm to create a model that produces the same Bragg intensity as a measured diffraction pattern. [4] The refined unit cell of $Bi_2Ti_2O_6O'$ is shown next to its fit to the low-temperature neutron diffraction pattern in

Fig. 1.2.(a,b). The tendency of Bi^{3+} to displace from its ideal position gives $Bi_2Ti_2O_6O'$ positional disorder that cannot be described by simply constructing a unit cell and tiling it infinitely. The crystallographer can choose from numerous methods to model this disorder.

1.2.2 Disorder in crystals

In traditional reciprocal-space Rietveld analysis, positional disorder on a crystallographic site is described by an atomic displacement parameter (ADP). Each unique atom in the unit cell is assigned ADPs that model the mean squared displacement from the ideal site. For a given atomic position in a standard crystal structure the ADPs are the only parameters that describe the positional disorder. Their form is typically of the tensors U_{ij}, which define an ellipsoid of probability density of finding the atom at a certain position near the site. The effect of changing ADPs in a model of pyrochlore $Bi_2Ti_2O_6O'$ is shown in Figure 1.2. The Rietveld-refined structure in (a) has anisotropic ADPs of $U_{11} = U_{22} = U_{33} =$ 0.092 Å^2 and $U_{12} = U_{13} = U_{23} = -0.044$ Å^2. The fit to neutron diffraction data in (b) is very good. If the ADPs are ignored, the unit cell would appear as in (c), where all atoms have $U_{iso} = 0.008$ Å^2. This model incorrectly approximates the atomic disorder, so the Bragg peak intensities are mismatched and the fit in (d)

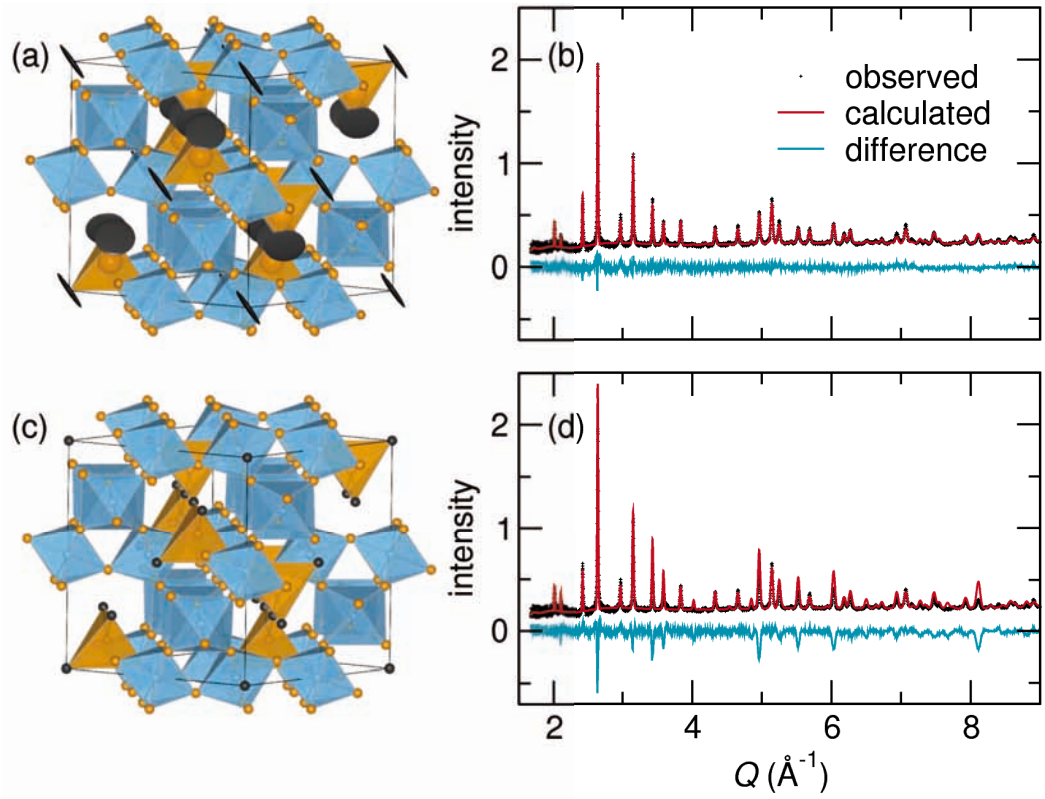

Figure 1.2: The $Bi_2Ti_2O_6O$ unit cell at 14 K is shown in (a) with ellipsoids representing ADPs obtained from Rietveld re nement to neutron di raction in (b). If these ADPs are ignored so that all atoms have $U_{iso} = 0\ 008$ A^2, the unit cell (c) produces a Bragg pattern with incorrect peak intensities (d).

worsens.

In materials where thermal vibrations are the only form of disorder, atoms are often isotropically disordered around their ideal position and all ADPs tend to be similar. In that case, the Rietveld-refined model of the crystal structure provides a sufficient description of the crystal structure. Complex materials such as $Bi_2Ti_2O_6O'$, where lattice instabilities cause static or dynamic displacements, are not always this well-behaved and merit further investigation. Their disorder can take many forms: thermal vibrations, compositional mixing, static or dynamic displacements, mixed valence, phase competition, finite grain size, etc.

1.2.3 Atomic displacements and diffuse scattering

In functional materials, structural degrees of freedom are tied to useful macroscopic properties: electronic and magnetic susceptibility, optical response, and mechanical behavior. These degrees of freedom arise from many underlying causes and can be tuned to engineer their respective properties. Their instability leads to disorder, and the deviation from the ideal, average crystal structure is often more complex than ellipsoidal ADPs can accommodate. The average atomic site may be a different shape than an ellipsoid, may be ordered over long length scales, or may be incoherent over long ranges. At this point, it becomes helpful

to step away from the infinitely long-range-ordered average model and move to a real-space, atom's-eye point of view.

Rather than the using the Bragg approximation to calculate the scattering profile of a material (where relevant scattered intensity comes from lattice plane spacings), the Debye equation [5] can be used to construct a diffraction pattern from each distinct atom in a material:

$$I_{powder}(Q) = \sum_{i=1}^{N} \sum_{j=1}^{N} f_i(Q) f_j(Q) \frac{sin(Qr_{ij})}{Qr_{ij}} \tag{1.1}$$

Where Q is the scattering momentum transfer, r_{ij} are distances between atoms with scattering cross-sections $f_i(Q)$–effectively a combination of each scattered wave interfering with each other. This implies that all pairwise interactions contribute to the scattered intensity, not simply the ones that are contributing most of their intensity to Bragg peaks. Diffuse scattering from disordered motifs, whether correlated over short ranges or not, is included here. The diffuse scattering rarely approaches Bragg scattering in peak intensity but it is often present in comparable amounts when integrated with respect to Q.

There is no more direct method than equation 1.1 to calculate the diffuse intensity profile from a model. However, a single unit cell does not provide enough pairs to create a reasonably precise diffuse profile. Indeed, many con-

tributions to diffuse scattering, such as the preference for clustering of nearest neighbors, are quantities that describe the relations *between* atoms over some length scale; they are not properties that can be easily defined by small boxes. Early work on fitting models to X-ray diffuse scattering relied on using mathematical descriptions of disorder to create longer-ranged autocorrelation functions that could be Fourier transformed. [6] In the 1980s, increased computing power led to the ability to model larger atomic configurations in computer simulations, and stochastic methods of modeling the disordered contributions to crystal structures were developed. [7]

1.3 Real space analysis and the pair distribution function

In the presence of atomic disorder that is not easily incorporated into the unit cell, the only way to calculate the diffuse intensity in $I(Q)$ is to use the Debye equation. If any appreciable resolution is desired in reciprocal space, a very large (tens or hundreds of thousands of atoms) supercell needs to input in equation 1.1. Instead fitting reciprocal-space scattering data with a real-space model, we can Fourier transform the data to allow modeling and fits to be performed in real

space. The result is the pair distribution function (PDF): a real-space histogram of atom-atom distances.

1.3.1 PDF systematics

After subtracting background intensity from the measured $I(Q)$ of a scattering experiment, normalization by the total cross section of the sample gives the structure factor $S(Q)$. The structure factor is the Fourier transformation of the scattering potential, so Fourier transformation of S(Q) gives the scattering potential (electron density for X-rays or nuclear density for neutrons) in real space:

$$G(r) = \frac{2}{\pi} \int_0^\infty Q[S(Q) - 1] \sin(Qr)\, dQ \tag{1.2}$$

The PDF (historically denoted as $G(r)$, the radial distribution function, or a one-dimensional Patterson function) provides a histogram of all atom-atom distances in a sample, weighted by scattering cross section, regardless of crystallinity. The measured $S(Q)$ and transformed PDF for $CuMn_2O_4$ are shown in Figure 1.3.

Two schematic PDFs are shown for graphene. The first (Figure 1.4) shows how the PDF is constructed outward from the central atom in the structure. Each nearest-neighbor shell produces one peak, weighted by the number of atoms at

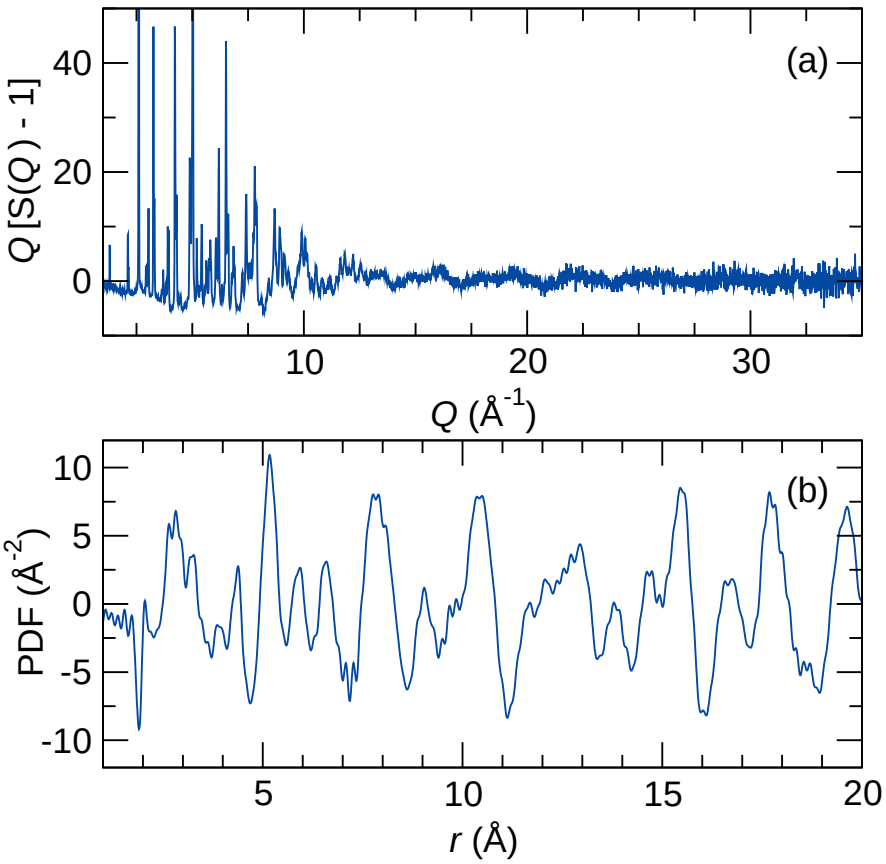

Figure 1.3: Time-of-flight neutron scattering $S(Q)$ and the Fourier transformed PDF for $CuMn_2O_4$. The first PDF peak (Mn–O) points downward because Mn has a negative neutron scattering cross section.

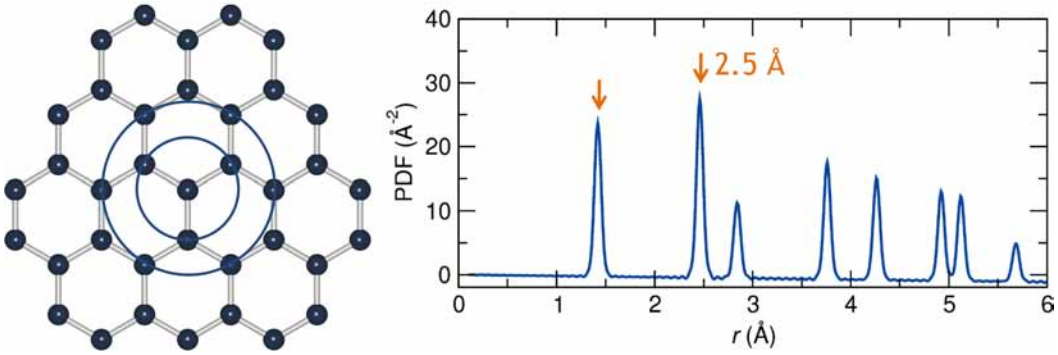

Figure 1.4: The PDF for a single sheet of graphene is shown schematically. From the central atom, two coordination circles are drawn, corresponding to the arrowed peaks in the PDF.

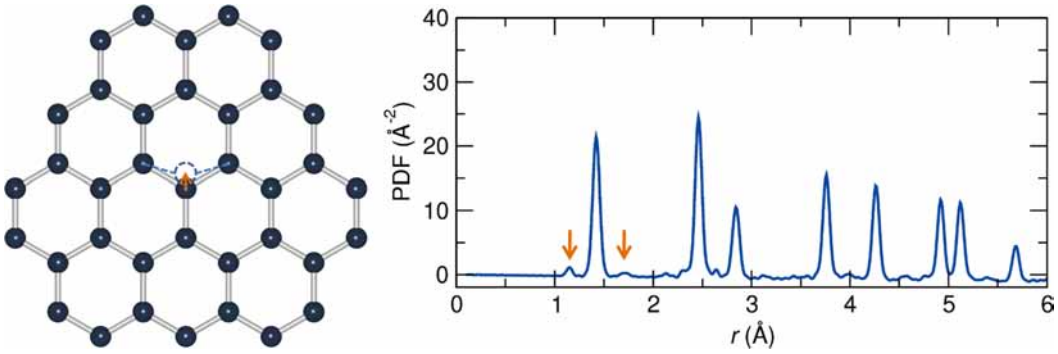

Figure 1.5: Displacing one atom causes should peaks to appear in the graphene PDF. The shorter-r peak is larger than the higher-r shoulder peak because there are two closer neighbors and only one farther. Higher-order peaks are also introduced.

that distance r. The second schematic (Figure 1.5) shows how atomic displacements produce directly-interpretable information in the PDF. When the central atom is moved upward, its new coordination environment has two short and one long nearest-neighbor bonds. These are seen as shoulder peaks in the PDF and their location gives the r distance of each bond.

The PDF is a Fourier transform of $S(Q)$ which includes both Bragg and diffuse contributions. Methods of modeling that account for both contributions are said to utilize "total scattering." Total scattering measurements require more care than traditional analysis because the diffuse intensity is no longer discarded as background. The instrumental background and container contribution must be constant over the course of measurement so that they can be subtracted. Because the PDF and $S(Q)$ are related by Fourier transformation, the resolution of $S(Q)$ determines how the PDF intensity attenuates with r (its extent) and the extent of $S(Q)$ determines the resolution of the PDF. The integral in equation 1.2 goes to $Q = \infty$, but in practice only finite Q values can be reached, so the PDF becomes:

$$G(r) = \frac{2}{\pi} \int_{Q_{min}}^{Q_{max}} Q[S(Q) - 1] \sin(Qr)\, dQ \tag{1.3}$$

For these reasons, the high resolution and high Q_{max} needed for extraction of a suitable PDF can only typically be achieved at spallation neutron or syn-

chrotron X-ray sources. Both types of data have been utilized in this work. X-ray measurements usually have Q_{max} = 20-25 Å^{-1}, while HIPD and NPDF at Los Alamos can reach Q_{max} = 35 Å^{-1}. This is in comparison to a laboratory Cu-Kα X-ray source which can only reach 2Θ = 120°, or a Q_{max} = 7 Å^{-1}.

Early collection of PDFs was restricted to work on liquids and glasses where even blurry (low Q_{max}), low-resolution information about the local coordination of atoms was valuable. The resolution and Q_{max} were not available to extract PDFs that contributed to the understanding of crystalline materials, which have sharp peaks persisting to high r in the PDF. However, with the advent of dedicated PDF beamlines at LANL, APS, and ISIS, higher-resolution PDFs are now available with short acquisition times (hours for neutrons and up to 10 Hz for X-rays) with sufficient resolution to see atomic displacements of around 0.01 Å.

1.3.2 Least-squares fits to the PDF

Widespread adoption of PDF analysis of crystalline materials in the past decade has been a result of rapid advances in not only instrumentation, but software. Data processing (which includes subtracting background runs to obtain a $S(Q)$ that can be Fourier transformed) is performed automatically by the PDFGETN [8] and GUDRUN programs for TOF neutron data collected at the

Lujan Center and ISIS, respectively, while PDFGETX2 [9] is used to process X-ray data from the APS. These programs are truly general-use, in the sense that the data reduction is performed using minimal details about the sample. Only its overall elemental composition and approximate density are necessary user inputs to the software. The transformation to PDF is not predicated on any prior structural knowledge.

Today, the most prolific form of PDF modeling is least-squares refinement using PDFGUI. [10] This software was designed to operate similarly to Rietveld refinement software, to speed adoption among crystallographers. In PDFGUI, neutron and X-ray PDFs can be loaded and fit using a single- or multiple-phase refinement. The structural models are often traditional unit cells (with periodic boundary conditions) with atoms in Wyckoff sites determined by the unit cell symmetry. Cell parameters, atom positions, and ADPs can be refined in the same manner as in the Rietveld method. The first logical step is to perform a fit to the PDF using the known, average structure from Rietveld refinement. If the average structure produces a good fit to the PDF, it can be assumed that the local structure is correctly described by the average structure. Further investigation of the PDF is therefore unlikely to provide any improvement from the Rietveld-refined average structure.

Figure 1.6 shows least-squares fits to the PDFs of Si and $CuMn_2O_4$. For Si,

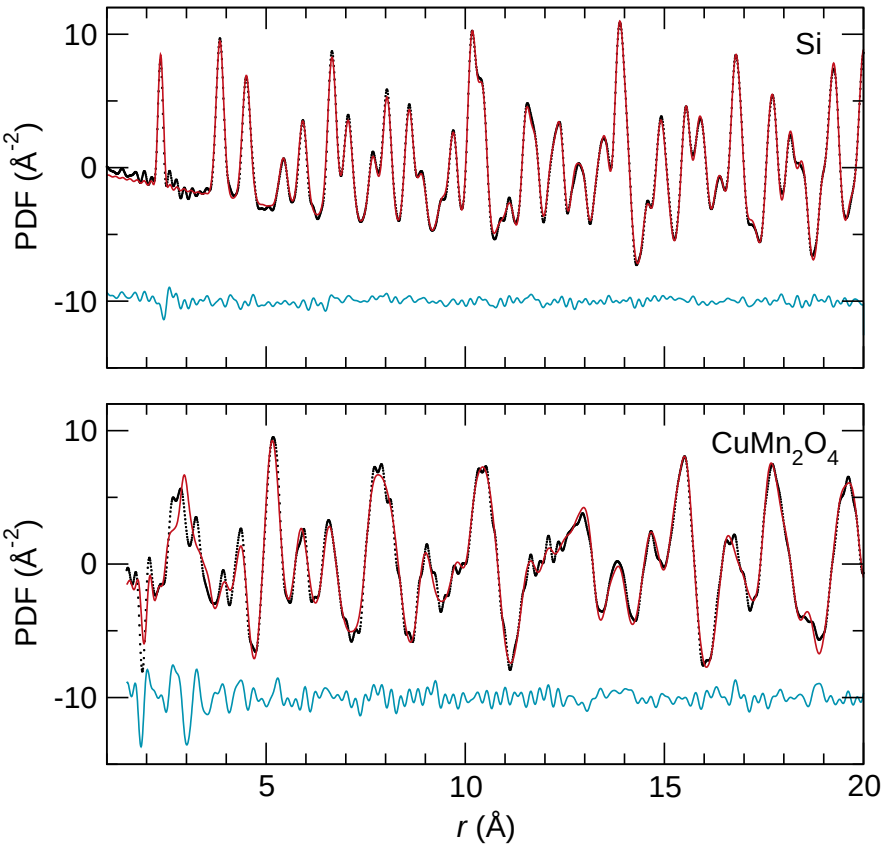

Figure 1.6: Room-temperature least-squares PDF refinements for Si and $CuMn_2O_4$. While Si is well-described by the Rietveld unit cell, $CuMn_2O_4$ has unfit peaks at low r.

the prototypical "average" structure, the fit is excellent. No additional structural information would likely be found during PDF analysis. $CuMn_2O_4$, on the other hand, has a poor fit at low r and a better fit at high r. This implies that the average structure does a reasonable job describing the structure as a whole, but does not include details of short-range M–O connectivity. The presence of chemical disorder and Jahn-Teller distortions in $CuMn_2O_4$ make it a candidate for further PDF analysis.

1.3.3 Difficulties with a prescriptive approach

When the average structure does not match the PDF, least-squares refinements offer routes to identify the local disorder. Atomic positions and thermal parameters can be allowed to refine, just as would be done in Rietveld refinements. Very large thermal parameters are a sign that more complex disorder may be present. When the fit to PDF is only performed over a short r intervals, this can uncover surprising structural details. In the case of $LaMnO_3$, (Figure 1.7) least-squares refinements over short r ranges show Jahn-Teller distortions that persist locally above the temperature where they disappear in the average structure. In this case, the low- and high-temperature structure appear identical when only short r ranges are used for the PDF refinement. This implies

that the shape of individual MnO_6 octahedra is always distorted. Heating above the Jahn-Teller transition does not alter the octahedra themselves, but it does disrupt the correlations between them.

This type of r-range-dependent fitting to the PDF (colloquially called "box-car refinement") is a powerful probe of the real-space coherence length of a structural distortion. It is easily performed as a macro in PDFGUI. This is the particular strength of least-squares refinement: When the local structure can be modeled *using a unit-cell description*, the method provides converged values of the structural parameters of that cell. It also finds the r range where the local and average structures disagree.

When the local structure is not immediately obvious, it may be necessary to employ larger models and search for the local structure. This is often the case when multiple forms of disorder (chemical, displacive, *etc.*) are present. Least-squares refinements typically do not allow complete relaxation of a large, complex structure because the refinement diverges when the number of free parameters becomes large.

Least-squares refinement of the PDF is therefore a prescriptive approach. A model must be made before it can be tested. This model needs to be close to the converged structure because least-squares algorithms are not designed to search

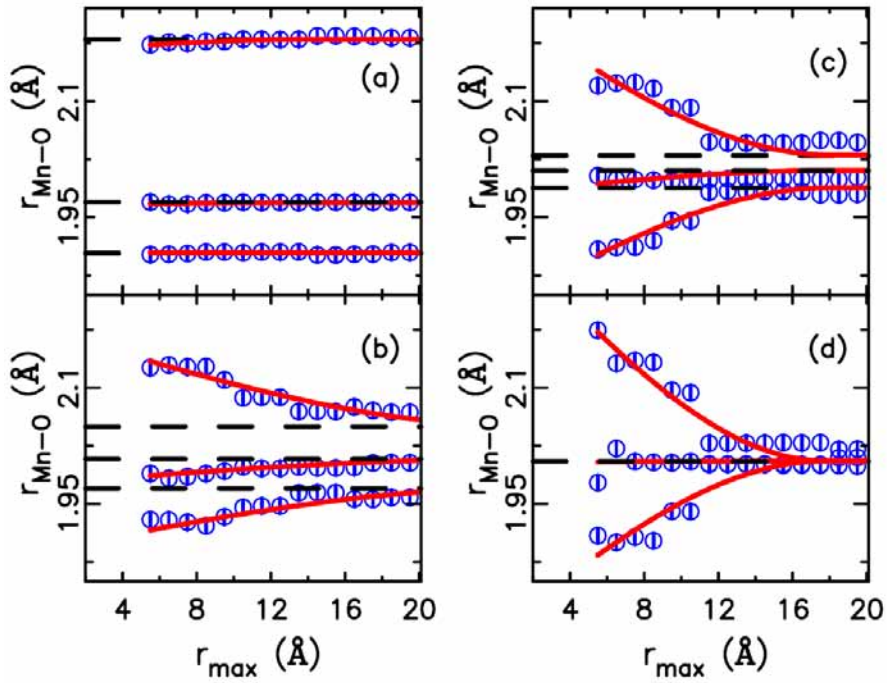

Figure 1.7: r-dependent least-squares fits to the PDF of $LaMnO_3$ show three different Mn–O bond lengths (indicating Jahn–Teller distortion) at (a) 300 K, (b) 740 K, (c) 800 K, (d) 1100 K. At low r all bond lengths are equal. Increasing temperature removes the correlation between them. Reproduced with permission from reference 11, © 2005 by the American Physical Society.

for a distant solution—only to locate in close proximity to the starting model. When the final answer is not obvious, devising and constructing a best-guess starting model can become very difficult and time-consuming. In this case, a technique that samples a larger parameter space becomes necessary.

1.4 Reverse Monte Carlo fits to the PDF

The reverse Monte Carlo (RMC) technique sidesteps the problem of determining an initial structural model. While least-squares fits are constrained by symmetry and typically have ten or fewer refined parameters, reverse Monte Carlo tends to be performed with no symmetry constraints and thousands of atoms. Truly a stochastic technique, RMC uses random numbers to sample large volumes of parameter space. Unlike traditional methods such as Rietveld, it does not give a single, "best agreement" structure. Instead, it produces many configurations that, taken as a whole, show tendencies that are supported by the data.

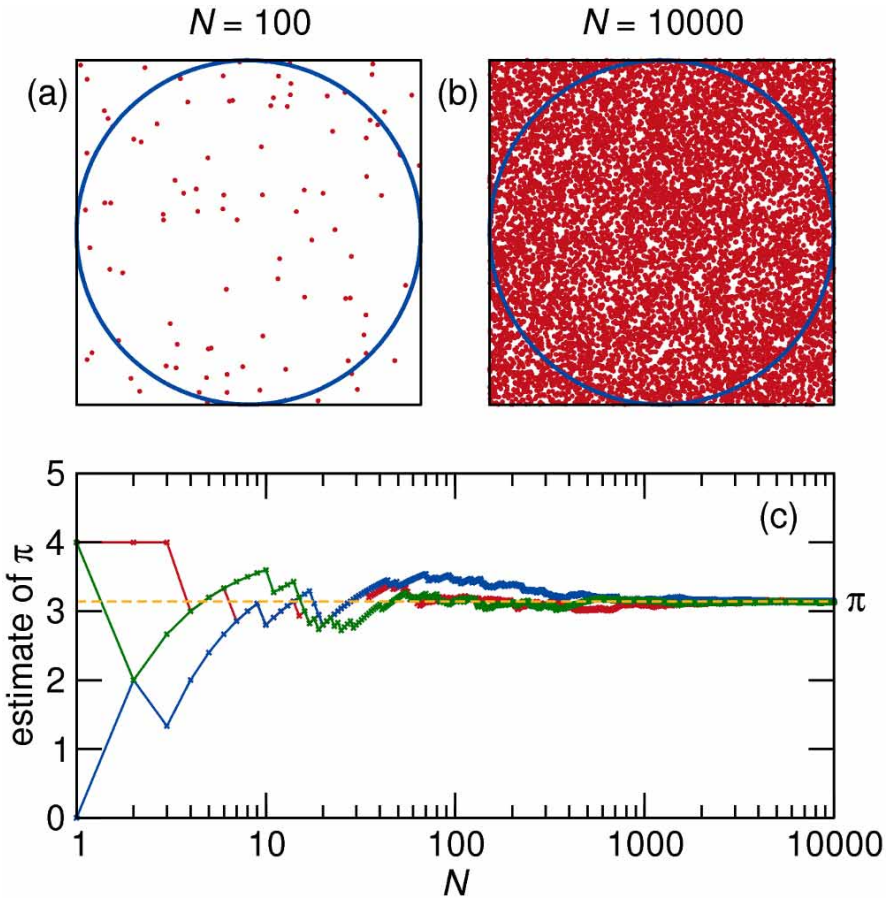

Figure 1.8: A Monte Carlo example to calculate an approximate value of π by placing stones in a box. An inexact value is given after $N = 100$, but by $N = 10000$ three independent runs give a reasonable estimate.

1.4.1 Background of the Monte Carlo method

One simple example of the Monte Carlo method is shown in Figure 1.8 and can be used to approximate the value of π. For a circle inscribed in a square, random points are chosen—"stones dropped into a box." The configuration after $N = 100$ stones is shown in Figure 1.8(a). The ratio of the areas of the circle to the square is $\frac{\pi}{4}$. Counting the fraction of stones in the box and multiplying by 4 gives an approximate value of π. This example continues to $N = 10000$, with the value of π plotted in Figure 1.8(c) after each step. At the end of the simulation, three independent MC runs return similar values of π.

This example highlights a few salient characteristics of Monte Carlo methods. First, the algorithm is stochastic, *i.e.* predicated on random events, and will produce a slightly different estimate of π every time. Second, the placement of stones must truly be random. Dropping stones only into the center of the box will give an incorrect estimate of π. As a result, Monte Carlo techniques were one of the first driving forces for truly random number generation. Third, the estimate of π improves as the number of stones becomes greater, shown by the convergence in Figure 1.8(c). Fourth, and very importantly, the simulation is never "finished." An exact value of π is never given, nor expected.

The application of Monte Carlo techniques to the physical sciences began

Enrico Fermi, John von Neumann, and Stanisław Ulam, all of whom were employed at Los Alamos National Laboratory for the Manhattan Project. [12] It was from this collaboration that the name Monte Carlo was coined by Neumann as a jab at Ulam's uncle who was known for borrowing money to gamble in the casinos of Monte Carlo. [12]

The Monte Carlo method in its earliest form could be used to calculate a PDF. Begin with a random distribution of particle positions in a box. Each pair of particles has a pairwise interaction between them. The total energy of the system is the sum of all pairwise potentials. The PDF can be calculated by simple geometry. A new random configuration is built and it has a new total energy and a new PDF. An estimate of the "true" PDF is obtained by building many models and weighting the individual PDFs by the relative energy of their corresponding systems. Boxes with the lowest internal energy would most contribute most to the final PDF.

This method of repetitive box-building is effective but inefficient. Without rules to govern how the initial configuration is built, a wide range of energies is produced and only a few systems contribute heavily to the final PDF. Early in the development of Monte Carlo methods, Nicholas Metropolis presented a modification with a thermodynamic underpinning. [13] The technique has become known as Metropolis Monte Carlo (MMC) and is still the most commonly-used

form of Monte Carlo simulation, the original publication [13] receiving over 14000 citations.

In MMC, a random starting configuration is built. The total internal energy is computed and atoms are moved in random steps. After each step, the change in energy of the system ΔU is calculated (by a pair potential or otherwise). The step is accepted or rejected based on the probability

$$P_{accept} = exp(\frac{-\Delta U}{kT}) \tag{1.4}$$

where kT is thermal energy. This relation requires that if the energy of the system is decreased, the move is accepted. If the energy of the system is increased, the move may be accepted unless the energy cost is disallowed by thermal vibrations. The end result of this type of calculation is that each *move* is weighted, unlike each *configuration* in the earlier Monte Carlo example. After a large number of steps, parallel MMC simulations produce PDFs that can be weighted equally. At that point, the model resembles a real material, with atoms wandering with Brownian motion as a result of thermal energy.

1.4.2 Reverse Monte Carlo and its early applications

Reverse Monte Carlo (RMC) is a modification of MMC first described in detail by McGreevey and Pusztai in 1988. [7] The term “reverse” applies because

observable quantities such as the PDF are used as input, rather than obtained at the end of a calculation. Just as in MMC simulation, a large box of atoms is produced and random moves are made with weighted acceptance probability. However, rather than basing P_{accept} on the change in energy of the system versus thermal energy, acceptance is determined by the change in the fit to observable data χ^2. If χ^2 is improved, the move is accepted. If the fit is worsened, the move may still be accepted based on the uncertainty of the data σ. The RMC acceptance probability becomes

$$P_{accept} = exp(\frac{-\Delta\chi^2}{\sigma}) \tag{1.5}$$

The stochastic nature of RMC implies that the course of a simulation proceeds very differently from least-squares refinements. The time dependence of a run is shown schematically in Figure 1.9. The least-squares refinement has distinct starting and ending points, and these are identical if the run is repeated (in the absence of strong correlations between the refined parameters). The RMC simulation has a defined starting point, but the convergence continues for infinite time.

Calculation of the PDF from an atomic configuration with a box edge of tens of Å is fast, so early work with RMC was concerned with modeling materials where the PDF was the only form of direct structural information: liquids and

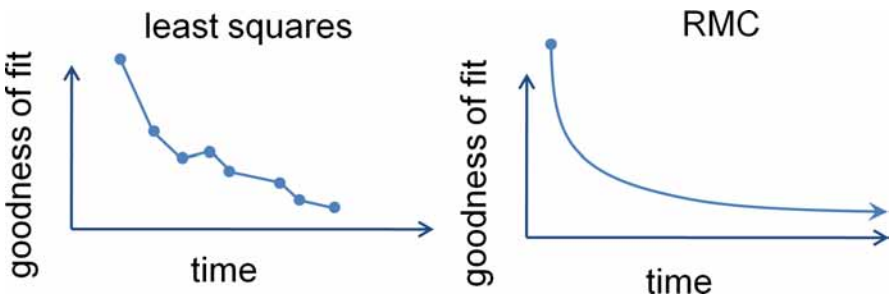

Figure 1.9: This schematic shows that least-squares refinements proceed in a small number of cycles, with defined starting and ending points. A repeated run produces identical results. In contrast, RMC fits will continue until they are stopped by the user, with the fit eventually flattening and oscillating around the best match.

glasses. RMC and PDFs lend themselves to the study of amorphous materials because neither requires symmetry. Early studies focused on LiCl, [14] AgBr, [15] and metallic glasses [16] where meaningful results were achieved from low-resolution PDFs with broad peaks that persist only to a few Å. One RMC fit to molten AgBr (from a 1992 study) is shown in Figure 1.10.

The introduction of total-scattering beamlines at Los Alamos, ISIS, and the APS provided new capabilities for studying the often-subtle disorder present in crystalline materials. With this capability came the opportunity to apply large-box RMC techniques fit PDFs of disordered crystalline materials.

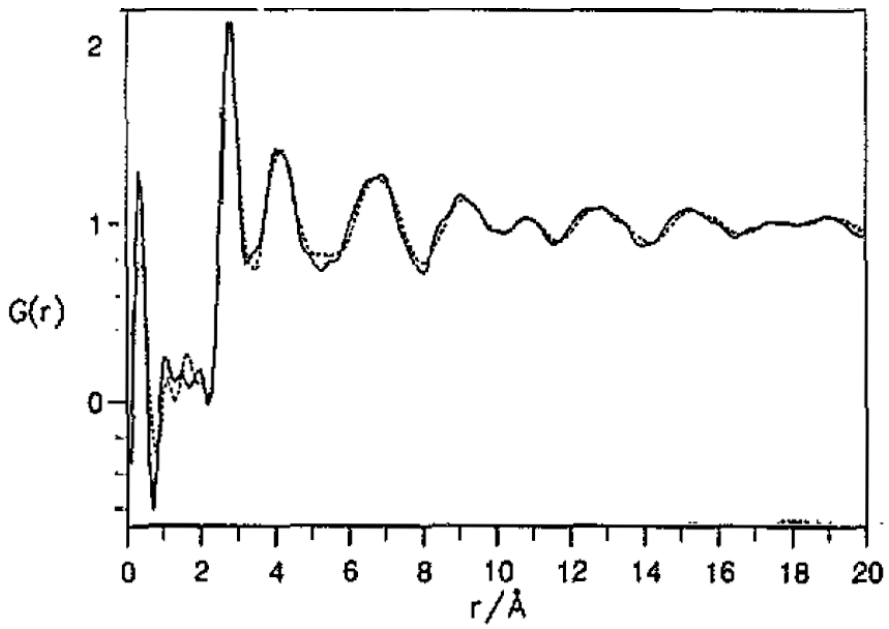

Figure 1.10: An early RMC fit to the neutron PDF of molten AgBr. Reproduced with permission from reference 15, © 1992 IOP Publishing.

1.4.3 Application of RMC to crystalline materials

With the advent of high-resolution PDF beamlines in the early 2000s came software for interpreting the data. In North America, the vast majority of publications on the NPDF neutron scattering beamline at Los Alamos and the 11-ID-B X-ray beamline at the Advanced Photon Source can be attributed to the adoption of PDFGETN, [8] PDFGETX2, [9] and PDFFIT software, [10] which perform data reduction and least-squares refinement of the PDF. The DISCUS software package [17] can also perform fits to total scattering data, but its adoption is not yet widespread. In Europe, the emergence of the GEM time-of-flight diffractometer at ISIS coincided with development of a number of software packages derived from MCGR and RMCA, both developed by groups at ISIS and Oxford. This suite of programs expanded to include RMC++, RMCPOW, and finally RMCPROFILE. [18] Of particular note is a difference in philosophy: North American work was centered on small-box modeling with PDFgui, while all development at ISIS focused on large-box modeling.

The number of local structure analysis publications per year for the three analysis packages (DISCUS, PDFGUI, RMCPROFILE) is shown in Figure 1.11. Despite having the capabilities of the other software, adoption of DISCUS seems slow, possibly due to a steeper learning curve. That may change with the pub-

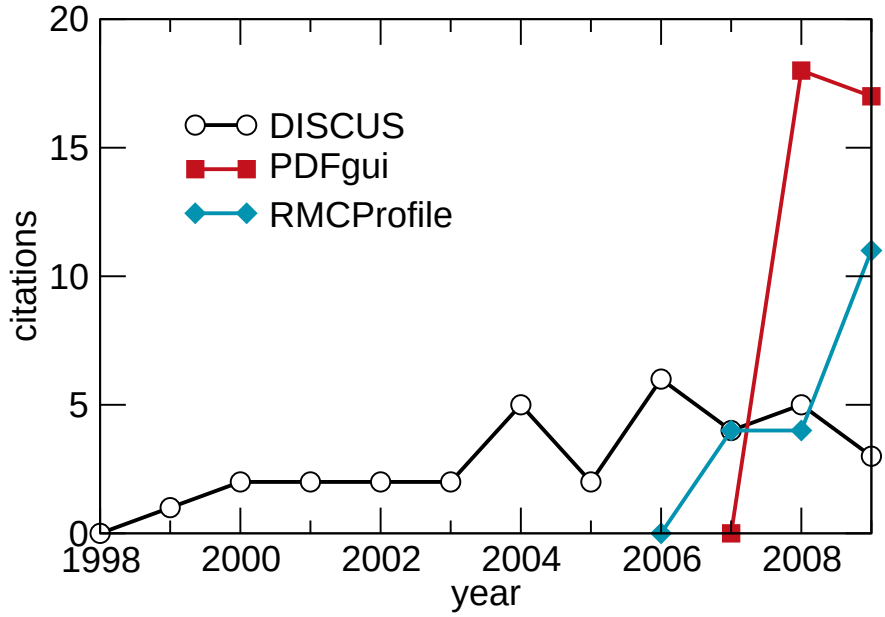

Figure 1.11: The yearly citations for local structure analysis using the three main software packages. Since their release in 2007, PDFGUI and RMCPROFILE have more quickly gained use.

lishing a “cookbook” with example codes. [19]

RMCPROFILE remains the only software package that is solely dedicated to RMC fits to crystalline materials, and it is used in each study of this thesis. “Profile” refers to the ability to simultaneously refine the Bragg profile of a material (implying crystallinity) alongside the PDF or other local structural information. In doing so, the Bragg profile constrains extensive properties that depend on the long-range crystal structure: cell parameters, average atomic positions, and the average ADPs.

The exact atomic positions in a material cannot be known (if only due to thermal disorder), but different methods of characterization can be used to create models. For RMC these models are not unique. This is in contrast to well-constrained, deterministic methods such as Rietveld refinement. However, both methods are “correct” in the sense that they reproduce the data. RMC has the advantage that multiple data sets (X-ray and neutron PDF, Bragg profile, $S(Q)$, bond valence sums, polyhedral constraints, *etc*.) can be used in a single simulation. In the next section I will outline how the constraints are used and how structural information can be extracted.

1.5 Systematics of reverse Monte Carlo simulations

There is no established method to set up a reverse Monte Carlo simulation, and the choice of inputs and constraints varies widely between runs based on the available datasets or the structural details which are desired. Unlike least-squares analysis, most structural analysis is performed *after* the simulation (analyzing the supercell), rather than before (constructing a starting model). The difference in approach is shown schematically in Figure 1.12. This section outlines a general plan for setting up and running a reverse Monte Carlo simulation using total scattering data. The general outline given here is applicable to all systems that are presented in this thesis.

1.5.1 Datasets and software

RMC simulations can accommodate many types of structural data, and it should be stressed that any one of them can be used to drive a simulation. However, the particular strength of the algorithm lies is its ability to *quickly create a model that reproduces the PDF*. For this reason, nearly all RMC studies in this work begin with total scattering data. This data can be collected at a

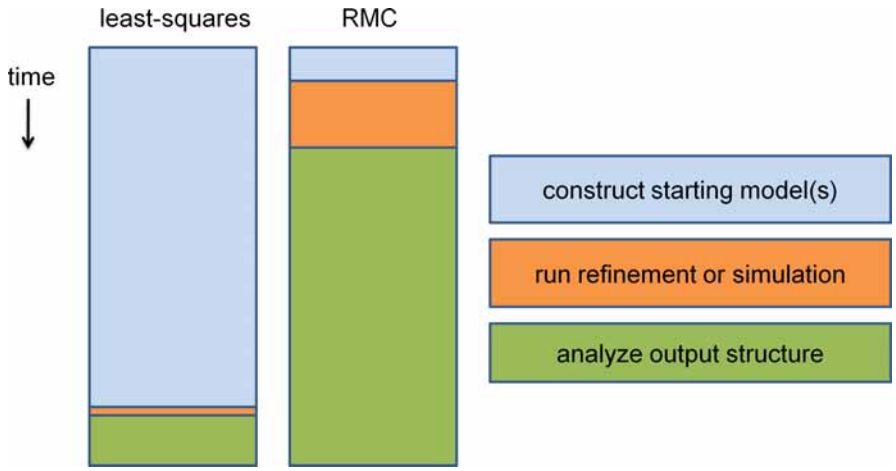

Figure 1.12: In least-squares analysis, most structural analysis goes into constructing a starting model that is close to the final answer. In RMC, the starting model is not as crucial, but much more time is spent extracting statistical information from the large-box model returned by the program.

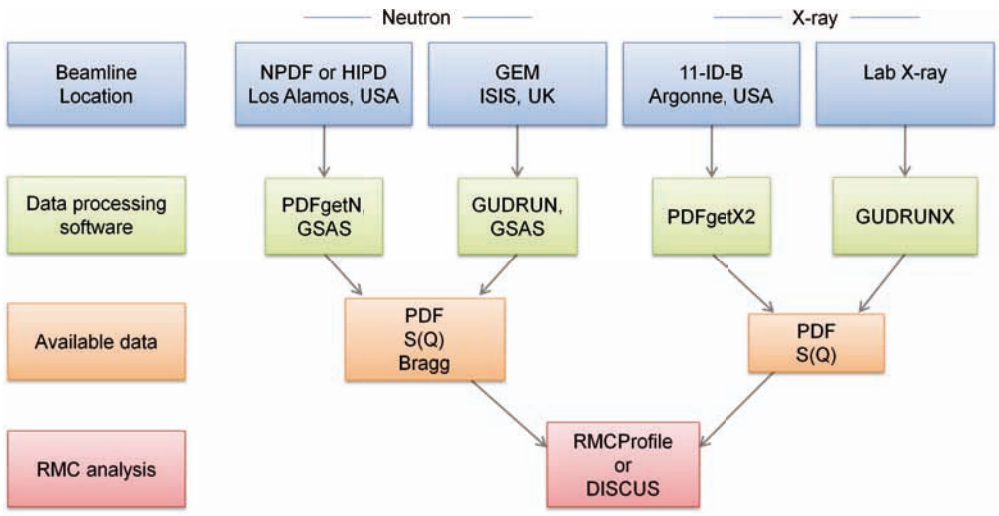

Figure 1.13: This owchart illustrates how data is moved from speci c beamlines through processing software in preparation for use in an RMC simulation.

spallation neutron source (NPDF, HIPD, GEM), synchrotron X-ray source (11-ID-B), or using a Mo or Ag constant wavelength X-ray diffractometer. Each facility uses a different software package to process the raw data, shown schematically in Figure 1.13. All total scattering data in this thesis was obtained from NPDF or 11-ID-B and processed using PDFGETN or PDFGETX2.

The data acquisition system for the NPDF and HIPD diffractometers at the Lujan Center automatically processes data that can be opened in GSAS (for Bragg diffraction data) and PDFGETN. The PDFGETN files, `*.sq` and `*.gr`, contain $S(Q)$ and PDF, respectively. This data can be used as input for RMCPROFILE after minor normalizations that account for differences in naming conventions

and unit conversions for the two software packages. In PDFGETN, the PDF output is output as a function denoted $G(r)$. This PDF is a normalization equivalent to the $D(r)$ defined by Keen [20] and used in RMCPROFILE. Keen's three normalizations are shown in Figure 1.14. For the sake of simplicity, all PDFs in this thesis are of the form $D(r)$.

1.5.2 Constructing a supercell

Along with experimental datasets, the supercell must be constructed before an RMC run. The supercell is the only data file strictly required by the program. Expansion of a unit cell via `*.cif` or `*.p1` structure is trivial, but some care should be taken in choosing the supercell dimensions and which atom types are present.

The configuration should be roughly square. The PDF can only be calculated for a sphere that is inscribed within the supercell. This means that the largest r value of the PDF that can be meaningfully fit is half the shortest box edge length. PDFs are typically output to $r = 20$ Å by default, so a supercell at least 40 Å per edge would be needed to fit the entire range. Non-orthogonal axes would increase the required edge length. Periodic boundary conditions are in effect.

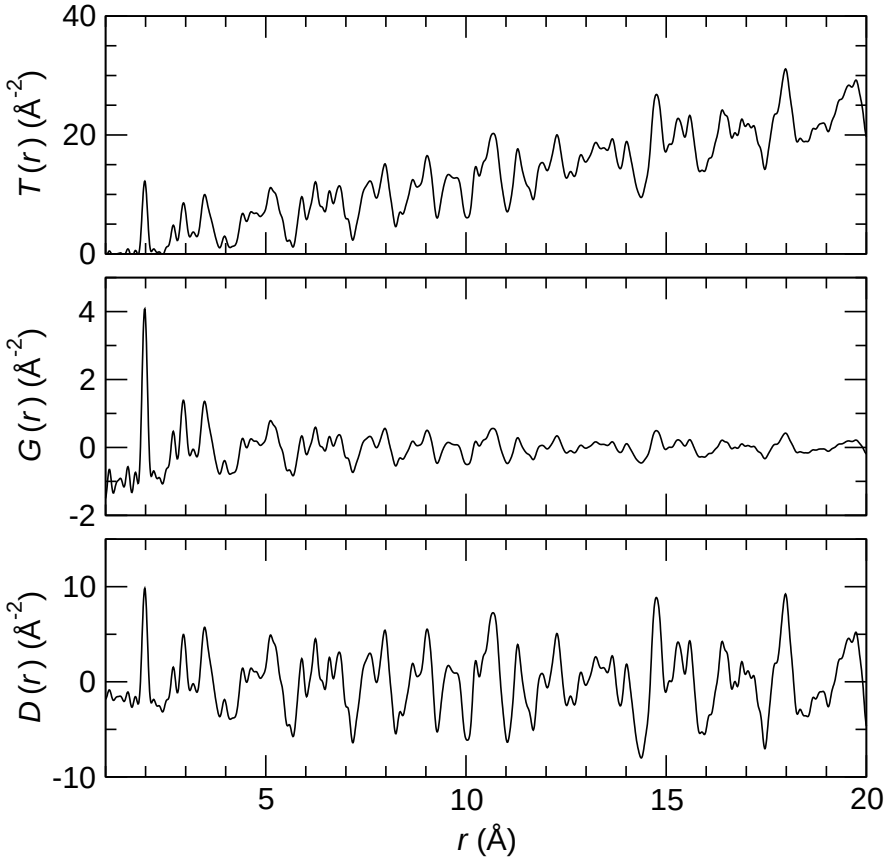

Figure 1.14: Three normalizations of the $Mg_{0.9}Cu_{0.1}Cr_2O_4$ PDF. These are labeled in the nomenclature of Keen [20] and RMCProfile. Data from North American beamlines is output by default in the form of $D(r)$.

The choice of how many distinct types of atoms to place in the supercell may seem straightforward, but clever splitting of atomic sites can greatly aid analysis. For example, the compound $Bi_2Ti_2O_7$ can be fit successfully using three types of scatterer in the supercell: Bi, Ti, and O. However, the compound can also be written $Bi_2Ti_2O_6O'$ to distinguish the O in $48f$ sites from the O′ in $8a$ sites. Since the behavior of O′ is of particular interest, the supercell is created using four atom types: Bi, Ti, O, and O′. The O and O′ nuclei have equivalent scattering lengths and the fit to data will be unchanged. After the simulation is over, it is far easier to extract metrics of O′ when they are the distinctly labeled. The alternative is to manually calculate (after the fact) which position a given O atom lies on.

Vacancies can be assigned to be distinct "atoms" with zero scattering length. Allowing swap moves between vacancies and other atom types allows vacancy ordering to be studied.

1.5.3 Atomic constraints

RMCProfile permits the inclusion of constraints that preserve atomic connectivity, closest approach, bond valence, bond length and angle stretching, *etc*. These are an efficient way to include the coordination information from NMR

or EXAFS (for example) that is assumed to be correct, or to conserve polyhedral linkages in a relatively open structure such as a coordination polymer or liquid. [21]

The simplest constraint is a nearest-neighbor cutoff distance which creates a hard-sphere repulsion preventing atoms from moving closer than the first peak in the PDF. For most oxides, setting a value of the nearest-neighbor cutoff around 1.7–1.9 Å coincides with the inner edge of the first peak. It also prevents atoms from sliding past each other and conserves the overall geometry of the supercell. In oxides, M–M and O–O cutoffs are generally not needed.

Polyhedral constraints preserve the connectivity of polyhedra and their corner- or edge-sharing linkages. They are described in detail in the RMCPROFILE documentation and are most useful for liquids or open frameworks. No studies in this work have utilized them.

Bond valence constraints use the sum of chemical bond lengths reaching an element to determine its valence, and can be applied to ensure that the supercell contains bonds that are chemically reasonable. The systematic effect of increasingly weighted bond valence constraints has not yet been established, but in some cases it has been shown to greatly disorder the configuration. [22] It is typically only applied as a weak constraint to prevent runaway atoms, *i.e.* only

the most extreme cases of short or long bonds. Methods of calculating bond valence sums *after* simulation have proven valuable and will be discussed for the cases of $CuMn_2O_4$, $Mg_{1-x}Cu_xCr_2O_4$, $Bi_2Ti_2O_6O'$, and $Bi_2Ru_2O_6O'$.

1.5.4 Analysis

Not present in this chapter is a detailed discussion of the analysis of the final atomic configurations. These techniques will be introduced as they appear in specific examples.

Chapter 2

Coordination, compositional disorder, and Jahn-Teller disorder in $CuMn_2O_4$

2.1 Introduction

The oxides La_2CuO_4 and $LaMnO_3$ have been at the heart of great excitement in condensed matter science in the last quarter century, being the parent com-

[1]Reproduced with permission from D. P Shoemaker, J. Li, and R. Seshadri, Unraveling Atomic Positions in an Oxide Spinel with Two Jahn–Teller Ions: Local Structure Investigation of $CuMn_2O_4$. *J. Am. Chem. Soc.* **131** [32] 1145011457 (2009), © 2009 American Chemical Society.

pounds respectively of high-temperature copper oxide superconductors[23] and colossal magnetoresistive (CMR) manganese oxides.[24, 25] A distinguishing feature of these compounds and their derivatives is the cooperative Jahn-Teller (JT) activity of the B-site ions Cu^{2+} and Mn^{3+}. In the CMR case, it is believed that JT phenomena are an important component of the unprecedented behavior displayed.[26]

Poorly-defined mixtures of copper and manganese oxides known as hopcalite were first found to be effective oxidizers of CO during World War I. [27] Use of hopcalite powder as a low-temperature oxidizer continues today for respiratory protection, and numerous studies have found that their catalytic activity is a result of a flexible valence in $Cu^{1+/2+}$ and $Mn^{3+/4+}$. [28–30]. Since the flexible valence allows for catalytic behavior and only a subset of those valences produce JT distortions, it should be of interest to probe the local structure as an indicator of relevant valence states. These distortions do not necessarily align with each other over long ranges.

When JT-driven bond stretches and the consequent rotations are present only on a *local* scale, their effects can average to zero in the Rietveld analysis. Determining element-specific bond lengths within solid solutions, phosphors, and ferroelectrics has been a significant thrust in X-ray absorption spectroscopy,[31–35] and has benefitted from the recent advent of real-space total scattering

analysis.[36–38] The complimentary data sets allow the usual (for example Rietveld) analysis in reciprocal space for long-range average parameters, and PDF analysis in real-space for local atom-atom pairs from typically 1 Å to 50 Å, with a real-space resolution of the order of hundredths of an Å.[39]

The PDF is a representation of all distances r between atom pairs in a material, so bond length distributions which are averaged in the bulk can become distinct peaks in the low-r PDF. Recent investigations of JT-distorting oxides (most notably $LaMnO_3$) using the PDF method have found that dynamic JT distortions persist even into the high temperature phase, above the cooperative JT transition temperature. As a consequence, bonding distances that are poorly estimated from the average structural model are often better described using the PDF.[11, 38]

2.1.1 Jahn-Teller distortions

Early understanding of cooperative JT distortions in spinel compounds can be traced back to the vast body of crystallographic data collected on these systems at the Philips Laboratory in Eindhoven, appearing in the literature from the 1930s. Early attempts to rationalize the data were made by Goodenough and Loeb[40] based on the a mechanism they referred to as “semicovalent ex-

change." Dunitz and Orgel[41] recognized the role that the JT theorem[42] played in determining the distorted octahedral coordination of many Cu^{2+} species, including in extended compounds like $CsCuCl_3$. They also pointed to the role of the JT theorem in determining the tetragonal structures of Mn^{3+} (spinel) compounds, including hausmannite Mn_3O_4 and hetærolite $ZnMn_2O_4$. Wojtowicz[43] carried the analysis further and examined the high temperature first-order transformation of JT spinels to the cubic spinel structure. Interestingly, in the case of the molecular, tetrahedral Cu^{2+} species such as the $CuCl_4^{2-}$ anion, Felsenfeld[44] approached the problem from the viewpoint of a distortion from the preferred square-planar arrangement of ligands around Cu^{2+}, driven by Coulombic repulsion between the Cl^- anions. Not much is known regarding Cu^{2+} in the tetrahedral sites of spinels as drivers of tetragonal distortions.

The oxide spinel $CuMn_2O_4$, is not simply comprised of only Cu^{2+} and Mn^{3+}. The literature on this compound is extensive but inconsistent, in part because it crystallizes with varying degrees of inversion δ, defined $Cu_{1-\delta}Mn_\delta[Mn_{2-\delta}Cu_\delta]O_4$. Early work from Sinha *et al.*[45] first suggested a cubic spinel with all Cu^{1+} in the tetrahedral site with the octahedral site equally occupied by Mn^{3+} and Mn^{4+}. Buhl[46] pointed out that pure compositions with 1:2 Cu:Mn ratios were tetragonal when formed above 750°C and when cooled

below this temperature, phase separated into a cubic spinel phase and some parasitic phases. Neutron diffraction studies carried out on samples quenched from 940°C suggested an inversion δ=0.24(2) and a c/a tetragonal ratio of 1.03. The need for water-quenching to form tetragonal $CuMn_2O_4$ was confirmed by Robbrecht and Henriet-Iserentant.[47] Numerous groups have carried out magnetic susceptibility, x-ray absorption, and x-ray photoelectron spectroscopic (XPS) studies in an attempt to establish the oxidation states of the ions in $CuMn_2O_4$; these have been summarized in the more recent works of Metz *et al.*[48] and Gillot *et al.*[49]

Reverse Monte Carlo analysis allows for statistical questions regarding coordination and bond valence to be addressed, *even for ions on sites with significant site mixing*. Distinct JT-active Cu^{2+} is found on the tetrahedral site and Cu^{3+} appears on the octahedral site. XPS studies, carried out with greatly improved signal to noise ratios and energy resolution when compared with the prior work, are consistent with the assignments made from bond valence sum analysis of the local coordination. One purpose of this work is to establish aspects of the structure of $CuMn_2O_4$, including the fascinating charge disproportionation of Cu^{2+} as means of obviating its JT tendency, and the nature of the JT distortion on the tetrahedral site. Equally, this study demonstrates the power of modern neutron scattering tools, used in judicious conjunction with the tools of computer

simulation, in unraveling structural details in a pathologically complex spinel compound.

2.2 Methods

Ceramic pellets of $CuMn_2O_4$ were prepared by grinding stoichiometric amounts of CuO and MnO (99.9%, Aldrich) in an agate mortar and pestle, pressing at 100 MPa, and firing in air at 860°C for 21 h. For the firing, the pellets were placed on a bed of sacrificial powder of the same composition in covered alumina crucibles. Pellets were water quenched since single-phase $CuMn_2O_4$ forms in a very narrow temperature window between $\approx$ 830°C and 910°. [50] Laboratory x-ray diffraction data was acquired on a Philips X'Pert diffractometer with Cu-K_α radiation. Magnetic properties were measured using a Quantum Design MPMS 5XL SQUID magnetometer. Time-of-flight (TOF) neutron scattering was performed on NPDF[51] at Los Alamos National Laboratory. Rietveld refinement was performed using the XND code[52] for x-ray data and GSAS [53] for TOF data. The PDF and $F(Q)$ were extracted using PDFGETN [8] and least-squares refinement of the PDF was performed using PDFGUI. [10] We used $Q_{max} = 30\,\text{Å}^{-1}$ to construct the PDF, with selection criteria based on the peak-width methods of Qiu *et al.* [39] X-ray photoelectron spectra (XPS) were

acquired on sintered pellets using a Kratos Axis Ultra spectrometer. Peak fitting for XPS was performed with CASAXPS with a Shirley-type background and Gaussian peaks.

Reverse Monte Carlo simulations [54, 55] were run using RMCPROFILE version 5 [18] on a $10 \times 10 \times 7$ hausmannite supercell with 19600 atoms. A hard-sphere repulsion was applied to prevent Mn–O and Cu–O bond distances of less than 1.79 Å, and 1.82 Å, respectively. The fraction of random attempted swaps between Cu and Mn was kept at 5% of the translational moves. Runs were performed using a maximum translational step size of 0.02 Å and dataset error σ adjusted to reflect experimental uncertainty while maintaining a move acceptance probability of about 50%. A typical simulation was run for about six million steps, taking about about 12 h on a 2 GHz Intel Pentium 4 processor. Many starting configurations (disordered and ordered) were used to observe the progression of the simulation to similar final configurations. There are 2800 tetrahedra and 5600 octahedra, with Cu and Mn allowed to swap positions to attain the best fit to the total scattering function $F(Q)$ and the PDF in the form of $T(r)$ as given by Keen. [20] The experimental $F(Q)$ was convoluted with the supercell size and fit up to $Q = 15$ Å^{-1}, while $T(r)$ was fit up to $r = 11$ Å. A paramagnetic contribution to $S(Q)$ was simulated by adding random spins with an average μ_{eff} value from SQUID magnetometry to the magnetic cations (all

except Cu^{+}). The magnetic contribution is nontrivial during the fit to $S(Q)$, but it does not have any appreciable affect after Fourier transformation to the PDF.

Bond valence sums (BVS) were extracted from atoms in the supercell using the bond valence formula

$$V = \sum exp\left(\frac{R_0 - R_i}{0.37}\right) \tag{2.1}$$

where V is the cation valence, the sum runs over all bonds to the cation, R_0 are tabulated for each cation-oxygen pair in the work by Brese and O'Keeffe,[56] and R_i is the bond length in Å. To assign an integer valence, V was calculated using each possible valence (1+ to 3+ for Cu and 2+ to 4+ for Mn), and the valence which most closely matched its corresponding V was assigned. Crystal structures were visualized with AtomEye [57] and VESTA. [58]

2.3 Results and discussion

2.3.1 Average structure

Laboratory Cu-K_α XRD Rietveld refinement using the $I4_1/amd$ unit cell is shown in 2.1(a). The sample is single-phase and all peak locations are matched

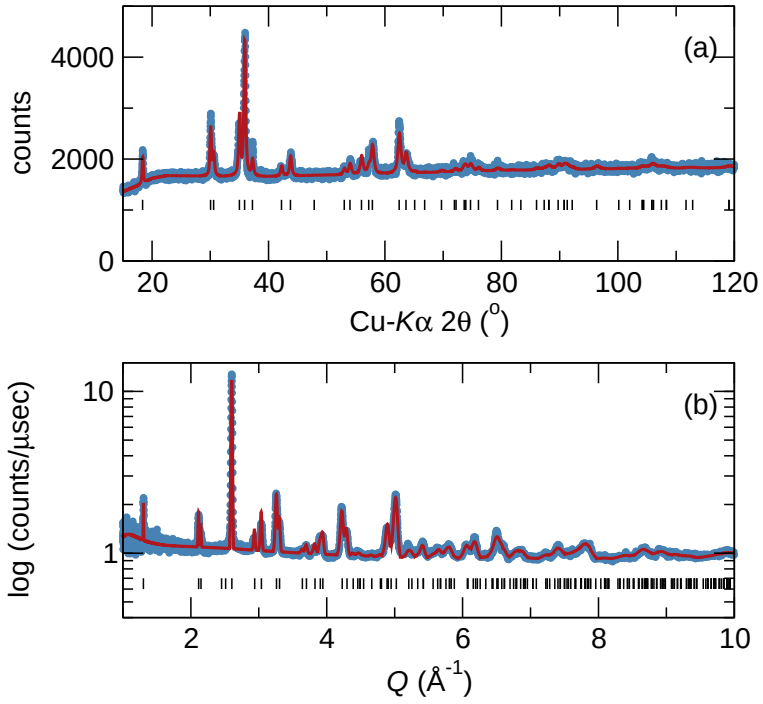

Figure 2.1: Rietveld refinement of single-phase, tetragonal $CuMn_2O_4$ from (a) laboratory x-ray diffraction data and (b) TOF neutron scattering data with $R_{wp} = 5.21\%$ acquired at the NPDF diffractometer at Los Alamos (note log scale). Both data sets were collected at room temperature. Reproduced with permission from reference 59, © 2009 American Chemical Society.

Table 2.1: Average structural parameters for $Cu_{1-\delta}Mn_{\delta}Mn_{2-\delta}Cu_{\delta}O_4$ [$\delta = 0.270(2)$] at 300 K obtained from Rietveld refinement of TOF neutron diffraction data: $I4_1/amd$ (No. 141, origin choice 2), $a = 5.84755(8)$ Å, $c = 8.5508(3)$ Å, $c/a = 1.03399(3)$. All U_{ij} are in Å^2.

Atom	Site	x	y	z
Cu/Mn(tet.)	$4a$	0	3/4	1/8
Mn/Cu(oct.)	$8d$	0	0	1/2
O	$16h$	0	0.0272(1)	0.2629(1)
	U_{11}	U_{22}	U_{33}	U_{23}
Cu/Mn(tet.)	0.0116(5)	0.0116(5)	0.021(1)	
Mn/Cu(oct.)	0.0015(7)	0.0048(8)	0.020(1)	0.004(1)
O	0.0127(2)	0.0090(2)	0.0243(3)	-0.0095(3)

by the tetragonal $I4_1/amd$ structural model. Despite the first few peaks in the diffraction pattern being relatively narrow, indicating a significant crystalline correlation length, the counts die down rather quickly with increasing 2θ. The decline in counts is much quicker than would arise from the x-ray form-factor fall-off, and is suggestive of large thermal displacement parameters. Rietveld refinement of the highest resolution bank (from four banks total) of TOF neutron powder diffraction data is shown in 2.1(b), with structural parameters in Table 2.1. The extent of inversion (Mn occupancy on the A site) was determined to be 0.270(2), and the structure was metrically tetragonal with c/a = 1.03399(3). Neutron diffraction form factors are constants, independent of the scattering angle or momentum transfer $Q = 2\pi/d$. Once again, the rapid de-

cline of counts with Q is suggestive of large atomic displacement parameters, and this is indeed seen from the refinement results in Table 2.1. Large atomic displacement parameters emerge from refinement of the Bragg scattering as a means of accommodating the varying coordination around the different cations on the tetrahedral and octahedral sites. Of particular interest is the anisotropy in the thermal parameters (data presented in Table 2.1).

2.3.2 Magnetic properties

In order to understand the nature of magnetic interactions and ordering, in a well-characterized $CuMn_2O_4$ sample, temperature dependence of zero-field cooled (ZFC) and field cooled (FC) magnetization data was recorded under a 100 Oe field [2.2(a)]. The compound displays magnetic ordering to a ferrimagnetic ground state with diverging ZFC and FC magnetization (indicative of a hard ferrimagnet) below T_c = 35 K. In 2.2(b), the reduced molar susceptibility is plotted as a function of the reduced temperature, using the Curie constant C and the Curie-Weiss temperature Θ_{CW}, obtained from fitting the high temperature (320 K to 400 K) portion of the molar susceptibility to the Curie-Weiss law, $\chi = C/(T - \Theta_{CW})$. The utility of such analysis in spinel compounds with magnetic ions on both the tetrahedral and octahedral sites has been presented

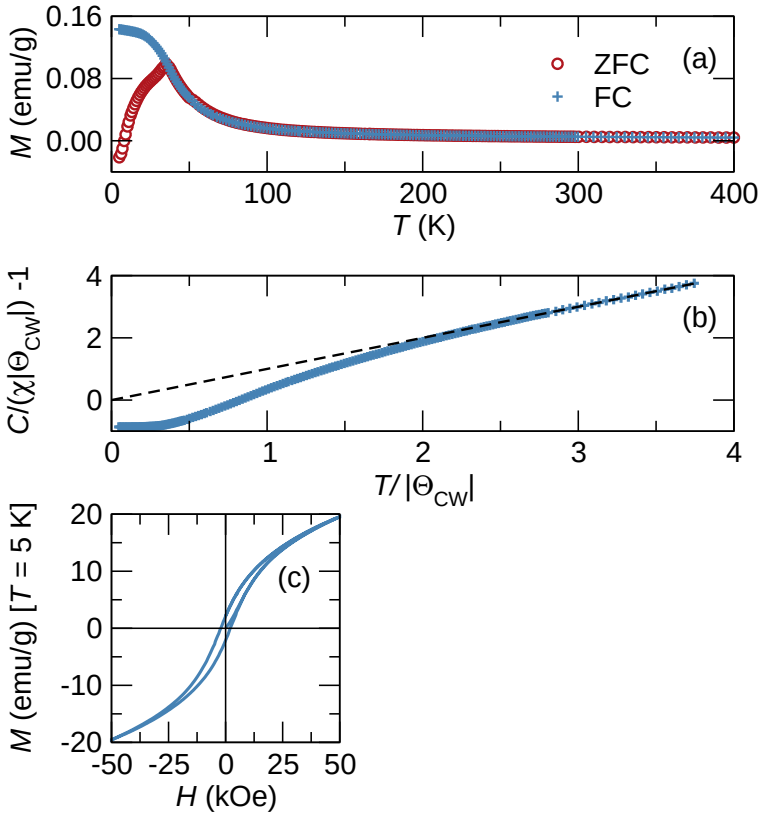

Figure 2.2: (a) Magnetization of $CuMn_2O_4$ after zero-field cooling (ZFC) and during field-cooling (FC) acquired under a field of 100 Oe, showing the emergence of a hard ferrimagnet below 40 K. In (b), the reduced molar susceptibility is plotted against the reduced temperature, with $C = 4.93\,\text{emu K mol}^{-1}\,\text{Oe}^{-1}$ and $\Theta = -107\,\text{K}$. The dashed line is the expectation for Curie-Weiss behavior. (c) Magnetization as a function of the magnetic field at 5 K. Reproduced with permission from reference 59, © 2009 American Chemical Society.

elsewhere.[60] Deviations below the Curie-Weiss line (dashed) in such analysis indicate long-range ferrimagnetism, corresponding to uncompensated antiferromagnetic coupling as the dominant interaction. The extent of magnetic frustration is the ratio $f = |\Theta_{CW}|/T_c$ and this can be read as the inverse of the abscissa in 2.2(b). It is seen that $CuMn_2O_4$ is not very frustrated, perhaps as a result of the antiferromagnetic interaction between the tetrahedral and octahedral sites being significantly stronger than other interactions. With many magnetic species in this compound, the single Curie constant C cannot be used to extract a consistent set of μ_{eff} values corresponding to each magnetic ion present. Panel (c) displays the magnetic hysteresis loop at 5 K for $CuMn_2O_4$, showing the absence of complete saturation even in fields of 50 kOe.

2.3.3 Local structure: Least-squares analysis

Non-cooperative distortions are manifest in reciprocal space by diffuse scattering, which is converted *via* appropriate Fourier transformation of the total scattering $F(Q)$ into real-space pairs of atom-atom distances in the PDF. Experimental PDFs for $CuMn_2O_4$ are shown as points in the two panels of 2.3. The least-squares refined PDF [solid line in 2.3(a)] of the experimental data using the TOF Rietveld structure as input for PDFFit2 results in an excellent fit to

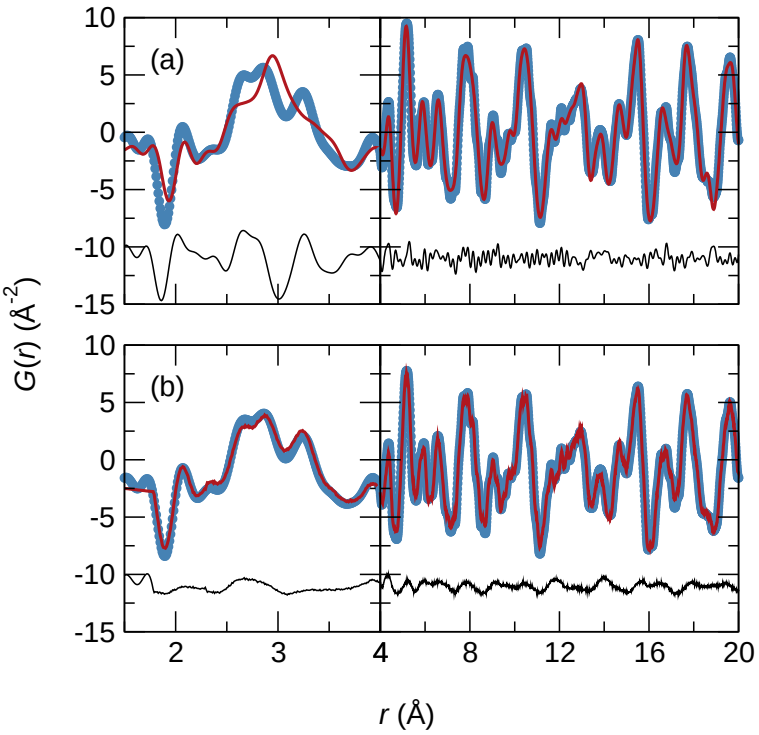

Figure 2.3: Fit to the experimental PDF up to 20 Å *via* (a) least-squares refinement of a single unit cell (b) and RMC simulation using a 10 × 10 × 7 supercell. The x-axis scale has been stretched below 4 Å to emphasize the distinct local structure. Difference curves are shown below. The peaks from 2.5 Å to 3.5 Å describe O–O and B–B pair correlations. The nearest-neighbor Mn–O bond (negative peak at about 2 Å) and the O–O correlations are not described by the $I4_1/amd$ model. Reproduced with permission from reference 59, © 2009 American Chemical Society.

high-r data, beyond about 4 Å, but within this distance, the experimental PDF is very poorly modeled.

The poor fit for small r shows which atom-atom pairs lead to the deviation between the average structure model and the data. A noteworthy feature in the low-r PDF is the negative peak at 1.9 Å corresponding to Mn–O pairs – the peak is negative since Mn has a negative neutron scattering length. The average structure (solid line in 2.3(a)) overestimates the Mn–O distance by about 0.1 Å. Another significant mismatch between data and average structure fit is seen in the cluster of peaks at 2.8 Å, which describe the O–O pairs on the edges of polyhedra (tetrahedra and octahedra). Since neither Mn–O nor O–O distances are fit, the average structure does not describe the true local structure of the polyhedra in $CuMn_2O_4$.

Single-cell PDFGUI least-squares refinement of $CuMn_2O_4$ cannot produce a fit to the low-r region of the PDF while maintaining $I4_1/amd$ symmetry. Thus the average symmetry is *not relevant within the unit cell.* We use RMC where all atoms in the structure are allowed to translate freely, with constraints placed only on closest-approach. It should be stressed that RMC produces snapshots of plausible configurations that, taken in total, yield a locus of atoms that reproduce the data. Errors or artifacts in the data can manifest false structural details in the simulated structure, so properly-normalized, high-quality data and an un-

derstanding of the origin of both systematic errors and true observed distortions is essential.[61]

2.3.4 Local structure: Reverse Monte Carlo analysis

RMC was performed as explained in the methods section, and the fit to the PDF data of $CuMn_2O_4$ is shown in 2.3(b). The crucial difference between the PDF fits as performed by least-squares average structure refinement *versus* RMC simulation is the agreement of the nearest-neighbor Mn–O and Cu–O bonds near 2 Å, and the O–O and B–B cluster from 2.5 Å to 3.0 Å. At higher r, the number of contributing atom pairs increases as r^3, so the experimental $G(r)$ approaches the average structure.

The supercell of 700 unit cells can be folded back into a single unit cell to verify that the atoms are in reasonable positions that correspond to those of hausmannite. The fit to $F(Q)$ in 2.5 helps keep this long-range structure in place. The folded configuration in 2.4(a) has clusters of 700 atoms at each site. The RMC simulations allow site-swapping of cations and produce a model with inversion around $\delta = 0.35$ which is close to the 0.270 obtained from Rietveld. A key distinction between least-squares refinement of the PDF and fits obtained from RMC is that peak broadening in the former is accommodated by instru-

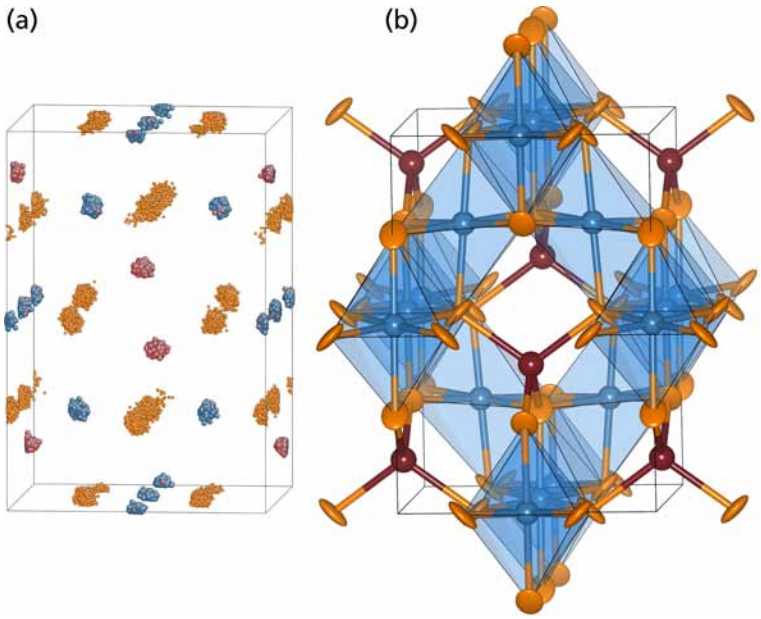

Figure 2.4: (a) "Point clouds" of simulated atom positions obtained by folding the $10 \times 10 \times 7$ RMC supercell into a single unit cell. Blue spheres are Mn, red are Cu and orange are O. (b) Rietveld-refined unit cell with tetrahedral M–O bonds, and coordination polyhedra around the octahedral site. 95% thermal ellipsoids are depicted around oxygen atoms. The O ellipsoids are highly oblate ($U_{23} < 0$) and the volume they trace roughly corresponds to the smearing of O positions in RMC. We stress that the RMC model need not perfectly reproduce the thermal ellipsoids since it describes non-correlated local distortions. Reproduced with permission from reference 59, © 2009 American Chemical Society.

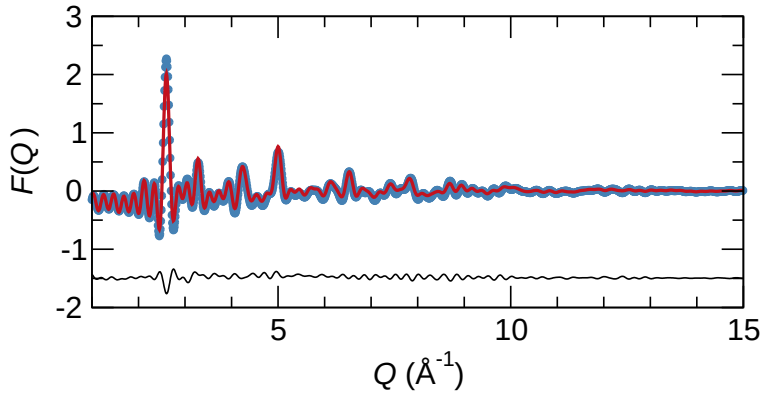

Figure 2.5: Fit to the experimental $F(Q)$ up to 15 Å^{-1} *via* RMC simulation. This data is convoluted to the width of the supercell. Fitting in reciprocal space simultaneously with $G(r)$ constrains the system to maintain a consistent average structure. Reproduced with permission from reference 59, © 2009 American Chemical Society.

mental broadening and thermal parameters. In contrast, RMC performs no such broadening, and broad $G(r)$ peaks can only be represented in the supercell by having an equally broad distribution of bond distances. RMC also does not account for termination ripples from the step function at $S(Q_{max})$. Some bond distances that are intuitively too long or short are necessary to fit the systematic peak broadening inherent in every experimental PDF.

If the thermal displacement is isotropic, the distribution of atoms around each ideal lattice position should be spherical. This is not the case for the oxygen distributions, which are found (even in the TOF Bragg refinements) to be

smeared normal to the tetrahedral (Cu/Mn)–O bonds, resulting in a large value for U_{33} and a negative value for U_{23}. The oxygen clouds seen in 2.4 are clearly not spherical, and should roughly lie within the long-range thermal displacement U factors. The comparison to the refined TOF Bragg data with $U_{23} < 0$ is shown in 2.4(b). The flattening of the oxygen point clouds toward the tetrahedral bonds is clearly evident in both fits.

RMC distributions of Cu and Mn nearest-neighbor bond lengths are separated by coordination and plotted in 2.6. For a local structure that matches the average long-range structure perfectly, Mn–O and Cu–O bond distributions at each site must be identical. Instead, 2.6(b) clearly shows nearest-neighbor Cu–O and Mn–O bond length peaks are centered distinctly apart from the average structural distance obtained from Rietveld. Indeed, Mn and Cu with the same coordination geometry should possess different bond lengths. Without a local structure probe such as PDF, these differences cannot be seen if they lack long-range cooperative ordering.

Bond angles can also be separated by cation and coordination and extracted from the RMC supercell. The O–M–O bond angle distributions $B(\theta)$ in 2.7 are weighted by $\sin(\theta)^{-1}$ to account for the probability of finding a given angle θ for a randomly rotated bond. [62] The bond angles from the average $I4_1/amd$ structure are denoted by vertical lines in (e). The O–Cu–O bond angles in 2.7(a)

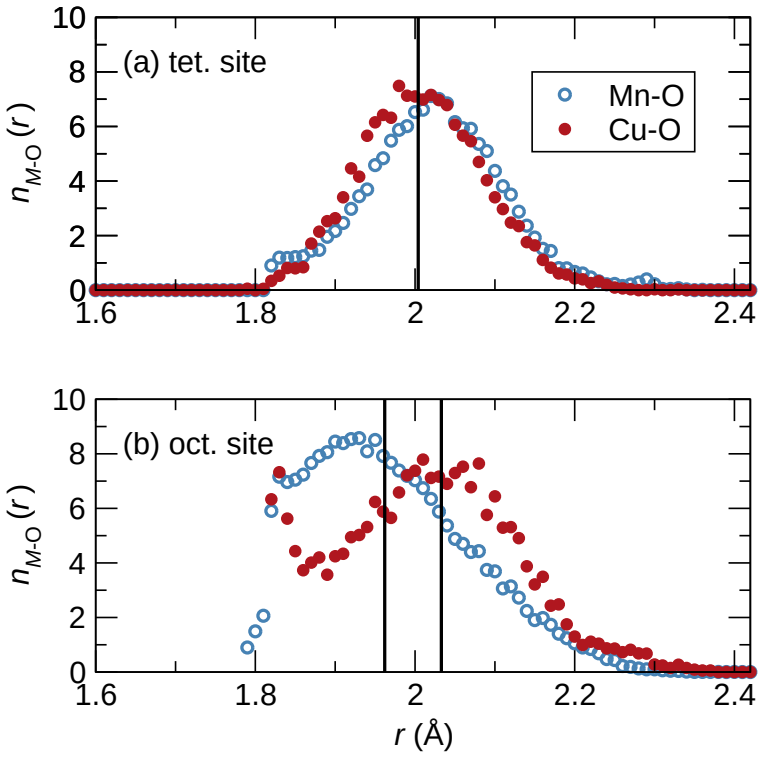

Figure 2.6: Partial bond distance distributions $n_{M-O}(r)$ for (a) tetrahedral and (b) octahedral M–O pairs obtained from the RMC modeling of $CuMn_2O_4$ according to by cation species and coordination. Some clustering is seen near the hard-sphere cutoff and is a result of RMC fitting to the low-r termination ripples. Average structure bond lengths from Rietveld refinement are denoted by vertical lines. The average structure would contain four short and two long octahedral bonds in (b), but this is not seen in RMC. Reproduced with permission from reference 59, © 2009 American Chemical Society.

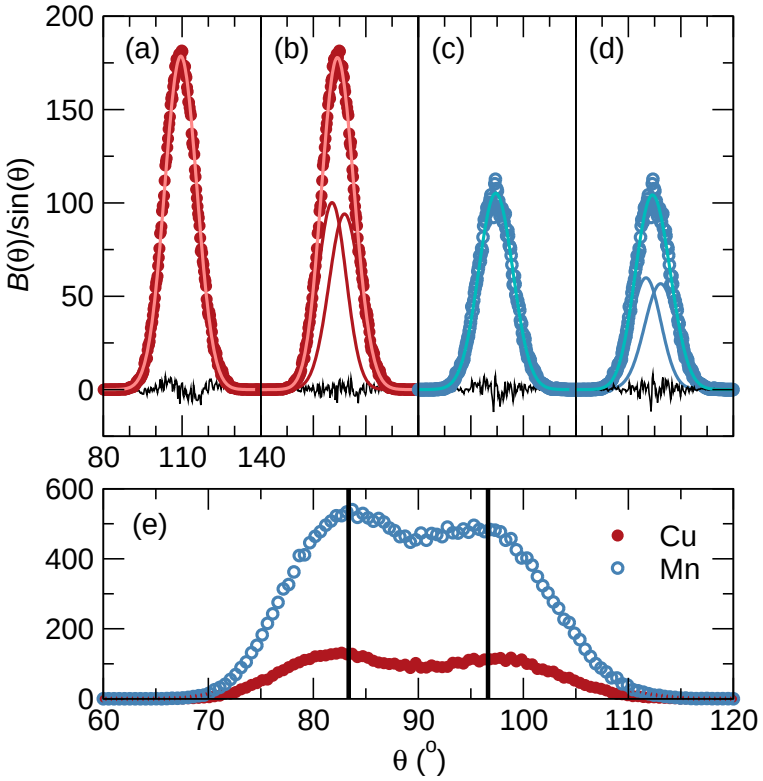

Figure 2.7: Bond angle distributions $B(\theta)$ for all nearest-neighbor O–M–O bond angles in the RMC simulation, for (a-b) tetrahedral Cu ions, (c-d) tetrahedral Mn ions, and (e) octahedral ions. Average-structure (Rietveld) bond angles are shown by vertical lines. In (a) and (c), data are fit using a single Gaussian. In (b) and (d), two Guassians centered equidistant from 109.5° are used. The χ^2 for O–Cu–O tetrahedral angles is improved from 47.0 to 31.5 by fitting to two peaks, but O–Mn–O is only improved from 48.8 to 41.6. Reproduced with permission from reference 59, © 2009 American Chemical Society.

display a clear bimodal difference curve when fit to a single Gaussian, and the fit can be improved significantly by fitting to two Gaussians (2.7(b)) with centers at 107.1° and 111.9°, which are more distorted than the Rietveld values of 108.0° and 110.2°. These two angles angles correspond to a flattening of the coordination around tetrahedral copper. In 2.7(c-d), fitting O–Mn–O bond angles with a single Gaussian does not produce a bimodal difference, and the improvement after fitting to two angles is not as marked as in Cu tetrahedra. This evidence points toward MnO_4 tetrahedra that are significantly less distorted than CuO_4. Distortions of tetrahedral Cu^{2+} are known in systems where the tetrahedra do not share features, *e.g.* in compounds with isolated CuX_4^{2-} species.[63] The literature on distorted Cu^{2+} tetrahedra in extended oxides is more scarce.[64] The bond angles of (Mn/Cu)O_6 octahedra in 2.7(c) show a two-peaked distribution centered near 80° and 100°. Describing the MO_6 shape from the bond angle distribution is more complex than the tetrahedral case, but there should be *less* cation-dependent distortion on the B site due to edge sharing between octahedra. In contrast, no tetrahedra share edges or corners with one another.

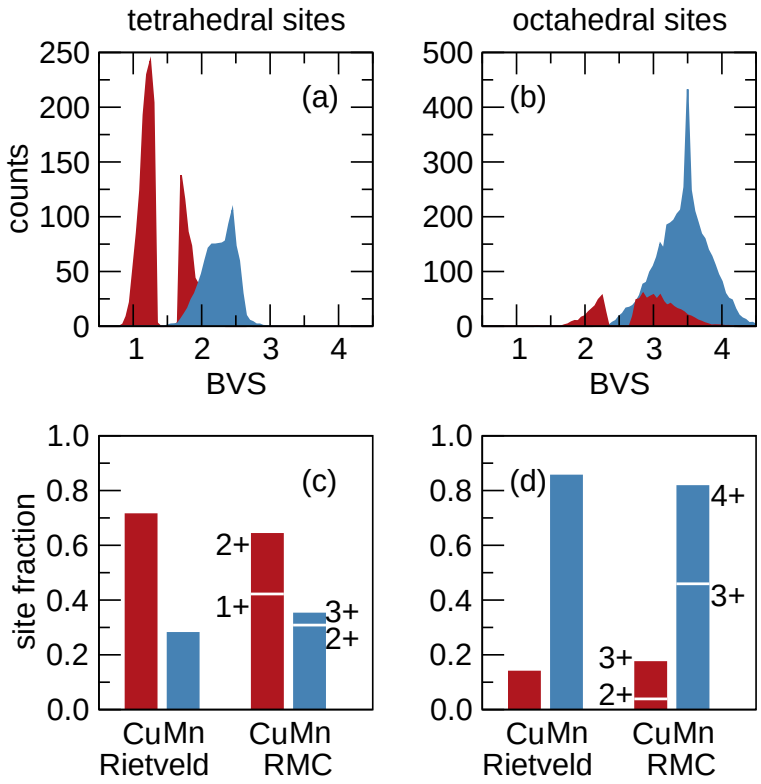

Figure 2.8: Histograms of bond valences are shown in (a) and (b) for Cu and Mn calculated on the two sites from the (Cu/Mn)–O bond-length distributions of the RMC supercell. In (c) and (d) the calculated fractions of the Cu and Mn on the two sites from Rietveld refinement are compared to the statistical RMC result in (a) and (b). Note the tendency for charge disproportionation away from Cu^{2+} and Mn^{3+}, and the presence of octahedral Cu^{3+}. Reproduced with permission from reference 59, © 2009 American Chemical Society.

2.3.5 Valence analysis from RMC and XPS

Just as bond distances and bond angles can be obtained from the RMC snapshot, bond valence sums (BVS) can be calculated for each cation. No symmetry constraints are applied in the RMC analysis, so bond distances and nearest-neighbor information are truly local and not influenced by long-range ordering in the bulk. Valence states for each cation were assigned by minimizing the difference between the ideal and BVS-calculated valence sum using the RMC bond distances. These distributions are shown in 2.8, both as distributions of the calculated BVS sum for each cation of each coordination (top) and stacked bar charts comparing the inversion, and charges for Rietveld versus RMC results (bottom). Inversion of Mn onto the A-site and the presence of d^{10} Cu^{1+} and d^{5} Mn^{4+} both serve to dilute the cooperative JT effect. Analysis of the bond valence of the RMC snapshots reveals that *only 28% of the tetrahedral cations* are JT-active d^{9} Cu^{2+} or d^{4} Mn^{3+}.

Using the average bond distances from Bragg refinement, the valence of ions is 1.66 and 2.63 on the tetrahedral and octahedral sites respectively. This does not agree with the RMC result, which has the majority of tetrahedral Cu as 1+. The average structure also finds Mn valences of 2.07 and 3.27 for tetrahedral and octahedral sites, respectively. While RMC does indeed find tetrahedral Mn

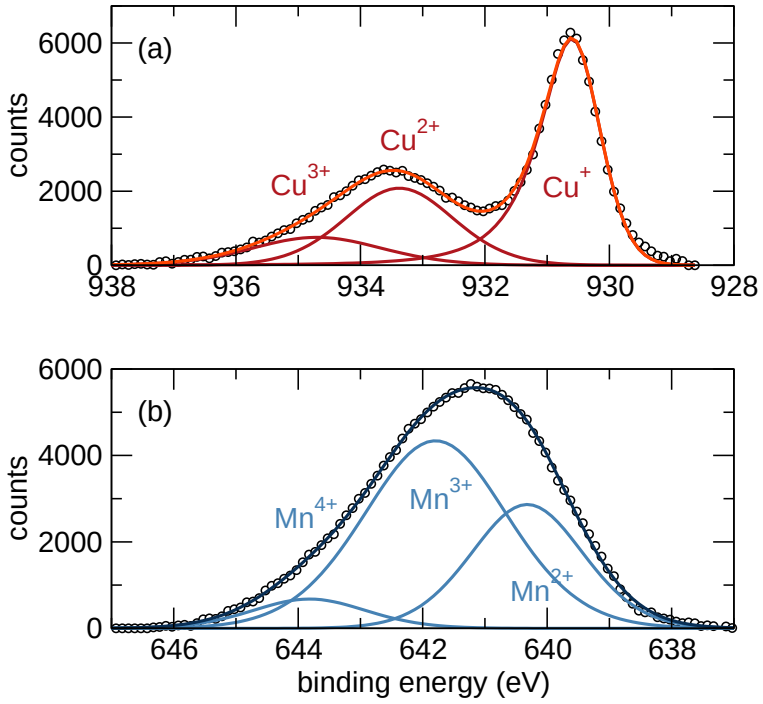

Figure 2.9: X-ray photoelectron spectra (XPS) for the $2p_{3/2}$ region of (a) Cu and (b) Mn cations provides another probe of the mixed valences. Most important is the unambiguous Cu^{+} peak at 934.8 eV is in agreement with the BVS analysis and energy shifts from a comparison between CuO and $NaCuO_2$. [65] Reproduced with permission from reference 59, © 2009 American Chemical Society.

to be mostly 2+, the octahedral Mn is 55% 3+ and 45% 4+. Our RMC BVS results give a cell with a valence of 1.63+ on the A-site and 3.33+ on the B-site. This is a total cation valence of 8.29+ in the formula unit, very close to the expected 8+ expected for $CuMn_2O_4$, despite there being no constraints on total charge imposed on the analysis. The total cation valence for the average Rietveld structure comes to only 6.9+.

Interpretation of the Cu $2p_{3/2}$ XPS spectra in 2.9(a) reveals most readily the large Cu^+ peak at 930.6 eV, which is confirmed by BVS analysis of the RMC supercell to be entirely confined to the tetrahedral sites. Prior XPS studies of $CuMn_2O_4$ have found the same Cu^+ peak for similar heat treatments, and the typical proposed ionic configuration is one of $Cu^+_{0.76}Mn_{0.24}[Cu^{2+}_{0.24}Mn_{1.76}]$ where the tetrahedral Mn can be 2+ or 3+, and the octahedral site Mn will balance with a combination of 3+ and 4+.[46, 66–68] One key distinction between the prior XPS results and those of the BVS is the appearance of B-site Cu^{3+} in the RMC supercell. The broad peaks at 933.4 eV and 934.75 eV have, in the past, been assigned to octahedral and tetrahedral Cu^{2+}, respectively. [66, 69] However, the shift of about 1.3 eV between these two peaks is the same as that between Cu^{2+} and Cu^{3+} in CuO and $NaCuO_2$. [65] It is therefore possible that the highest-energy peak previously assigned to tetrahedral Cu^{2+} is actually that of octahedral Cu^{3+}.

Table 2.2: Stoichiometric amounts per $CuMn_2O_4$ formula unit of the different charge states at the different sites suggested by bond valence sums (BVS). Values within parentheses are percentage of total number in the formula unit. The percentage values obtained from integrated areas of the XPS signals are insensitive to the coordination.

	Cu			Mn		
Charge	Tet. (BVS)	Oct. (BVS)	XPS	Tet. (BVS)	Oct. (BVS)	XPS
1+	0.42 (42%)		47%			
2+	0.20 (20%)	0.10 (10%)	35%	0.34 (17%)		35%
3+		0.28 (28%)	18%	0.05 (2%)	0.89 (44%)	47%
4+					0.72 (36%)	18%

Table 2.2 compares the distributuion of the different ions in their different charge states as suggested by the bond valence analysis of RMC metal-oxygen distances, compared with the integrated areas under the different XPS peaks. While the stoichiometric amounts of Cu^{2+} and Mn^{3+} in the formula units as obtained from the bond valence sums matches closely with the suggested relative amounts from XPS, for the lower and higher valent states of both Cu and Mn, the correspondence is less impressive. A more quantitative spectroscopic study may be called for.

2.4 Conclusions

An ostensibly simple extended compound, $CuMn_2O_4$, is structurally very complex as a consequence of incoherent Jahn-Teller distortions and multiple valence states of the two cations, in conjunction with site disorder. The particular sample examined is tetragonal, quenched from high temperatures, and characterized by near 30% inversion. The compound undergoes glassy magnetic ordering near $T_c = 35\,\mathrm{K}$ to an unsaturated ferrimagnetic state. A combination of neutron scattering and RMC simulations provides a consistent picture of the structure (or more accurately, the positional tendencies of atoms) of a compound that has long provided a challenge to structural and spectroscopic tools. Some of the findings are surprising: Using details of the neighboring metal-oxygen distances and bond valence calculations, we ascertain that the compound tries to minimize the population of JT-active ions on the tetrahedral site, implying charge disproportionation:

$$2\mathrm{Cu}^{2+} \leftrightarrow \mathrm{Cu}^{+} + \mathrm{Cu}^{3+}$$

A similar disproportionation takes place with Mn^{3+}, to lower and higher charge states, both of which are JT-inactive. It is rare to observe stabilization of Cu^{3+} or other high-valence cations in the spinel structure. Normally, one expects to find

Cu^{3+} only in oxides with highly electropositive cations, *e.g.* ACuO$_2$ where A is an alkali cation from Li through Cs. [70, 71] In the spinel, stabilization is achieved because Cu in an octahedral environment can move to a d^8 3+ configuration. These octahedra resist breaking Pauling's third rule–they need not share edges with each other since less than one in six octahedral cations is Cu^{3+}.

This is the first time that bond valence is used to suggest the presence of Cu^{3+} in $CuMn_2O_4$, and this suggestion finds support in x-ray photoelectron spectroscopy – features in the core level XPS of Cu that were previously attributed to differences in coordination, rather than valence states. The use of bond valence in a compound with mixed site occupancies is itself unusual and becomes possible because the modeling allows a statistical analysis of the coordination and bond lengths. Finally, for the first time, it is noted that presence of a large fraction of Cu^{2+} results in the tetrahedra being somewhat flattened, also in an incoherent manner. It is germane to point out that the spinel tetrahedral sites form a diamond lattice, and these are notoriously hard to distort; this has been well studied in the related system of Kagomé lattices.[72] Indeed, in the diamond lattice formed by considering only the averaged positions of tetrahedral cations, all cation-cation distances are equal in $CuMn_2O_4$.

It remains to be seen whether there is evidence for valence-specific local distortions in $CuMn_2O_4$. Future studies may, as an example, geometric analysis

algorithms to describe continuous symmetry measures of a particular polyehdral distortion. [73, 74] These techniques will be discussed in subsequent chapters. Efforts are also under way to incorporate more data and constraints in each RMC simulation, such as x-ray $F(Q)$ and Bragg profile, EXAFS, NMR, or EPR. With so much information within the supercell, a major task is to create well-defined metrics of local distortions and ensure that their presence is statictically supported by multiple simulations.

Chapter 3

Total scattering descriptions of local and cooperative distortions in the oxide spinel $Mg_{1-x}Cu_xCr_2O_4$ with dilute Jahn-Teller ions

The normal spinel oxide $MgCr_2O_4$ is cubic at room temperature while the normal spinel $CuCr_2O_4$ is tetragonal as a consequence of the Jahn-Teller activity of Cu^{2+} on the tetrahedral sites. Despite different end-member structures, complete solid solutions of $Mg_{1-x}Cu_xCr_2O_4$ can be prepared that display a first-order

structural transition around room temperature with composition $x = 0.43$. This chapter details reverse Monte Carlo analysis of total neutron scattering on data acquired between 300 K and 15 K on samples with $x = 0.10$, 0.20, and 0.43 to provide local and average structure descriptions of the samples, including an understanding of the transition from local Jahn-Teller distortions in the cubic phase to cooperative distortions that result in a tetragonal structure.

3.1 Introduction

The propensity of octahedral Cu^{2+} ions in oxide structures to display Jahn-Teller (JT) distortions is intimately linked to magnetism and superconductivity in systems derived from La_2CuO_4. [75, 76] While less common, tetrahedral Cu^{2+} on the A site of oxide spinels can also display JT activity. This distortion lowers symmetry by compressing the tetrahedron and thereby breaking the degeneracy of the partially-occupied t_2 energy levels. [77, 78] The crystal field splittings of the ideal and distorted tetrahedra are shown schematically in Fig. 3.1.

Jahn-Teller distortions themselves are an intriguing theme in functional materials because they enable interplay between electronic and structural degrees of freedom. They have been most widely studied in the manganites, often derivatives of perovskite $LaMnO_3$. [11, 79, 80] In these compounds, Mn^{3+} has

four $3d$ electrons with a singly-occupied pair of e_g states in an octahedral crystal field. It is well established that elongation of the octahedron breaks the degeneracy and lowers the energy of the system. [81, 82] The percolative nature of orbital ordering arising from cooperative JT distortion in doped samples is believed to play a central role in colossal magnetoresistive behavior. [83]

In spinels, collective JT distortions on the A or B sites result in a reduction in symmetry from cubic $Fd\bar{3}m$ to tetragonal $I4_1/amd$ upon orbital ordering at the transition temperature T_{JT}. When only a fraction of occupied sites are JT-active, cation clustering can lead to endotaxial coexistence of tetragonal (distorted) and cubic phases,[84–86] with strain-driven checkerboard patterns first studied in phase-separated CoPt alloys. [87–89] These Mn^{3+}-driven JT distortions are a product of unpaired $3d$ electrons, so self-assembled nanostructured magnetic films are under development. [90]

Few studies have examined the precise JT tendency of Cu^{2+} on the spinel A site. The effect of Cu^{2+} occupancy on T_{JT} and the electronic or magnetic properties remains sparesly investigated. [91–93] We expect there should be key differences between JT activity on the A and B sites of spinel. While BO_6 octahedra are edge-sharing and form a pyrochlore sublattice, the AO_4 tetrahedra are isolated from each other in a diamond sublattice. The increased distance between A cations should hinder their cooperative behavior.

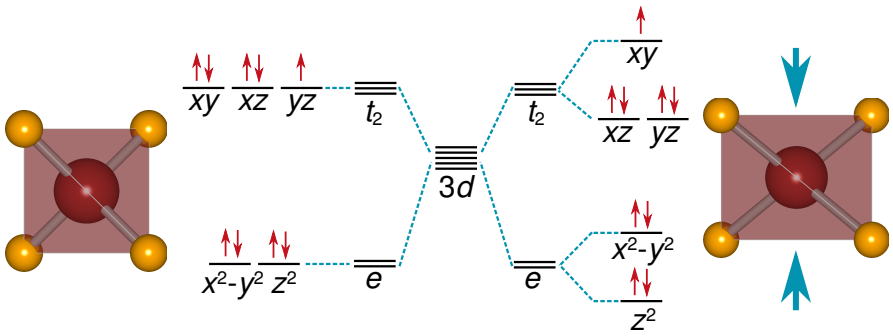

Figure 3.1: Crystal-field splitting of Cu^{2+} with a $3d^9$ electron configuration in an ideal tetrahedron (left) results in degeneracy in the t_2 orbitals. Jahn-Teller compression of the tetrahedron lifts the degeneracy (right), and results in a singly-occupied xy orbital.

In this work, the structural effects of Cu^{2+} concentration x in the spinel solid solution $Mg_{1-x}Cu_xCr_2O_4$ are investigated by real- and reciprocal space structural probes utilizing total neutron scattering. Discrepancies between the average and local structural are of particular interest. Specifically, we probe whether the coordinations of JT-active Cu^{2+} and JT-inactive Mg^{2+} differ. Traditional Bragg diffraction analysis fails to resolve these differences because atoms on the same crystallographic site (here Cu and Mg on the spinel A site) are required to have identical surroundings. Electron paramagnetic resonance [94] and x-ray absorption [95] offer a confirmation that dilute Jahn-Teller cations create local distortions, but these spectroscopic techniques do not yield any detailed structural information. We utilize the pair distribution function (PDF) because it

provides a real-space description of the structure with distinct Cu–O and Mg–O distances.

Our previous work on the spinel $CuMn_2O_4$ encountered many of the complications that make $Mg_{1-x}Cu_xCr_2O_4$ a difficult crystal structure to describe. [59] In that study, Cu and Mn are present with mixed valence on both A and B positions, and the surrounding oxygen polyhedra are cation-dependent. We found that CuO_4 tetrahedra are significantly more distorted (as judged by bond angles) than MnO_4 tetrahedra, and Cu avoids the tendency for JT distortion by disproportionating to Cu^+/Cu^{3+}. The situation for $Mg_{1-x}Cu_xCr_2O_4$ is less complex: no valence mixing is present, and Cu/Mg substitution is confined to the A site. The effect of central cation on MO_4 distortion is more isolated.

We employ large box modeling via reverse Monte Carlo simulations as method of retrieving possible signatures of cation-dependent coordinations from the PDF. [54, 55] Supercells with thousands of atoms can be routinely simulated with modest computational requirements, and the large sample size provides element-specific information due to the presence of many discrete atoms of each type. A crucial aspect of RMC simulations is determining straightforward metrics that describe how local crystalline structure differs from the average. The tendency for distortion of individual polyhedra has been characterized by analyzing bond lengths,[59] bond angles, [59, 96, 97] and geometric analysis. [98, 99]

In this study, tetrahedral JT distortion is gauged using continuous symmetry measures (CSM). [73, 100] The particular strength of the CSM method is its ability to compare the symmetry of imperfect polyhedra, regardless of their size or orientation in space. [101, 102] Extraction of CSM information from RMC simulation was recently performed as a test of structural rigidity in $Bi_2Ti_2O_7$ [103] and is employed here to compare the symmetry of CuO_4 and MgO_4 tetrahedra, thereby describing the preference for JT activity as a function of x and temperature.

3.2 Methods

Powders of $Mg_{1-x}Cu_xCr_2O_4$ compounds were prepared by dissolving stoichiometric amounts of $Cu(NO_3)_2{\cdot}2.5H_2O$, $Mg(NO_3)_2{\cdot}6H_2O$, and $Cr(NO_3)_3{\cdot}9H_2O$ in water, followed by boiling to evaporate the solvent until a brown mass was formed, which was then ground and calcined in air at between 700°C or 1000°C for 10 hours, then cooled at 10°C/min. Laboratory X-ray diffraction patterns were acquired using Cu-K_α radiation on a Philips X'Pert diffractometer at room temperature and a Bruker D8 diffractometer with an Anton Parr high-temperature stage. Magnetic properties were measured using a Quantum Design MPMS 5XL SQUID magnetometer. Time-of-flight (TOF) neutron scatter-

ing was performed on the NPDF instrument at Los Alamos National Laboratory. Rietveld refinements were performed using the XND code[52] for X-ray data and the GSAS-EXPGUI suite[53] for the TOF data. The PDF was extracted using the PDFGETN program[8] with $Q_{max} = 35\,\text{Å}^{-1}$ and least-squares refinement of the PDF was performed using the PDFGUI frontend for PDFFIT2.[10] Crystal structures were visualized with ATOMEYE[57] and VESTA. [58]

Reverse Monte Carlo simulations were run using RMCPROFILE version 6 [18] on $7 \times 7 \times 7$ cubic or $10 \times 10 \times 7$ tetragonal spinel supercells with 19208 or 19600 atoms, respectively. A hard-sphere repulsion was applied to prevent M–O bond distances shorter than the first peak of the PDF, but no clustering was observed at the cutoff distances. No preference for cation clustering was found (as judged by Cu–Cu, Cu–Mg, and Mg–Mg pair correlations), so configurations with randomized Cu and Mg occupancy were used. Simulations were performed as serial jobs on the HP Opteron QSR cluster at the California NanoSystems Institute.

Bond valence sums (BVS) were extracted from atoms in the supercell in the same manner described in our previous work on $CuMn_2O_4$,[59] using the R_0 values of Brese and O'Keeffe.[56] CSM for AO_4 tetrahedra were calculated using a distance measure program provided by M. Pinsky and D. Avnir.

3.3 Results and discussion

3.3.1 Average structure *via* reciprocal-space analysis

The compounds $MgCr_2O_4$ and $CuCr_2O_4$ both belong to the AB_2O_4 spinel family of structures with the A cations, Mg^{2+} and Cu^{2+}, tetrahedrally coordinated by oxygen, while Cr^{3+} lies on the octahedral B site. The [Ar]$3d^3$ electron configuration of Cr^{3+} is very stable because each of the t_{2g} energy levels is singly occupied, so there is no tendency of site mixing or mixed valence. [104] Substituting x in $Mg_{1-x}Cu_xCr_2O_4$ therefore does not disturb the B sublattice composition, but changes in the interpenetrating A sublattice may lead to chemical pressure which will influence its size and shape.

On the tetrahedral A site, Mg^{2+} and Cu^{2+} have effectively identical ionic radii. Both are 0.57 Å as given by Shannon,[105] but their electron configurations are distinctly different. Mg^{2+} has the [Ne] configuration and no d electrons. Cu^{2+} has [Ar]$3d^9$ and only two of the three t_2 energy levels are fully occupied in tetrahedral coordination (Fig. 3.1). This degeneracy causes a JT distortion, manifested by a flattening of the tetrahedron. Bond lengths are preserved, but bond angles are no longer equivalent at 109.5°. [106–108] The contrasting behavior of Mg^{2+} and Cu^{2+} in tetrahedral coordination is evident when

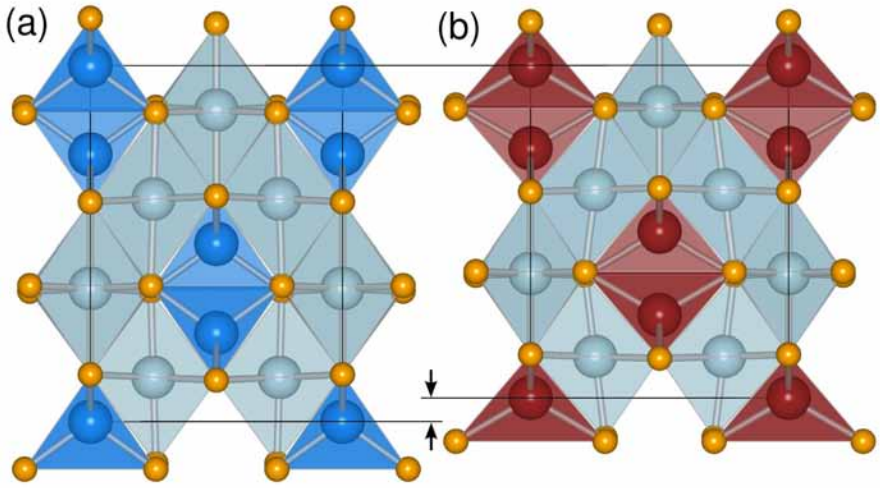

Figure 3.2: To scale, the pseudotetragonal cells of (a) cubic $MgCr_2O_4$ and (b) Jahn-Teller distorted tetragonal $CuCr_2O_4$ are viewed along the a axis of the $I4_1/amd$ cell. Contraction in the c direction is evident due to JT distortion in $CuCr_2O_4$. CrO_6 octahedra are light blue, while MgO_4 and CuO_4 tetrahedra are dark blue and red, respectively.

the $MgCr_2O_4$ and $CuCr_2O_4$ structures are compared in Fig. 3.2. $MgCr_2O_4$ forms in the cubic space group $Fd\bar{3}m$ with ideal MgO_4 tetrahedra.[109] $CuCr_2O_4$ undergoes flattening in the c direction and forms in the tetrahedral space group $I4_1/amd$, which is the same space group as JT distorted Mn_3O_4 (and other AMn_2O_4) or $NiCr_2O_4$.[106, 110] The unit cells are shown to scale in Fig. 3.2 to highlight their difference in dimensions.

Alloying x from 0 to 1 in $Mg_{1-x}Cu_xCr_2O_4$ produces a transition from a cubic to tetragonal spinel. The lattice parameters obtained from Rietveld refinements to room-temperature XRD patterns shown in Fig. 3.3 reveal that for $x < 0.43$ a cubic spinel is formed with a gradually decreasing lattice parameter a. A small region of coexistence occurs for $0.43 \leq x \leq 0.47$, above which the cubic phase disappears. The compound becomes increasingly tetragonal with $c/a < 1$ as the end member $CuCr_2O_4$ is approached, with $c/a = 0.91$ when $x = 1$. The pseudocubic cell volume contracts from 579.4 Å^3 for $MgCr_2O_4$ to 566.1 Å^3 for $CuCr_2O_4$, which is a 2.3% decrease.

We used high-temperature XRD and low-temperature TOF neutron scattering to produce the equilibrium phase diagram of the pseudobinary system $MgCr_2O_4$–$CuCr_2O_4$, shown in Fig. 3.4. The T_{JT} between cubic and tetragonal spinels has a nearly linear relationship on x. There is some phase coexistence determined from HTXRD denoted by the bars on the graph. The transition temperature for

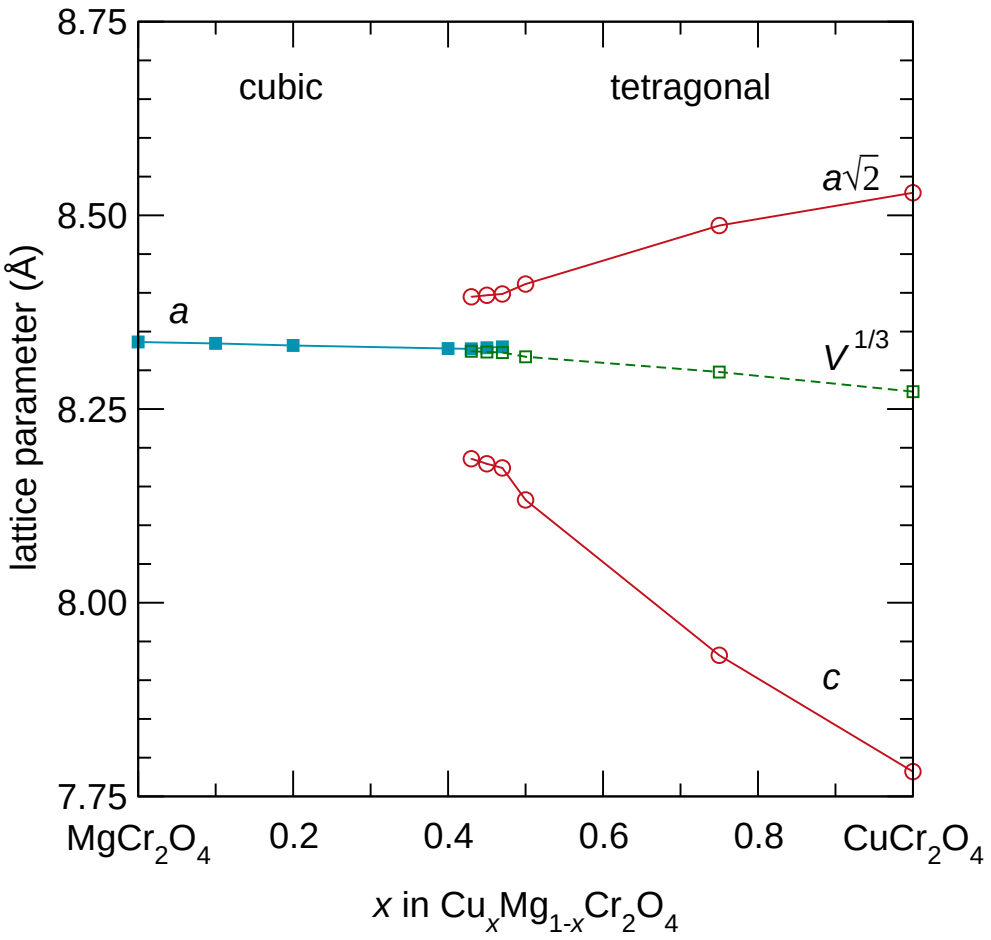

Figure 3.3: Lattice parameters of the $Mg_{1-x}Cu_xCr_2O_4$ solid solution obtained by Rietveld refinement of laboratory X-ray powder diffraction at room temperature. Coexistence of the cubic and tetragonal phases occurs for $0.43 \leq x \leq 0.47$. $V^{1/3}$ is shown for tetragonal phases. Error bars are smaller than the symbols for all points.

$CuCr_2O_4$ was found to be T_{JT} = 630°C, which agrees with the literature. [110, 111] The JT transition temperature steadily decreases with decreasing x to a point where, at T = 15 K, the tetragonal phase occurs for x = 0.20 but not for x = 0.10. Rietveld refinements to neutron scattering data are shown in Fig. 3.5 for three different points on the phase diagram, representing (a) cubic, (b) mixed, and (c) tetragonal phases at x = 0.20 and T = 300 K, x = 0.43 and T = 300 K, and x = 0.20 and T = 15 K, respectively. In all cases, the fits are excellent. There is, however, some unfit diffuse intensity under split tetragonal peaks in (b) and (c), indicative of a more complex crystal structure than the two-phase Rietveld model would suggest.

Not shown on our phase diagram is the tetragonal distortion around 12 K in $MgCr_2O_4$.[112–114] A transition from $Fd\bar{3}m$ to $I4_1/amd$ occurs to remove the geometric frustration of Cr^{3+} spins arranged in a pyrochlore sublattice. Addition of magnetic Cu^{2+} cations in the A sites should relieve this frustration due to strong A-B interactions, [93, 115] so we do not expect the spin-driven distortion to play a role for $x > 0$. The sample with x = 0.10 is cubic at 15 K.

The presence of a tetragonal phase for low Cu^{2+} content is surprising. At x = 0.20, for instance, only one in five A sites has a JT active cation. The A cations are arranged in a diamond sublattice and each has four nearest A neighbors. The tetrahedra do not share edges or corners with each other, with the shortest

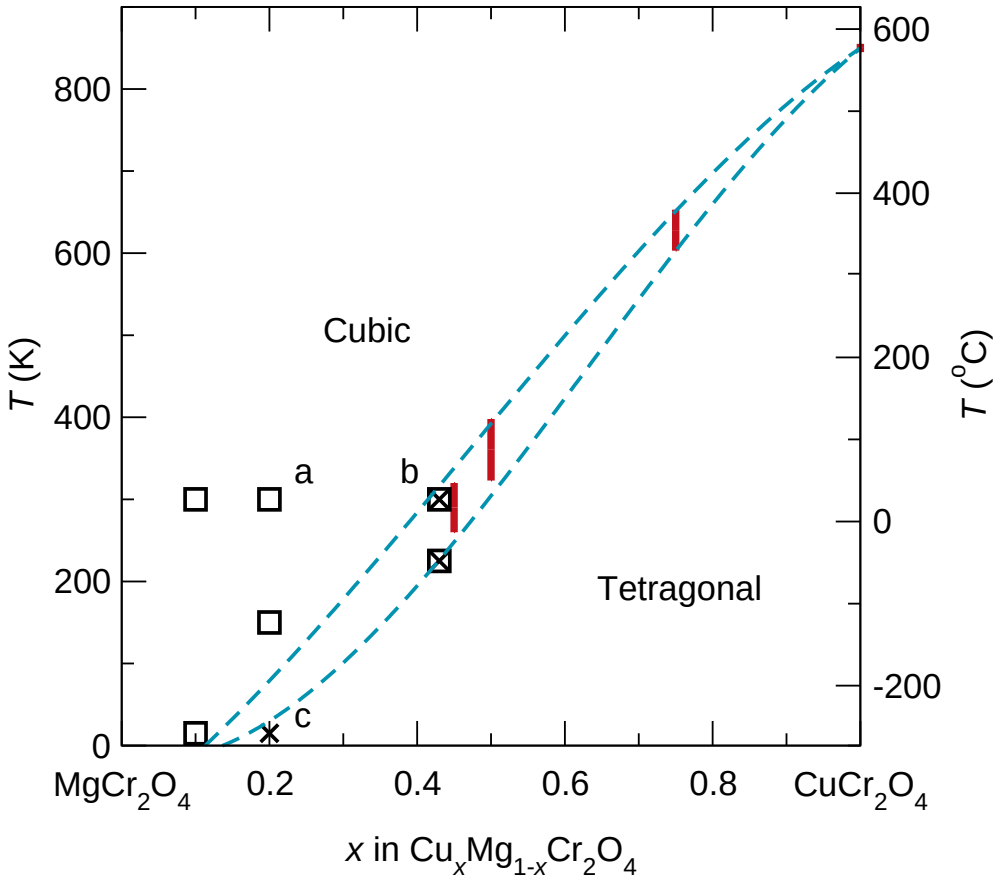

Figure 3.4: Phase diagram of the $Mg_{1-x}Cu_xCr_2O_4$ system as determined by Rietveld refinement. Points denote neutron refinements to cubic (□) and tetragonal (×) phases. Bars represent coexistence regions from high-temperature X-ray diffraction. Letters (a,b,c) correspond to the Rietveld refinements shown in Fig. 3.5

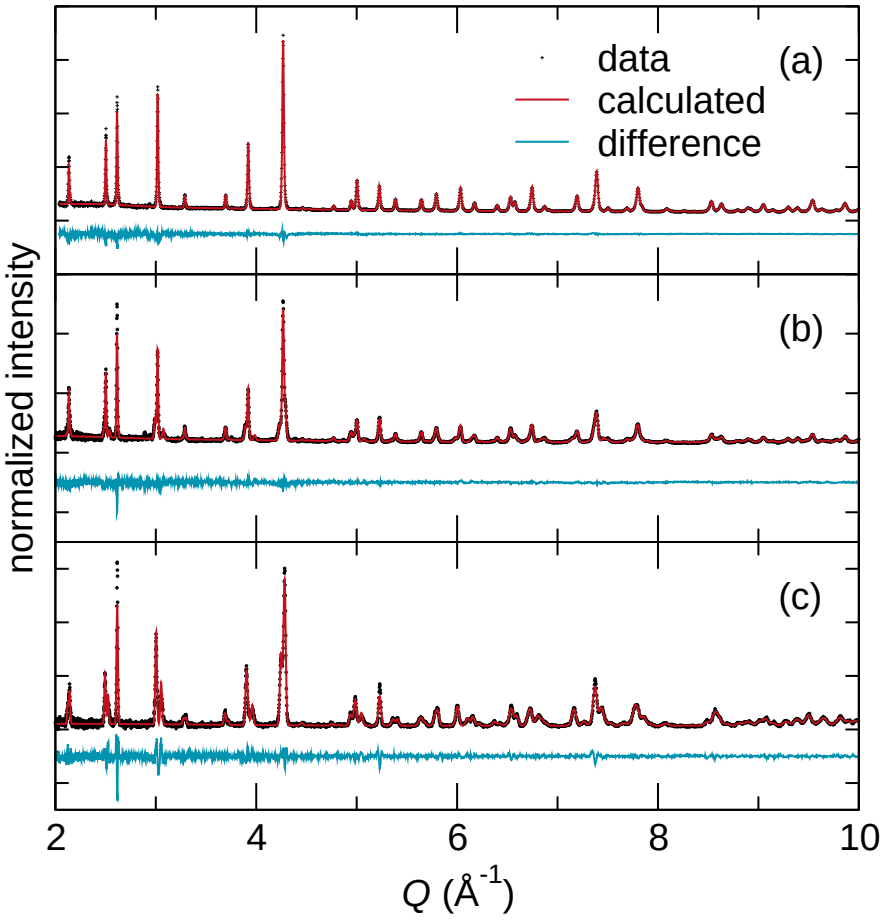

Figure 3.5: Time-of-flight neutron scattering Rietveld refinements of $Mg_{1-x}Cu_xCr_2O_4$ with (a) $x = 0.20$ at 300 K [cubic], (b) $x = 0.43$ at 300 K [cubic and tetragonal], and (c) $x = 0.20$ at 15 K [tetragonal].

exchange pathway being A–O–Cr–O–A. Given a random cation distribution, the probability of one Cu^{2+} having all JT-inactive Mg^{2+} neighbors is $(\frac{4}{5})^4 = 41.0\%$. The probability of having only one Cu^{2+} neighbor is $4(\frac{1}{5})(\frac{4}{5})^3 = 41.0\%$, and the probability of having two Cu^{2+} neighbors falls to $6(\frac{1}{5})^2(\frac{4}{5})^2 = 15.4\%$. Thus 82.0% of Cu^{2+} cations have zero or only one JT-active nearest neighbor, but they still produce orbital ordering with long-range periodicity.

The critical concentration of Cu^{2+} needed to drive a cooperative JT distortion in $Mg_{1-x}Cu_xCr_2O_4$ at 300 K is x = 0.43. This fraction increases with A-site cation radius in ACr_2O_4 spinels: $Zn_{1-x}Cu_xCr_2O_4$ (r_{Zn} = 0.60 Å) is reported to have $x = 0.47$ [116] and $x = 0.58$, [93] while $Cd_{1-x}Cu_xCr_2O_4$ (r_{Cd} = 0.78 Å) has $x = 0.64$. [92] This could be due to increased distance between A-site cations, or a loosening of the structure (thus weakening of strain field produced by a JT distortion).

The critical concentration in $Zn_{1-x}Ni_xCr_2O_4$, [117] where Ni^{2+} drives JT distortion, is around $x \sim 1$ at room temperature. For Cr^{3+} on the spinel B site, less Cu^{2+} is needed to drive a cooperative distortion than Ni^{2+}. The $3d^8$ configuration of Ni^{2+} has only one unpaired t_2 electron, rather than the two of Cu^{2+}. The result is a smaller energy gain after breaking degeneracy and elongation (rather than contraction) of the c axis. [78]

Comparison with JT tendency of Mn^{3+} on the spinel B site is less direct. For example, the solid solution $Zn[Fe_{1-x}Mn_x]_2O_4$ has a critical concentration of about $x = 0.3$, [118] while $Mn[Cr_{1-x}Mn_x]_2O_4$ has $x = 0.4$.[119] This would seem to indicate a stronger JT tendency, in part due to closer B–B distances and edge sharing between octahedra. However, for $Zn_{x/2}Ge_{1-x/2}[Co_{1-x}Mn_x]_2O_4$, Wickham reports $x = 0.65$, [120] and Bhandage reports $x = 0.70$ for $Zn_{x/2}Mn_{1-x/2}[Ni_{1-x}Mn_x]_2O_4$.[121] The wide spread in critical concentrations of Mn^{3+} can be explained by the differences in JT splitting energies found by X-ray absorption spectroscopy on AMn_2O_4 spinels by Noh, *et al*. [95] In essence, the energy drop from JT distortion around Mn^{3+} on the spinel B site is very senstive to changes in chemical pressure.

We obtain the *cooperative* behavior of the averaged lattice using Rietveld refinement. We do not necessarily resolve the distinct cation coordinations of Mg^{2+} and Cu^{2+} if they are different on the local, atomic length scale. Two views of the JT transition can be proposed: in the case of a sharp crossover, as would be implied by how Rietveld analysis is performed, all AO_4 tetrahedra are equivalent whether they contain Mg^{2+} or Cu^{2+}, and upon increasing x they abruptly transform from ideal tetrahedra in the cubic spinel to flattened tetrahedra in the cooperatively JT distorted spinel. In the second case, the CuO_4 tetrahedra are *always* locally JT distorted (even for values of x where the spinel is cubic)

but the crossover at $x = 0.43$ at room temperature represents the point where they cooperatively order and the JT distortions percolate through the long-range structure.

3.3.2 Magnetic properties

$MgCr_2O_4$ and $CuCr_2O_4$ have markedly different magnetic behavior due to the addition of unpaired spins in Cu^{2+} and the accompanying JT distortion. $CuCr_2O_4$ is a hard ferrimagnet with $T_C = 135$ K,[122] while $MgCr_2O_4$ undergoes complex antiferromagnetic ordering below $T_N = 16$ K.[114, 123] Macroscopic composites of a ferromagnet and antiferromagnet would result in a traditional exchange biased material, with an enhanced coercive field H_C and an exchange bias field H_E, manifested as a shift of the hysteresis loop in the $-H$ direction. [124–126]

The $Mg_{1-x}Cu_xCr_2O_4$ solid solution is a mixture on the atomic level, but nevertheless exhibits the magnetic hallmarks of an exchange biased system. The hysteresis loop of the $x = 0.43$ sample in Fig. 3.6 at $T = 5$ K has $H_C = 8.4$ kOe. Cooling with a field $H_{FC} = 50$ kOe broadens the hysteresis loop and shifts it in the $-H$ direction by $H_E = 0.44$ kOe. This shift signifies the preference for the ferrimagnet to align along the field-cooling direction. H_C and H_E decrease with the Cu^{2+} concentration x, as does the onset of magnetic ordering. These trends

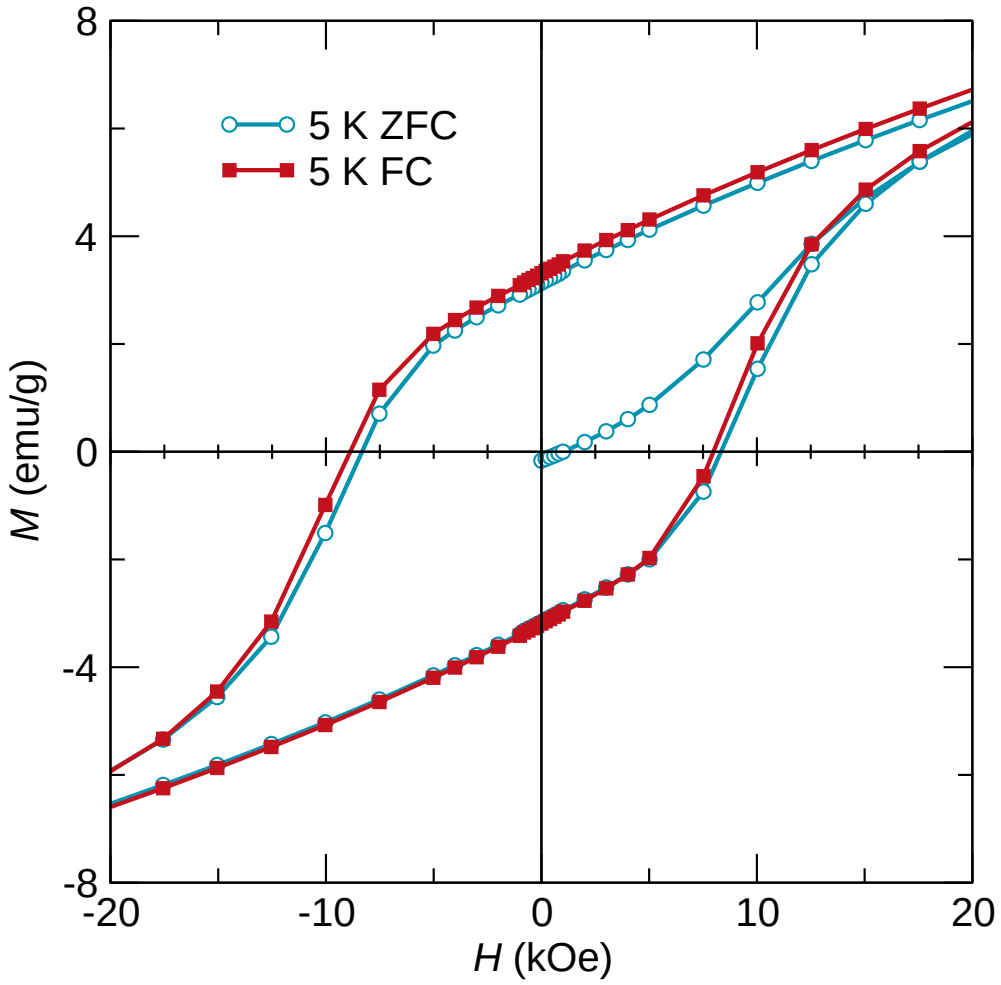

Figure 3.6: Magnetic hysteresis of $Mg_{1-x}Cu_xCr_2O_4$ with $x = 0.43$ at $T = 5$ K after zero-field cooling (ZFC) and field cooling (FC) with $H_{FC} = 5$ T. The shift in the $-H$ direction when $M = 0$ is the exchange bias field H_E.

are shown in Fig. 3.7. In all cases, field-cooling increases H_C and results in the appearance of a significant H_E. We find $H_E = 0$ in all samples after zero-field cooling.

Exchange bias is traditionally manifested by pinning at the interface between a ferro- or ferrimagnet and antiferromagnet after field cooling when $T_C > T_N$. It can also arise from intrinsic disorder in a single-phase system, or the presence of disordered spins from either a spin glass or uncompensated surface spins on small particles (which behave in a glassy manner themselves). [127, 128] In the $Mg_{1-x}Cu_xCr_2O_4$ system, the magnetic behavior cannot be fully described by traditional AFM-FM interplay between $MgCr_2O_4$ and $CuCr_2O_4$ because the onset of H_E when $x = 0.43$ in Fig. 3.7(d) occurs above $T = 20$ K, which is above the Néel temperature of $MgCr_2O_4$. Therefore the disordered solid solution contains some regions of heterogeneity which may behave as glassy moments or as some intermediate AFM phase. Either of these cases can produce exchange bias. [93, 129] A more detailed investigation of the magnetism, as was performed on $Zn_xMn_{3-x}O_4$, [130] would be needed to elucidate how the competing magnetic interactions produce exchange bias behavior as a function of Cu content x. The phenomenon of JT-active cation clustering has been investigated by dilatometry, [131] but its effects on magnetism have not been explored in detail.

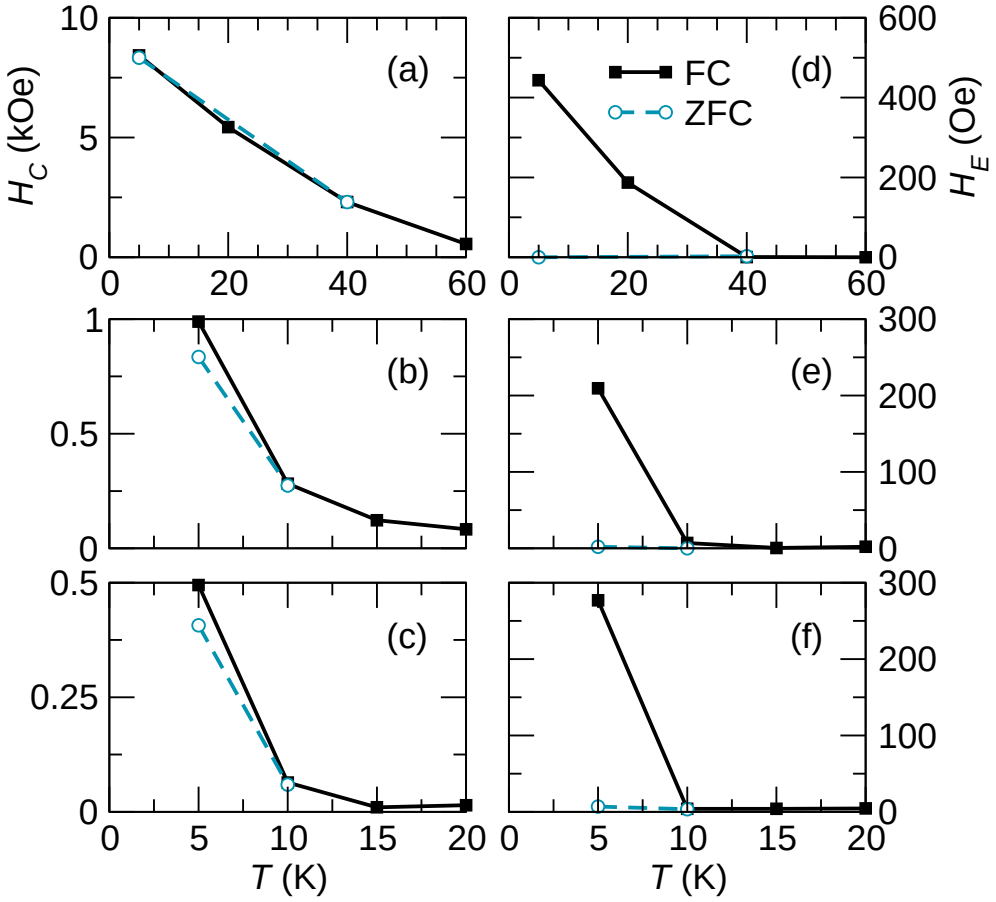

Figure 3.7: (a-c) Coercive fields H_C and (d-e) exchange bias fields H_E for $Mg_{1-x}Cu_xCr_2O_4$ samples with $x = 0.43$ (a,d); $x = 0.20$ (b,e); and $x = 0.10$ (c,f) after ZFC and FC with $H_{FC} = 5$ T. In all cases, ZFC results in a smaller H_C and gives $H_E = 0$.

3.3.3 Local structure *via* real-space analysis

The average structure model of $Mg_{1-x}Cu_xCr_2O_4$ from Rietveld refinement indicates that the compounds exist as single phases, either cubic or tetragonal, apart from the two-phase coexistence region around T_{JT}. When modeled using a single unit cell, Mg^{2+} and Cu^{2+} are required to share the same crystallographic site and their surroundings are necessarily identical. This model often inadequately describes the true structure of compounds where energy-lowering changes in cation coordination are known to persist above the average structural transition temperature as in perovskite manganites and cobaltites. [11, 80, 132, 133] The PDF has emerged as a key tool for measuring these local distortions that do not possess long-range order. Because the PDF is a weighted histogram of all atom-atom distances in the sample, it is sensitive to the distinct bond distances that are produced by dissimilar coordination of multiple chemical species on the same site. [59] We investigate whether the PDF shows any signature of distinct Cu^{2+} and Mg^{2+} coordination.

Least-squares PDF refinements can be performed using the average structure unit cells from Rietveld refinement as a starting point. Fits to the $x = 0.20$ data at 300 K are shown in Fig. 3.8. Panel (a) shows the fit to a Rietveld-refined cubic unit cell with split 0.20/0.80 occupancy of Cu^{2+} and Mg^{2+} on the same

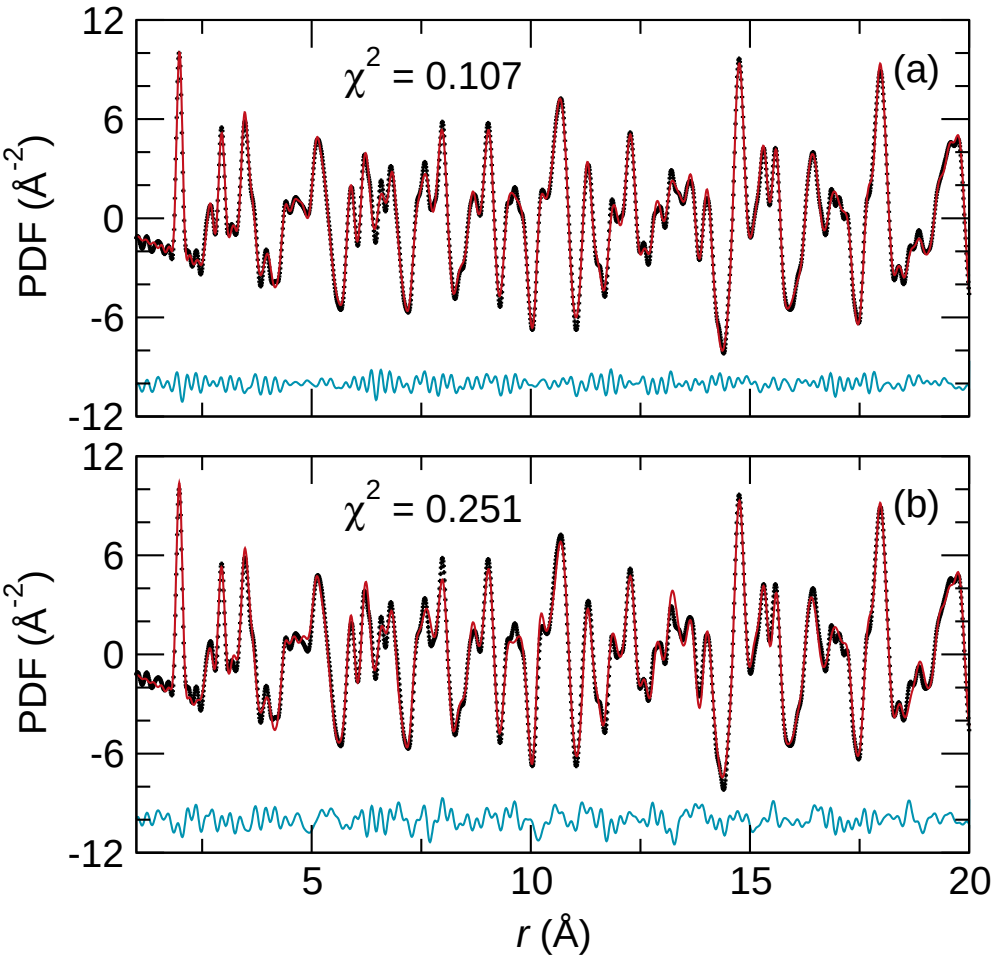

Figure 3.8: Least-squares fits to the PDF for $x = 0.20$ at 300 K for the (a) cubic spinel phase with fractional-occupancy obtained from Rietveld refinement, and (b) an 80-20 fit to the end members $MgCr_2O_4$ and $CuCr_2O_4$.

crystallographic site. In (b), we fit using a 0.20/0.80 linear combination of the $MgCr_2O_4$ and $CuCr_2O_4$ end members with lattice parameters allowed to refine. The fit is good despite the use of a tetragonal unit cell to model a structure far above T_{JT}, but it does not improve on the fit using a single cubic unit cell. The ability to distinguish Mg and Cu is hindered by their similar neutron scattering lengths: 5.38 and 7.71 fm, respectively. [134] For $x = 0.20$, least-squares PDF fits do not definitively prove that there are distinct (or identical) coordination environments for Mg^{2+} and Cu^{2+}.

Resolution of distinct cation environments is aided when $x = 0.43$ due to approximately even concentrations of Cu^{2+} and Mg^{2+}. At 300 K, Rietveld refinement found coexistence of the cubic and tetragonal phases. Neither phase alone can be used to produce a satisfactory fit to the PDF. A two-phase fit using the Rietveld refined cells is shown in Fig. 3.9(a), and agrees quite well with the data. As with the $x = 0.20$ sample, we also fit the data to a combination of the end members $MgCr_2O_4$ and $CuCr_2O_4$ in Fig. 3.9(b). Again, the fractional occupancy Rietveld result produces a better fit than the end members. The least-squares fits indicate that the average structures produce excellent representations of the local structures, but they do not definitively show whether the Mg^{2+} and Cu^{2+} coordination environments are distinct or similar.

Least-squares fits to the PDF are required to specify how many distinct AO_4

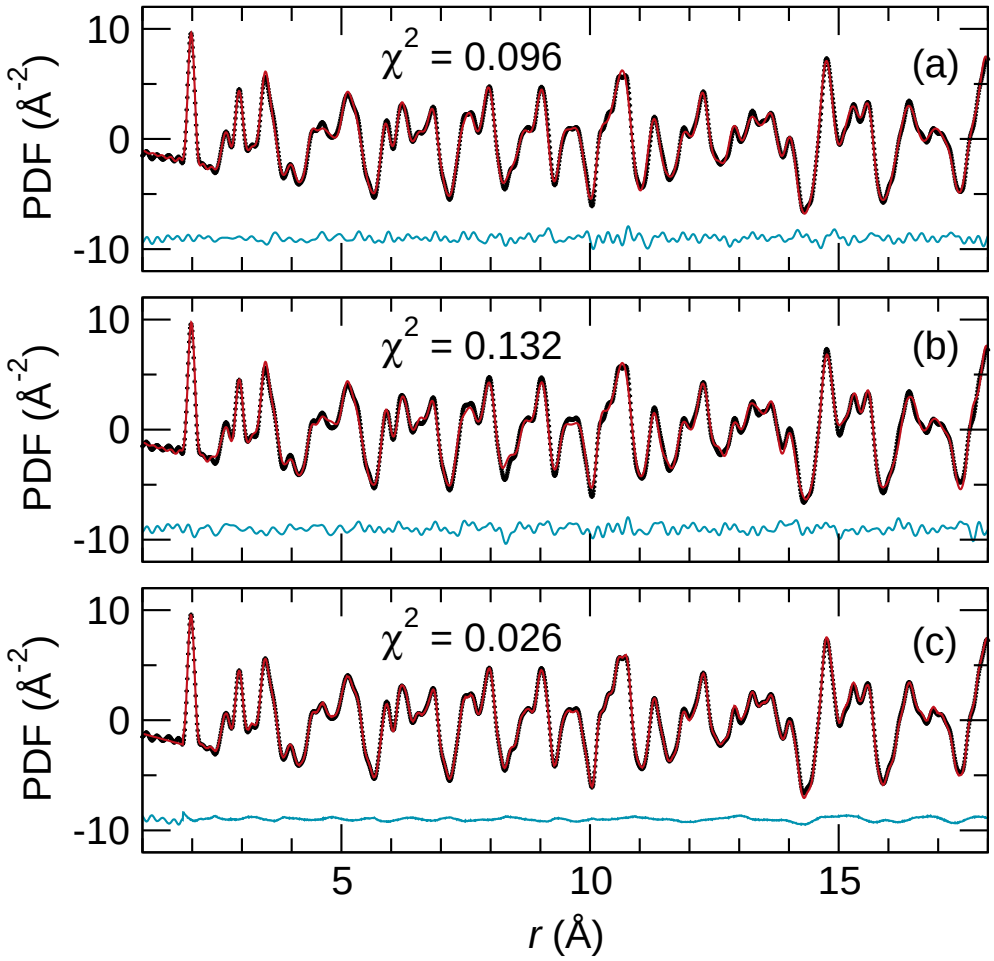

Figure 3.9: Fits to the PDF for $x = 0.43$ at 300 K for (a) least-squares refinement of the two fractional-occupancy phases found from Rietveld refinement, (b) least-squares refinement using the end members $MgCr_2O_4$ and $CuCr_2O_4$, and (c) the fit after RMC simulation.

environments to allow, much like in a Rietveld refinement. The $Fd\bar{3}m$ and $I4_1/amd$ unit cells provide only one AO$_4$ environment per phase. There is no way to define cation-dependent coordination without manually building a lower-symmetry unit cell. In order to investigate the AO$_4$ environment directly, we remove the symmetry constraints of least-squares PDF analysis and utilize large-box modeling via reverse Monte Carlo (RMC) simulations. This method has proved to be useful for investigating atomic structure on the local level, especially in cases where long-range periodicity is not present, such as $SrSnO_3$,[99] $Bi_2Ti_2O_7$,[103] and β-cristobalite. [135]

The RMC supercell for an $x = 0.20$ sample at 15 K is inspected by folding each of the unit cells back into a single box, shown in Fig. 3.10, which reveals how each crystallographic site is decorated with atoms. The supercell contains 560 Cu and 2240 Mg atoms that are randomly arranged. Because there are a large number of distinct Cu and Mg atoms, statistical analysis can be used to investigate whether there is any evidence for the local AO$_4$ distortion to depend on the central cation. Bond valence sum histograms shown in Fig. 3.11 show that both the A cations have valences peaked around the expected value of A^{2+}, and the B site shows only Cr^{3+}, which implies that our supercells contain chemically reasonable bond lengths.

No cation dependence of AO$_4$ bond distances is obvious from partial radial

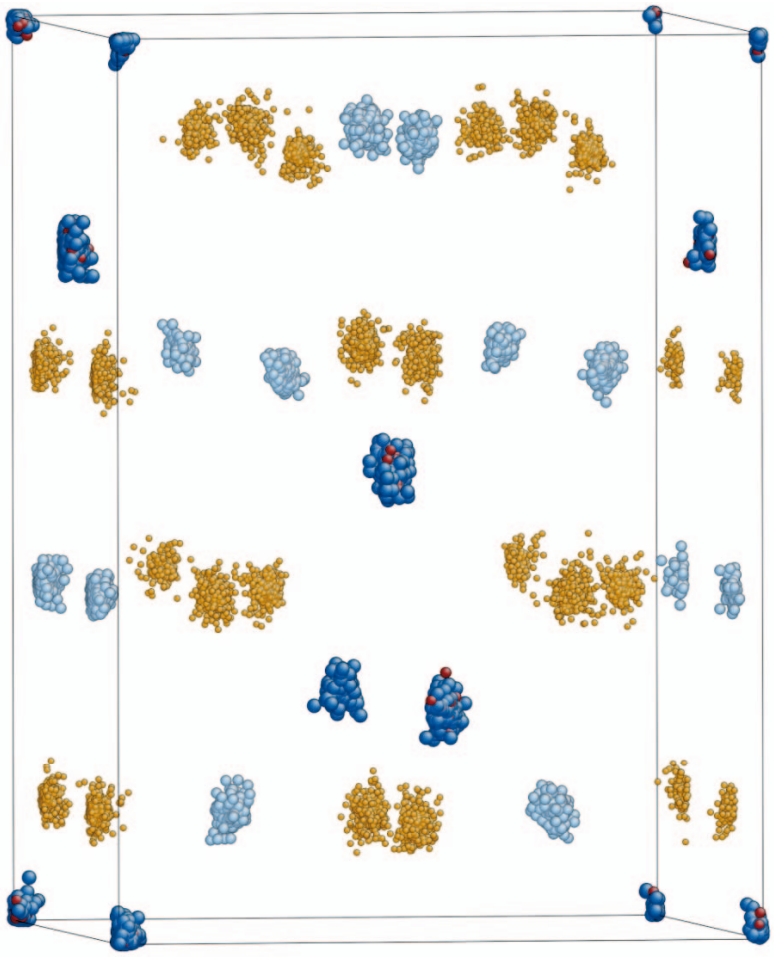

Figure 3.10: The final $10 \times 10 \times 7$ RMC supercell for an $x = 0.20$ simulation is folded into a single unit cell to obtain point clouds at each crystallographic site. Atoms shown are Cu (red), Mg (dark blue), Cr (light blue), and O (orange).

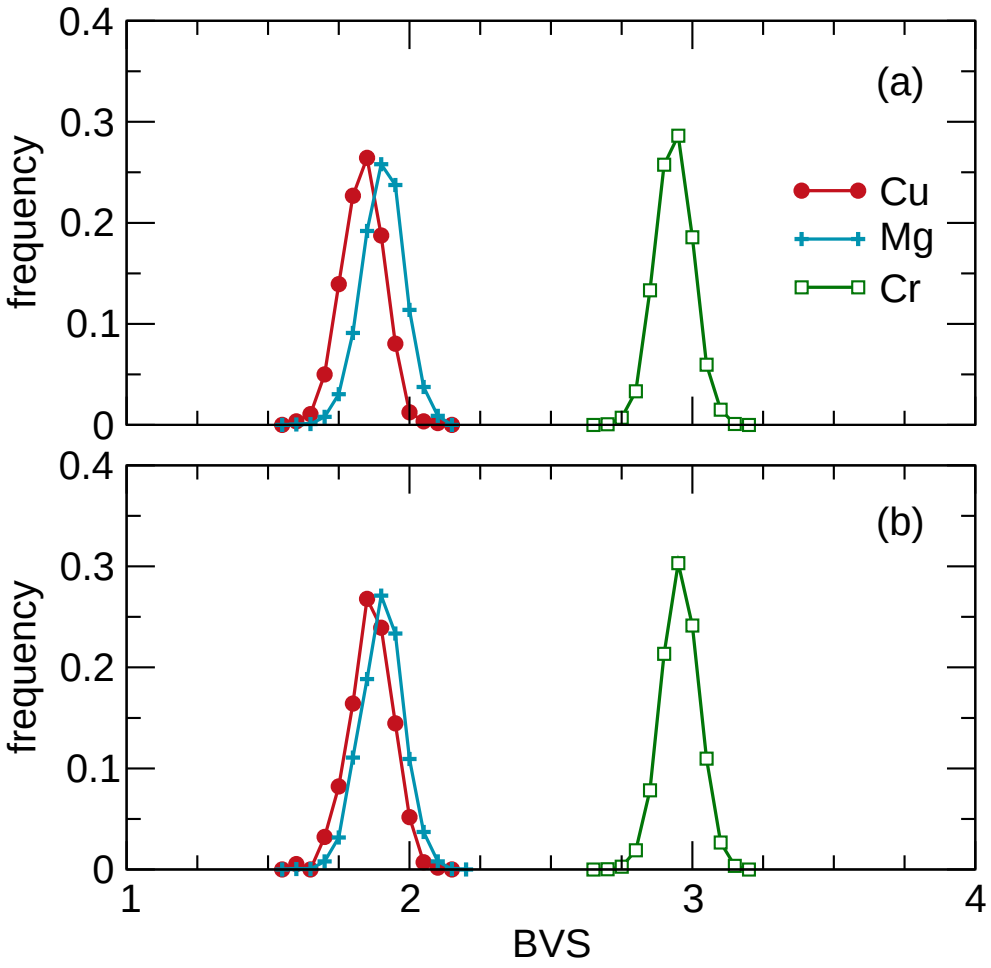

Figure 3.11: Bond valence sums for Cu and Mg extracted from $Mg_{1-x}Cu_xCr_2O_4$ RMC supercells $x = 0.20$ after fits to data at $T = 300$ K (a) and 15 K (b). Aside from a slight broadening at 300 K, the distributions are comparable.

distributions $g_{Cu-O}(r)$ and $g_{Mg-O}(r)$. This is to be expected because Mg^{2+} and Cu^{2+} have the same ionic radius when tetrahedrally coordinated. Neither is there any apparent distinction between CuO_4 and MgO_4 tetrahedra based upon O–A–O bond angles, in contrast to our previous study on $CuMn_2O_4$.[59]

We use the continuous symmetry measure (CSM) technique to gauge the tendency for JT distortion of AO_4 tetrahedra. The CSM technique provides a distance measure (DM) of a given tetrahedron that indicates its deviation from ideality. [73, 100] A perfect tetrahedron has DM = 0, and any distortion increases the value of DM. In the end member compounds, MgO_4 has a DM = 0 while CuO_4 has a DM = 0.0076. Having thousands of distinct tetrahedra in the RMC supercell affords the opportunity to produce a histogram of DM (Fig. 3.12) for all tetrahedra depending on the central cation. Each panel contains eight lines: four for each cation, resulting from four independent RMC simulations. The overall shape of each histogram describes the average distortion (peak center) and the tightness of the DM distribution (peak width) at each value of x and T. No tetrahedra are present with exactly DM = 0 because stochastic RMC simulations leave no atomic positions untouched–even a compound with ideal tetrahedra would have the shapes subtly distorted.

At 300 K, the spread of distortions increases for $x = 0.43$ because the average structure becomes a mixture of cubic and tetragonal phases. In the series

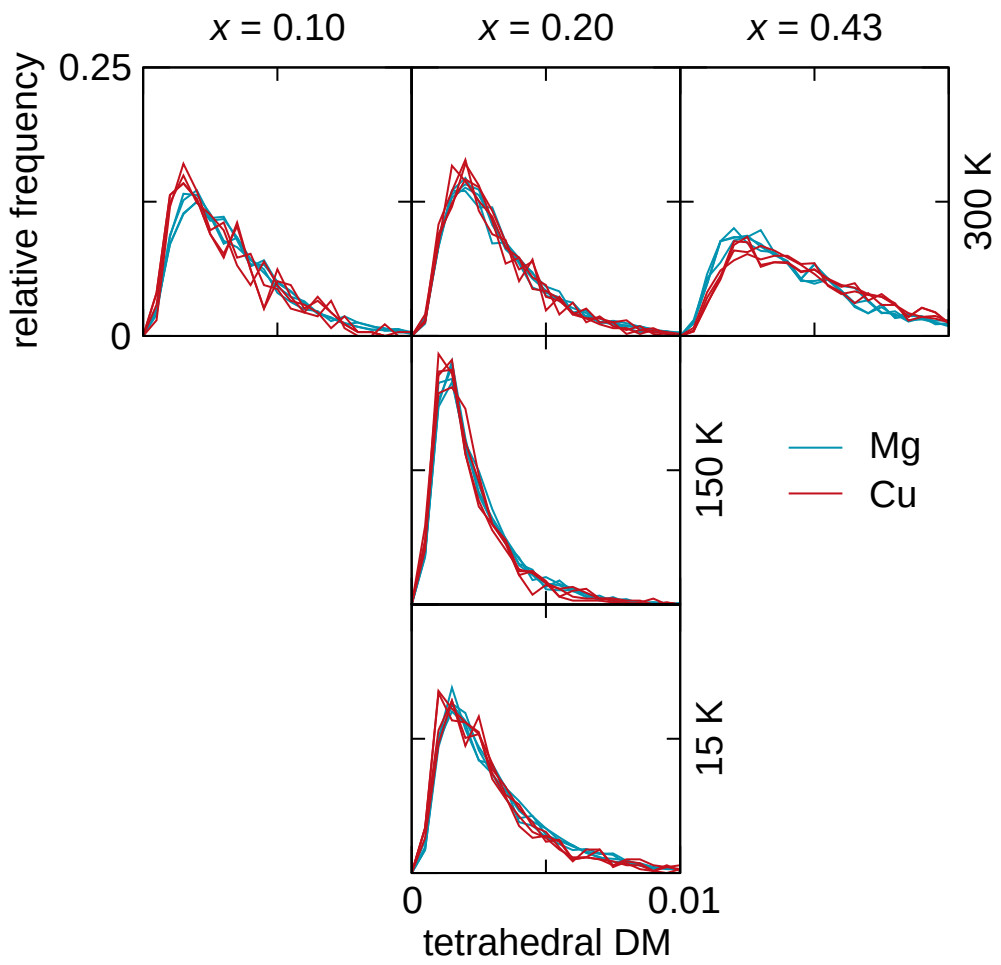

Figure 3.12: CSM histograms from RMC simulations for three Cu contents and three temperatures. Each pane contains 8 distributions: one Cu and one Mg for four independent simulations. Broadening of the peaks indicates a large distribution of tetrahedral distortions.

where x = 0.20, the peak sharpens upon cooling to 150 K, which we attribute to a reduction of thermal vibrations. This trend would continue to low temperature in the absence of JT distortion. Instead, the peak broadens at 15 K, most likely due to the transition to a tetragonal phase. These histograms provide a view of the average tetrahedral shape, but no distinction between Mg and Cu is apparent. We find that cumulative distributions offer a clearer picture of this dependence.

The cumulative distributions in Fig. 3.13 do not show separation between the Cu and Mg curves in the x = 0.10 or 0.20 samples. However, the x = 0.43 sample shows a clear distinction, with Mg tetrahedra possessing DM that are closer to zero (more ideal) than Cu. This is clear evidence for the tendency of Cu to undergo JT distortion while Mg remains more symmetric.

Overlapping DM curves for x = 0.10 and 0.20 do not preclude the possibility of distinct CuO_4 and MgO_4 tetrahedra in those samples. There may be insufficient resolution in the PDF to distinguish the cations due to their similar neutron scattering cross sections and the relatively low concentration of Cu^{2+}. It remains unclear whether distinct cation environments are only seen around x = 0.5 (due to approximately even cation concentrations) and if the distinction would disappear as $x \rightarrow 1$. Temperature dependence of the CSM when x = 0.43 may also provide some insight into the dynamics of these distortions. Substitut-

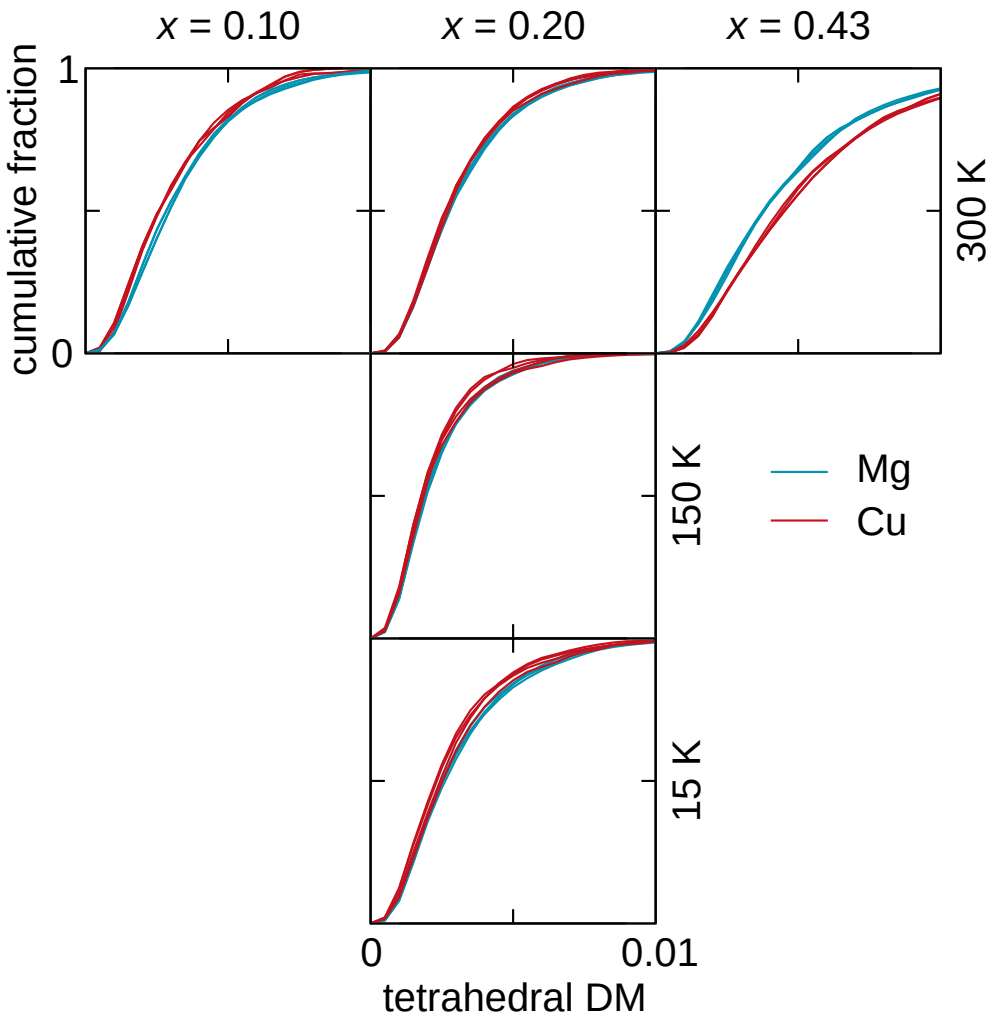

Figure 3.13: Cumulative CSM distributions are similar enough from run to run that most lines overlay each other. Only the $x = 0.43$ run has a clear distinction between CuO_4 and MgO_4 tetrahedron shape, with MgO_4 distinctly more ideal than CuO_4.

ing a JT-inactive A site cation with a different neutron scattering cross length, such as Mn^{2+} or Co^{2+}, may aid contrast with Cu^{2+}.

3.4 Conclusions

We find that the solid solution $Mg_{1-x}Cu_xCr_2O_4$ has a two-phase coexistence of cubic and tetragonal phases at room temperature for $0.43 \leq x \leq 0.47$. Tetragonality is induced by increasing JT activity in tetrahedrally coordinated Cu^{2+}. The average structure descriptions from Rietveld refinement provide an adequate description of the structures across the range of x and temperature. This is corroborated by the magnetic behavior, which indicates a disordered atomic mixture. The $x = 0.20$ sample is cooperatively JT distorted with orbital ordering at 15 K despite 82% of all Cu^{2+} having zero or only one Cu^{2+} neighbors.

Least-squares PDF refinements achieve good fits using the models from Rietveld refinement, implying that it is difficult to improve on models where CuO_4 and MgO_4 are equivalent. Still, bond valence calculations show that RMC simulations produce better fits to the data while retaining chemically reasonable bond distances. The AO_4 tetrahedral distortion increases with x as judged by CSM. The absence of distinct CuO_4 local distortions in the low-x CSM histograms does not prohibit their existence. One sample with $x = 0.43$ shows tetrahedral

DM that indicate distinct coordination of Cu^{2+} versus Mg^{2+}. We expect this technique to resolve the cation-dependent JT distortions (even when they are incoherent) in materials where significant contrast between cations exists.

Chapter 4

Real space investigation of structural changes at the metal-insulator transition in VO_2

4.1 Introduction

VO_2 undergoes a transition from a metal to a non-magnetic insulator upon cooling below 340 K.[137] Accompanying this transition is a structural change from the high temperature tetragonal phase to a low temperature monoclinic

[1]Portions of this chapter have been published in reference 136 © 2010 by the American Physical Society

phase, where pairing and tilting of vanadium ions result in chains with alternating long and short V–V distances along the c-axis (Fig. 4.1).[138–140] The mechanism underpinning the insulating behaviour of the low temperature phase continues to attract widespread interest, and recent work suggests the simultaneous role of the V–V pairing and electron correlation to drive the system from a correlated metal to a slightly less correlated insulator.[141–143] Diverse methods have been used to understand this transition, including recent probes of dynamics and techniques sensitive to spatial inhomogeneities.[144–147] The phenomenon as it occurs in nanostructures is also receiving increasing attention.[148–150]

Above 340 K, the rutile VO_2 structure in space group $P4_2/mnm$ has a single near-neighbor V–V distance of 2.88 Å.[151, 152] Below 340 K, the monoclinic structure in space group $P2_1/c$ is characterized by V–V dimers along the c-axis displaying two distinct V–V distances: 2.65 Å and 3.12 Å.[152–154] The structures are displayed in Fig. 4.1. Interestingly, several recent papers address the formation of domain-like regions in monoclinic VO_2 on approaching the transition temperature from below.[143, 145, 155, 156] An unresolved question regarding the nature of these domains is whether they are associated with an intermediate phase formed during the transition. A second question concerns the possible existence of dimers, albeit over short length scales, persisting in the

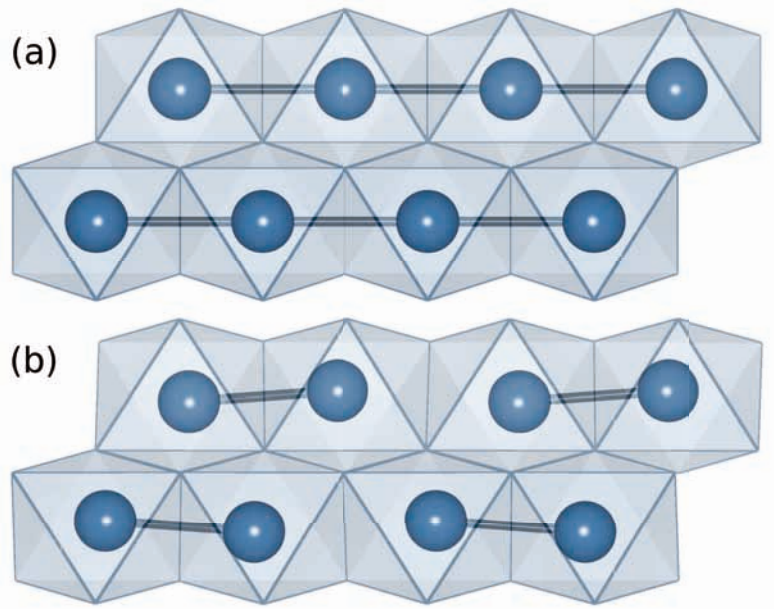

Figure 4.1: (a) The metallic high temperature tetragonal rutile form of VO_2 with a single V V distance and (b) the insulating low-temperature monoclinic form, showing dimerized chains of alternating short and long V V distances along the c-axis. Reproduced from reference 136, c 2010 by the American Physical Society.

metallic high temperature phase.

Here we employ synchrotron X-ray total scattering in conjunction with real-space analysis—using least-squares and reverse Monte Carlo methods—to show that the transition from the low-temperature monoclinic to the high temperature tetragonal phase in rutile VO_2 occurs in a first-order manner, with coexistence of the low and high-temperature phases at the transition temperature. We employ pair distribution function (PDF) analysis, which has emerged in recent years as an indispensable tool for probing and understanding structural changes, and specifically, the range-dependence thereof.[11, 157–159] The advantages of the PDF method lie in its ability to probe structural changes that lack long range correlations, which are not captured by Bragg peaks in X-ray or neutron scattering. By analyzing PDF data with large-box reverse Monte Carlo (RMC) simulations, we are able to produce a supercell where the local environment is free from symmetry constraints of the high or low temperature structures.[59, 99, 103] Atomic positions can therefore relax to best fit the experimental data, which includes both the Bragg and diffuse components. This approach provides an opportunity to observe any continuum of atomic positions which might exist across the metal-to-insulator transition in VO_2.

4.2 Methods

Phase pure VO_2 powders were prepared in evacuated and sealed silica ampoules from a stoichiometric mixture of V_2O_5 (99.9%, Alfa Aesar) and V_2O_3, the latter obtained by reduction of V_2O_5 in 5%-H_2/N_2 gas at 900°C. Synchrotron total scattering data on powders in Kapton tubes were collected in transmission mode at beamline 11-ID-B of the Advanced Photon Source at Argonne National Laboratory by using X-rays with energies near 90 keV (wavelength λ = 0.13702 Å). Samples were heated and cooled continuously from 250 K to 400 K at a rate of 50 K h^{-1} using an Oxford Cryosystems Cryostream 700. Scattering data were collected on an image plate system with a sample-to-detector distance of 250 mm. Raw images were processed using FIT2D.[160] PDFs were extracted as $G(r)$ using PDFGETX2 with Q_{max} = 25 $Å^{-1}$.[9] Least-squares profile refinements were carried out using PDFGUI.[10] RMC simulations were performed using RMCPROFILE[18] with a $10 \times 10 \times 16$ supercell, starting from atomic positions of the tetragonal structure. The simulations were constrained by the PDF (where $G(r)$ above corresponds to $D(r)$ as described by Keen [20]) up to r = 25 Å. RMC results shown in this work are averages of many simulations to ensure an unbiased representation of the fit to data.

4.3 Results and discussion

Least-squares refinements to all the PDFs at 2 K intervals were performed using both monoclinic and tetragonal structures [Fig. 4.2(a) and (b), respectively]. In the case of data fit to a monoclinic structure [Fig. 4.2(a)], we obtain a good fit from $T = 250$ K to 338 K. The high temperature tetragonal structure [Fig. 4.2(b)], results in a good fit to the data from $T = 342$ K to 400 K. The PDFs of the two structures are markedly different as seen in Fig. 4.2(a,b). There are no significant changes (other than lattice constants) in either end member until the transition is reached. The sudden structural transition at $T = 340$ K is evident in plots of the goodness-of-fit parameters R_w to the high and low temperature structures as seen in Fig. 4.2(c). In addition to locating the transition itself, the evolution in both temperature regimes suggest pure, single-phase polymorphs of the VO_2 end members. There is no broad hysteresis in the transition because the measurement allows thermal equilibrium to be reached at each point. In addition, the sample is a bulk powder of large crystallites, which implies the possibility of many concurrent nucleation events.

Dimerization of the V cations leads to splitting of the $2a$ Wyckoff site in the tetragonal VO_2 structure. If a dimerized structure is fit using the high-temperature model, the structural changes must be accommodated by an in-

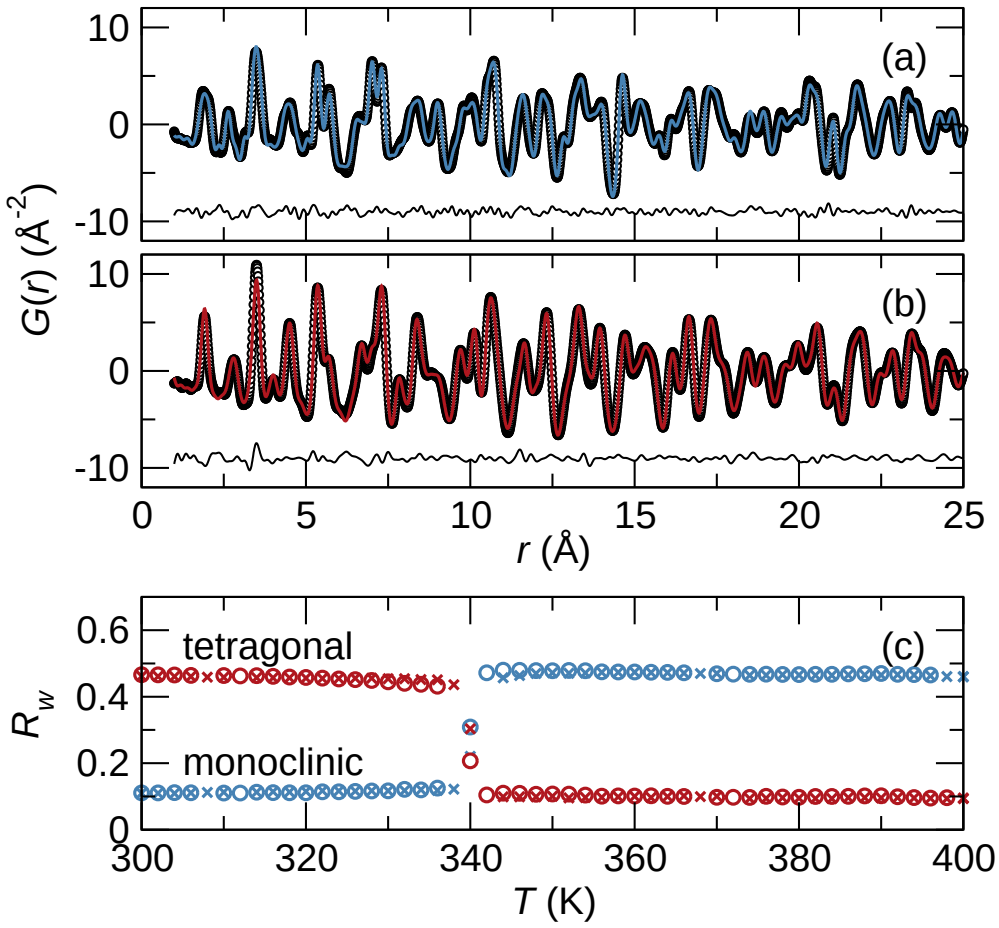

Figure 4.2: Least-squares fits to the PDF of bulk VO_2 using (a) the low temperature monoclinic structure for $T = 300\,\mathrm{K}$ (R_w, 11.6%) and (b) the high temperature tetragonal structure for $T = 400\,\mathrm{K}$ (R_w, 9.6%). Circles are experimental data and lines are fits to the average structure. The difference is displayed below each fit. (c) Changes in the R_w fitting parameters, shown for cooling ($\circ$) and heating ($\times$) through the transition temperature, show an abrupt transition with good fits at all temperatures outside of $T = 340$ K. Reproduced from reference 136, © 2010 by the American Physical Society.

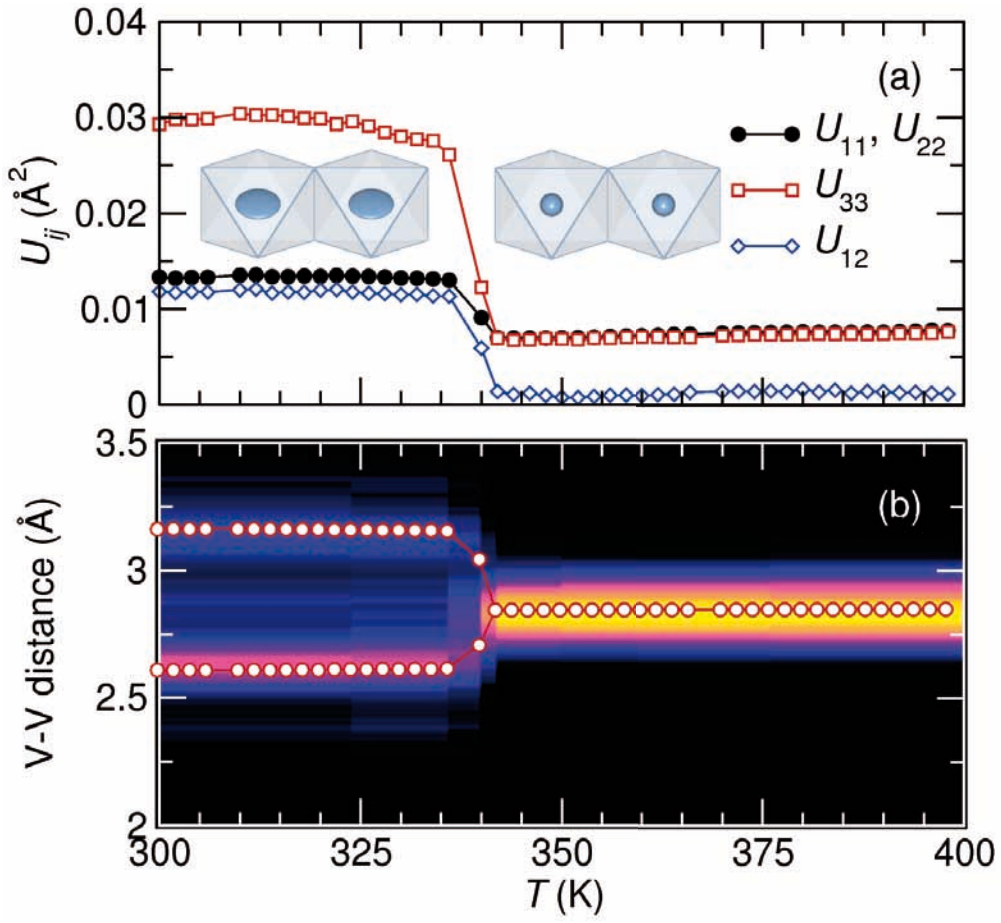

Figure 4.3: (a) Thermal parameters (U_{ij}) obtained from PDF least-squares re nement as a function of temperature reveal abrupt changes at the transition temperature. Thermal ellipsoids (99%) for neighboring V polyhedra in the c direction are shown above and below the transition temperature. (b) V V bond distances from the least-squares re nement (points) overlayed with a map of the V V distances obtained from RMC modeling. Reproduced from reference 136, c 2010 by the American Physical Society.

crease in the V atomic displacement parameters U_{ij}, which could convey information of the directionality of the displacement. Fig. 4.3(a) shows the least-squares refined values of the U_{ij} parameters of the tetragonal structure over the full temperature range. At all temperatures, $U_{11} \equiv U_{22}$ by symmetry. Above the transition, U_{33} is equal to U_{11}, while U_{12} (the only non-diagonal parameter allowed by symmetry) is negligible. The high-temperature V position is therefore spherical, and is shown on the right in Fig. 4.3(a). Below 340 K, dimerization along the c direction leads to a large increase in U_{33}. Tilting of V–V vectors off the c axis (zero above the transition) produces an increase in U_{12}. The corresponding growth and elongation of the V thermal ellipsoids are seen on the left in Fig. 4.3(a).

The split V positions and corresponding dimerized V–V distances are the hallmark of cooling through the transition, and we use the PDF to extract the distances directly. If there were a gradual shift in V–V distances over the extent of a wide transition region, which other probes such as the electrical resistivity suggest, the local structure information in the PDF would reproduce these distances regardless of whether or not they are correlated over long ranges. Least-squares refinements of the V–V distances (using the appropriate monoclinic or tetragonal model for each structure) are displayed as points in Fig. 4.3(b) and show an abrupt change upon cooling through the transition. The distances at 336 K and

342 K are effectively unchanged from the low- and high-temperature structures at 300 K and 400 K respectively, so the structural transition occurs within this range ($\Delta T < 6$ K). The least-squares refinements, however, are predicated on the choice of a monoclinic or tetragonal unit cell.

Histograms of V–V distances from RMC supercells (not constrained by symmetry) are displayed as an intensity map in Fig. 4.3(b). They display excellent agreement with the least-squares refined values for all points except $T = 340$ K, implying that the single-phase least-squares refinements accurately reproduce the true distribution of V–V distances in the end members. However, at $T = 340$ K the least-squares refined distances are of intermediate length, while the RMC V–V histogram is unclear. Is there an intermediate phase with V–V distances that are distinct from the monoclinic and tetragonal structures, or is there a mixture of two phases? Our subsequent analysis of the linear combination of experimental PDFs, along with V positions from RMC simulations, can resolve this issue.

In Fig. 4.4(a), experimental PDFs are displayed for $T = 334$ K, 340 K, and 342 K: below, during, and above the structural transition temperature. The $T = 334$ K and 342 K PDFs can be refined to the end member structures, so a linear combination of these two PDFs produces a two-phase PDF containing three V–V distances: two monoclinic and one tetragonal. This linear combination PDF is

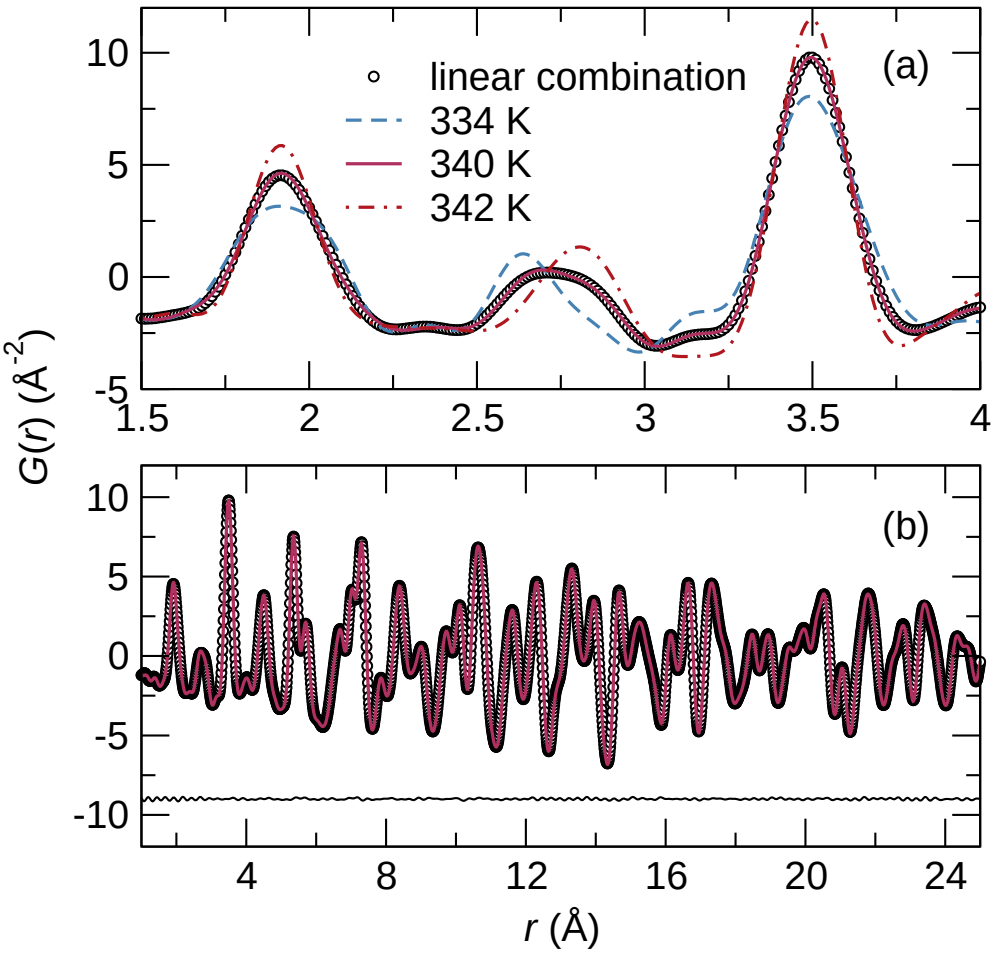

Figure 4.4: (a) Experimental X-ray PDFs from VO_2 at T below (334 K), equal to (340 K), and above (342 K) the transition temperature. A linear combination of the 334 K and 342 K data is shown as points, along with a difference curve to the 340 K data. In (b) the full fitting range is shown–at the transition temperature the sample is comprised of two distinct end-member phases. Reproduced from reference 136, © 2010 by the American Physical Society.

displayed as the points behind the $T = 340\,\mathrm{K}$ data, and tracks the data up to 25 Å. The difference curve between the combination PDF and the $T = 340\,\mathrm{K}$ data is shown in Fig. 4.4(b), showing that the two PDFs are identical within the limits of experimental noise. The agreement implies that, even on a local scale, the VO_2 sample at 340 K comprises two structurally distinct regions, corresponding directly to the tetragonal or the monoclinic structures. No additional contribution to the PDF is found.

Corroborating evidence for the two-phase combination is seen in RMC simulations. We examine the distribution of V positions around the ideal crystallographic site in real space by folding the positions of all V in the RMC supercell back into a single unit cell, which produces a cloud of 1600 V positions (from a $10 \times 10 \times 16$ supercell) on each site. This cloud is viewed as a two-dimensional histogram showing the most probable positions of V cations in the $a - c$ plane in Fig. 4.5. For each cloud with $T > 340\,\mathrm{K}$, V distributions are spherical (as seen in the ellipsoids in Fig. 4.3(a)) and centered on the ideal tetragonal positions. For $T < 340\,\mathrm{K}$, dramatic splitting of the V position is seen. These two spots correspond to the end member monoclinic positions. We see no evolution of V clouds versus temperature far from the transition, but the 340 K cloud possesses an intermediate shape, distinct from the two regimes on either side. Just as was performed for the experimental PDFs themselves, we can linearly

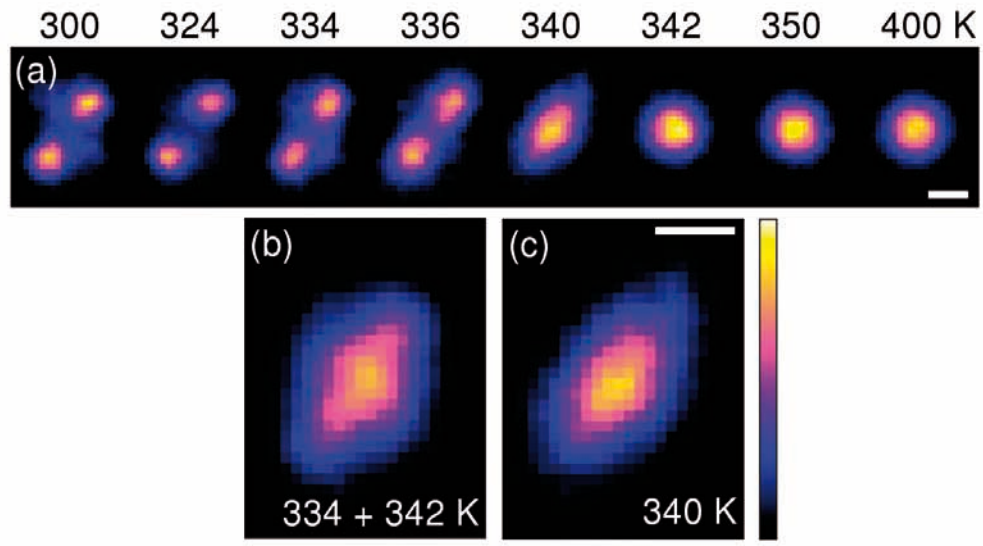

Figure 4.5: (a) The relative probabilities of V atom positions as obtained from RMC modeling are dimerized at four temperatures below and spherical at three temperatures above the transition. At T = 340 K, the probability distribution is intermediate. In (b), a two-phase model is formed by averaging the experimental maps from T= 334 K and 342 K, both of which resemble the low- and high-temperature end members. This resulting map appears similar similar to the 340 K data reproduced in (c). Scale bars are 0.2 A. The color bar indicates minimum and maximum probability. Reproduced from reference 136, c 2010 by the American Physical Society.

combine RMC results to produce models of a 1:1 mixture of the two phases. In Fig. 4.5(b), an average of the clouds from 334 K and 342 K is displayed, as a model of coexistence of the end members. The experimental cloud from T = 340 K is reproduced in Fig. 4.5(c), and their similar appearance indicates that this is a two-phase mixture, in agreement with the linear combinations of the PDF in Fig. 4.4.

4.4 Conclusions

Qazilbash *et al.*[145] have recently suggested the formation of "metallic nanopuddles" at the transition temperature, and Cava and coworkers[143] have suggested the importance of metal-metal dimers in a series of substituted $V_{1-x}M_xO_2$ (M = Nb, Mo) samples. What has not been clear up to now is whether these implied a third, intermediate phase of VO_2. Here, we have shown that at the transition temperature there are only two distinct phase populations: low temperature monoclinic VO_2 together with the high temperature tetragonal phase. Above the transition, there is no evidence for the presence of V–V dimers.

Chapter 5

Static atomic displacements in the charge ice pyrochlore $Bi_2Ti_2O_6O'$

5.1 Introduction

Magnetic oxides with the $A_2B_2O_7$ pyrochlore structure have been the subject of intense study. The lattice of corner-connected tetrahedra of A atoms hinders cooperative magnetic ordering, and when the A atom spins are Ising, an ice-like ground state is produced, for example in $Dy_2Ti_2O_7$ and $Ho_2Ti_2O_7$.[161–164] Other recent developments in oxide pyrochlores include superconductivity in

[1]Portions of this chapter have been published in reference 103 © 2010 by the American Physical Society

osmium compounds,[165] the formation of polar metallic states with unusual phonon modes,[166], and the suggestion of chiral magnetic ground states.[167] The analogy between Ising spins and vector displacements of cations within their coordination polyhedra has led to the suggestion that polar ordering may be similarly frustrated on the pyrochlore lattice.[168] Thus in pyrochlore $Bi_2Ti_2O_6O'$, it is known that the Bi^{3+} atoms, usually predisposed to off-centering within their coordination polyhedra, display incoherent displacements permitting the average structure to remain cubic.[169] This is in sharp contrast to the Bi^{3+}-containing perovskites $BiMnO_3$ and $BiFeO_3$ where the lone-pair active A-site produces polar, non-cubic ground states.[170] Some signatures of these incoherent displacements are seen in measurements of heat capacity of $Bi_2Ti_2O_6O'$ and related compounds at low temperatures.[171]

Significant advances in describing frustrated, ice-like behavior in magnetic pyrochlores have been made when atomistic models are utilized to describe the interactions between individual A sites. For example, atomistic simulation of magnetic spin ordering in $Dy_2Ti_2O_7$ leads to a picture of localized, uncompensated spins connected by strings of ordered spins.[163, 164] This picture is local: spin behavior is driven by connectivity, geometry, and pairwise exchange interactions. However, it also agrees with bulk thermodynamic measurements: the heat capacity of the ensemble average agrees with experimental observa-

tions. This chapter demonstrates how experimental modeling over multiple length scales, both atomistic and averaged, affords a view of the pyrochlore $Bi_2Ti_2O_6O'$ where Bi *displacements*, rather than spins, form a frustrated network on the A sublattice. These frustrated displacements produce diffuse scattering, just as incoherent spin orientations produce diffuse magnetic scattering.

$Bi_2Ti_2O_6O'$ [structure in Fig. 5.1(a)] is written thus to emphasize the two sublattices: one of corner-sharing TiO_6 octahedra, and the other of corner-sharing $O'Bi_4$ tetrahedra. While the TiO_6 sublattice is rigid in models of the average structure, Bi atoms are suggested to displace 0.4 Å normal to the linear O′–Bi–O′ bond in an uncorrelated manner.[168, 169] First-principles calculations on $Bi_2Ti_2O_6O'$ predict Bi displacements but these are perforce associated with non-cubic symmetries.[172] Diffuse intensity in electron diffraction patterns of related compounds including $Bi_2Ru_2O_7$, Bi_2InNbO_7, and Bi_2ScNbO_7 may indicate short-range correlations in the Bi displacements.[22, 173, 174] If Bi displacements cooperatively order with each other, they must do so only over short ranges. Crystallographic analysis based on Bragg scattering leaves a void in the ability to probe such short-range order, as analyses are predicated on the existence of long-range order. Consequently, studies of displacive disorder on the A site *via* Rietveld refinement or Fourier maps can produce a model of the *average* electron or nuclear distributions, but each A site has an identical cloud of

intensity.[175]

We use reverse Monte Carlo (RMC) fits to the pair distribution function (PDF) and Bragg profile to produce models where the correlated motion of atoms on the A sites reproduces the atomistic, pairwise distances between individual atoms. Many of these models are combined and used as a set of atomic positions for further analysis. RMC compares the experimental and computed (based on atom positions in the simulation box) $D(r)$ and $S(Q)$ while randomly relaxing atomic positions. The method is similar to Metropolis Monte Carlo, except that the fit to data χ^2, instead of a potential energy function, is minimized.[7, 55, 176]

There are many approaches to describing the behavior and correlations of atomic positions as obtained from large-box models of structure. Some examples include the use of quadrupolar moments of octahedra to describe $LaMnO_3$,[80] of contour plots of bond angles in cristobalite,[135] and the use of bond valence analysis to obtain valence states from a statistical analysis of metal-oxygen positions as in $CuMn_2O_4$ and $Mg_{1-x}Cu_xCr_2O_4$.[59, 177] Here we analyze the local geometry using simple metrics, then present the continuous symmetry measures (CSM)[73, 100, 101] of polyhedra from RMC simulations. The CSM model provides a quantitative measure of a polyhedron's distortion, in the form of a "distance" from ideality. A key advantage of CSM is its ability to compare

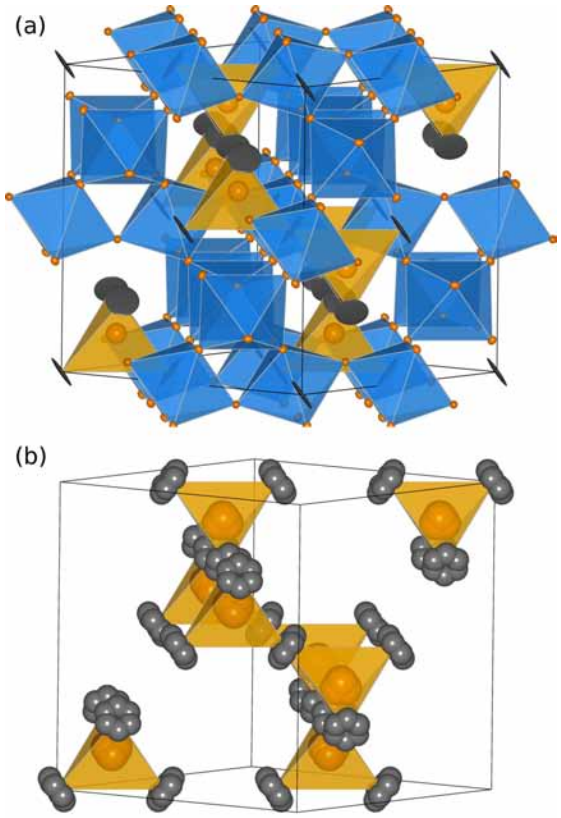

Figure 5.1: The $Bi_2Ti_2O_6O'$ crystal structure in (a) has 50% thermal ellipsoids representing the atomic displacement parameters from Rietveld refinement at 14 K. The two sublattices are corner-sharing TiO_6 octahedra (blue) and corner-sharing $O'Bi_4$ tetrahedra (orange). Bi and O′ are on ideal positions. Bi cations (black) appear as discs due to their displacement normal to the O′–Bi–O′ bond. This disorder can be modeled using six-fold-split Bi and four-fold-split O′ as in (b). Reproduced from reference 103, © 2010 by the American Physical Society.

shapes in different compounds.[101] The CSM has been used to correlate deviations from ideal tetrahedra in silicates as a function of applied pressure,[178] and to analyze second-order Jahn-Teller systems across a variety of crystal structures.[102] In these cases, the CSM was considered for the average crystallographic stucture, *e.g.* one where polyhedra possess a single CSM value. Here, as in $Mg_{1-x}Cu_xCr_2O_4$, CSM is applied to large-box modeling by calculating it for every $O'Bi_4$ tetrahedron in the RMC supercell, obtaining distributions, rather than single values.

The key finding to emerge from this study is that displacements from ideal atomic positions in $Bi_2Ti_2O_6O'$ and in particular, the nature of the $O'Bi_4$ tetrahedra indicate a tendency for Bi to lie in a disordered ring around the ideal position, with some preference for near-neighbor Bi-Bi ordering. This reaffirms the case that, even when probed microscopically, $Bi_2Ti_2O_6O'$ is ice-like in its disorder. In drawing the analogy with ice, we do not suggest the existence of ice-rules of the Bernal-Fowler[179] type in these systems.

5.2 Methods

Synthesis and a detailed average structural analysis of the sample used in this study (including verification of purity) has been reported by Hector and

Wiggin.[169] Briefly, a basic solution of titanium metal with hydrogen peroxide and ammonia was added to an acidic solution of bismuth nitrate pentahydrate and nitric acid. The resulting precipitate was filtered, washed with a dilute ammonia solution, dried at 50°C, and calcined in air for 16 h at 470°C. Time-of-flight (TOF) neutron powder diffraction on samples held in vanadium cans was collected at the NPDF instrument at Los Alamos National Laboratory at 298 K and 14 K. NPDF is designed to collect high-resolution, high-momentum-transfer data suitable for production of the PDF, as well as traditional Rietveld refinement. We performed Rietveld refinement using GSAS.[53]. Extraction of the PDF with PDFGETN [8] used $Q_{max} = 35\,\text{Å}^{-1}$, and least-squares refinements of the PDF were performed with PDFGUI.[10]

First-principles density functional methods were used to identify a possible ordered ground state. The local stability of $Fd\bar{3}m$ $Bi_2Ti_2O_7$ was investigated using projector augmented wave potentials within the local density approximation as implemented in the VASP program[180–183] and described previously.[172] Three zone-center lattice instabilities were found–one ferroelectric and two antiferroelectric-like modes–which were used to guide a systematic search for low-symmetry phases. A series of structural relaxations within each of the highest-symmetry isotropy subgroups[184, 185] consistent with the freezing-in of one or more of these lattice instabilities revealed that the lowest energy

structure is ferroelectric (with a substantial polarization of $\mathbf{P} \approx 20\,\mu\mathrm{C\,cm^{-2}}$), in the polar monoclinic space group Cm, consistent with the freezing-in of all three modes.

Maximum entropy method (MEM) calculations of the nuclear scattering density were performed using PRIMA.[186] RMC simulations were performed using RMCPROFILE [18] version 6 on a $5 \times 5 \times 5$ supercell (cubic, ≈ 52 Å per side) with 11000 atoms. These simulations were constrained by the PDF (in the form of $D(r)$)[20] up to $r = 12$ Å and by the Bragg profile of NPDF bank 1, which contains the lowest-Q Bragg reflections. Crystal structures are visualized using VESTA [58] and ATOMEYE. [57] Quantitative analyses shown in this work are taken from averaging many simulations in order to obtain an unbiased interpretation of the fit to data. Hard-sphere cutoffs were employed in RMC simulations to ensure that atoms did not approach closer than the specified nearest-neighbor distances, but no bunching was observed at these cutoffs. CSM for O′Bi_4 tetrahedra were calculated using a distance measure program provided by M. Pinsky and D. Avnir.

5.3 Results and discussion

5.3.1 Average structure from Rietveld refinement

The profile resulting from TOF neutron Rietveld refinement is displayed (for a single bank of data) in Fig. 5.2. The goodness of fit parameter $R_{wp} = 2.9\%$. The sample is the same as used in the Rietveld study of Hector and Wiggin,[169] and the fit converges to similar structural parameters (within error), so these will not be reproduced here.

In $Bi_2Ti_2O_6O'$, preliminary Rietveld refinement using an ideal pyrochlore model can obtain a good fit to data, but large atomic displacement parameters (ADPs) indicate that significant atomic disorder is present, characterized by an elliptical spread around the ideal atomic positions. The ideal Bi position on the $16c$ (0,0,0) site can be fit using a large U_{23} component. These appear as large, flat discs in Fig. 5.1(a) with a radius of about 0.4 Å. The discs envelop the Bi displacive disorder which we seek to accurately describe. The O′ atoms at the $8a$ $(\frac{1}{8}, \frac{1}{8}, \frac{1}{8})$ position have large, isotropic displacements as well, corresponding to $U_{iso} \approx 0.4$Å^2. The TiO_6 sublattice, on the other hand, is described by small U_{iso} values and does not display any signs of displacive disorder. Here we investigate the precise nature of atomic displacements in the O′Bi_4 sublattice.

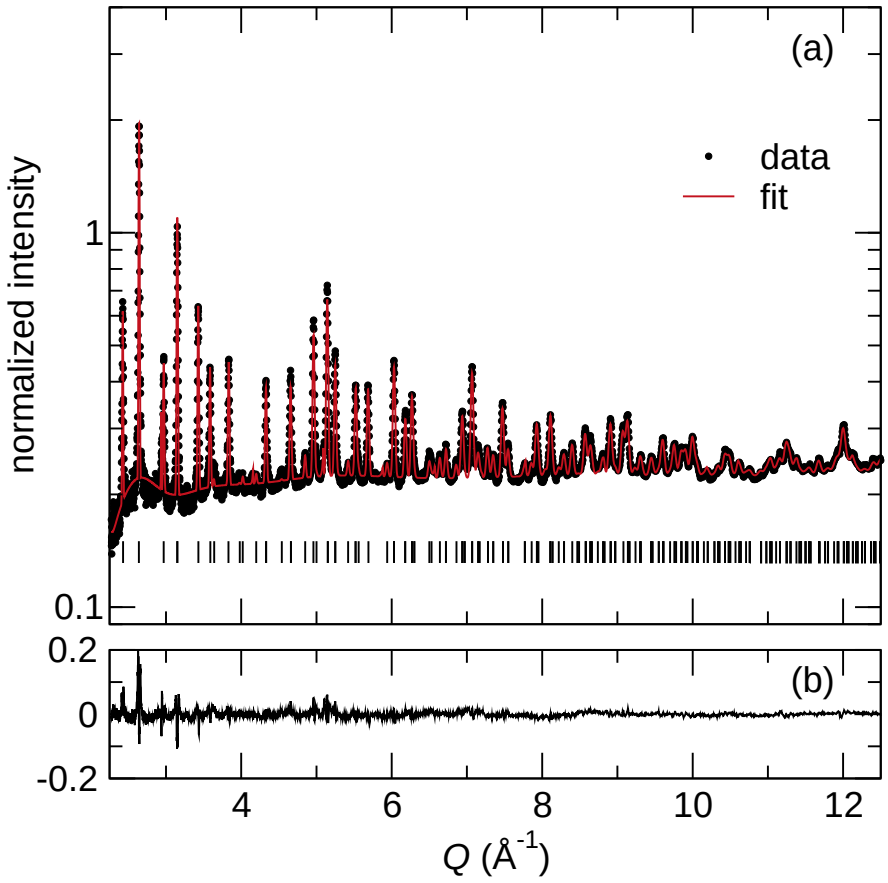

Figure 5.2: Neutron TOF Rietveld refinement of $Bi_2Ti_2O_6O'$ at 14 K (a) using the model of Hector and Wiggin [169] gives a fit with $R_{wp} = 2.9\%$. Small features in the difference curve (b) at low Q are caused by shoulders of diffuse intensity around Bragg peaks. This component of the data can be interpreted using total scattering analysis. Reproduced from reference 103, © 2010 by the American Physical Society.

Improved refinement of the average pyrochlore structure has been achieved by using a split-atom model for the A sites, such as in studies of $Bi_2Ti_2O_6O'$,[169, 187] $Bi_2Sn_2O_7$,[188] or $La_2Zr_2O_7$.[175] Hector and Wiggin modeled Bi using a six-fold ring in the $96g$ position,[169] but acknowledged that their refinement does not clearly show a preference for $96g$ versus $96h$ (rotated 30° to each other). The $96g$ split-atom configuration is shown in Fig. 5.1(b). Comparison to an ideal-position model in Fig. 5.1(a) shows that the Bi split-atom sites lie inside the anisotropic discs. Most O′ intensity is still centered on the $8a$ site, but some occupancy is shifted away in 4 directions to form a tetrapod, modeled by partial occupancy of the $32e$ sites. From Rietveld refinement, the Bi displacement parameters at 14 K and 300 K are similar in orientation and magnitude. This suggests that Bi displacements are frozen at room (and higher) temperatures, and what is being monitored in the scattering is not a snapshot of dynamic motion, but rather a description of static positions. The suggestion of frozen displacements at room temperature is consistent with measurements of the temperature- and field-dependence of the dielectric constant in $Bi_2Ti_2O_6O'$ thin films.[189]

Kinks in the difference profiles of the Rietveld refinement in Fig. 5.2(b) can be attributed to shoulders of diffuse intensity around low-Q peaks. The diffuse scattering cannot be interpreted here because the Rietveld technique only mod-

els Bragg intensity. Crucial approximations are made to model a structure using only Bragg peaks: any atomic correlations or distortions that do not possess long-range ordering must be averaged. The Bi distortions are incoherent, and their description will require an examination of diffuse scattering. Total scattering analysis of the real-space PDF, discussed here subsequently, provides a real-space tool to model both Bragg and diffuse scattering simultaneously.

5.3.2 Maximum entropy method

The maximum entropy method (MEM) was used here to produce a map of neutron scattering density in the unit cell. The method, proposed originally by Jaynes,[190, 191] uses some testable information (in this case, observed Bragg peak intensities in TOF neutron diffraction), and is based on the most probable distribution (nuclear scattering density) being the one with the largest information entropy. This method is described by Sakata[192, 193] and in the context of the MEM software program MEED,[194] a precursor to the software code PRIMA used here. The MEM input consists of the observed Bragg structure factor F_{obs} (from a Le Bail fit, with phase information from the ideal structure) for a list of hkl reflections, the unit cell dimensions, space group, and the sum of all scattering lengths in the cell. The MEM as employed here is largely model-free

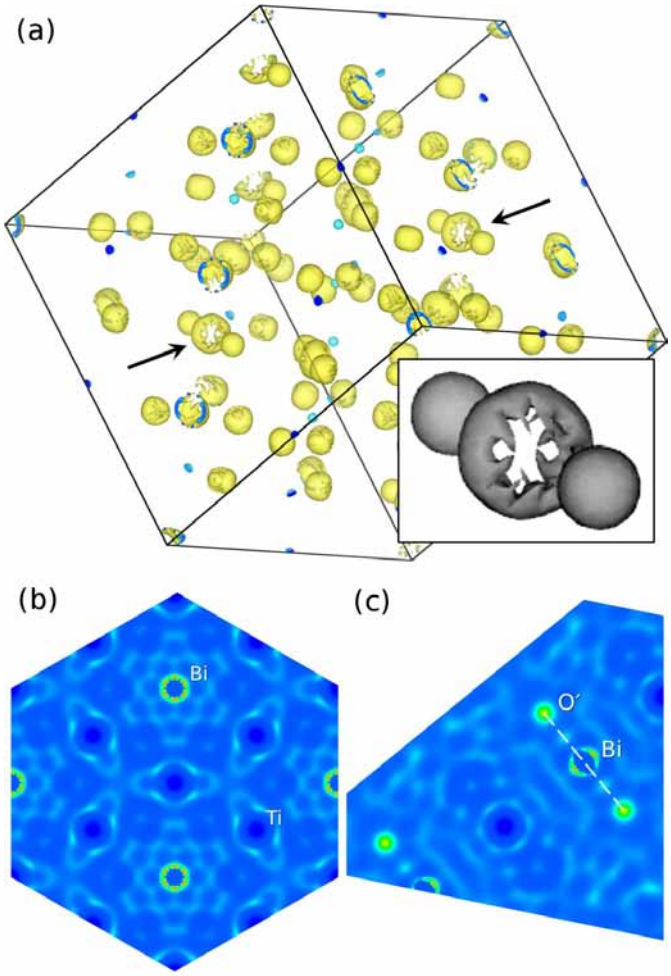

Figure 5.3: The MEM nuclear density map of the $Bi_2Ti_2O_6O'$ unit cell at 14 K is plotted in (a). Arrows point to Bi positions where the rings are rotated with the O′–Bi–O′ direction almost parallel to the viewing direction. The circular Bi isosurface is magnified in the inset. The 2-D density slice in (b) is the $(11\bar{1})$ plane, normal to O′–Bi–O′ bonds, and (c) is the $(12\bar{1})$ plane with the O′–Bi–O′ bond dashed. The imposed sixfold symmetry of the Bi ring is evident in the $(11\bar{1})$ slice. Reproduced from reference 103, © 2010 by the American Physical Society.

in the sense that atomic positions are not specified during the calculation, but phase information for F_{obs} is biased by the ideal structure. The final result is required to obey the symmetry of the space group. This is also an average structure probe–diffuse scattering intensity is ignored. Thus all Bi atomic positions in $Bi_2Ti_2O_6O'$, for example, will be equivalent to each other as required by $Fd\bar{3}m$.

Despite these constraints, the MEM affords an excellent view of average Bi displacements. No prior description of Bi displacements, or even a knowledge of their existence, is used to produce them in the isosurface neutron density unit cell displayed in Fig. 5.3(a). Arrows point to the circular Bi density that forms a ring around the O′–Bi–O′ bond. Two-dimensional slices of the cell viewed along and normal to the O′–Bi–O′ bond in Figs. 5.3(b) and 5.3(c), respectively, show additional detail of the Bi nuclear density. The Bi ring appears hexagonal in Fig. 5.3(b), which is the required symmetry of the position in $Fd\bar{3}m$. The strongest intensity of Bi points toward the in-plane Ti in Fig. 5.3(b). This corresponds to a $96h$ site for Bi, not $96g$.[195] While the Bi shapes found by MEM agree with those from Rietveld refinements, there is no evidence of a tetrapod-shaped spread in the O′ density in MEM. This shape would be allowed by symmetry.

5.3.3 Least-squares PDF refinement

When displacements of atomic positions and their correlations have been proposed in the pyrochlore structure, it has been compared to the SiO_4 tetrahedral network of β-cristobalite, which is isostructural to the O′Bi_4 sublattice.[22, 196, 197] This configuration would have long-range zig-zag ordering of Bi displacements shown in Fig. 5.5. These distortions may be ordered along any of the three Bi–Bi directions in the lattice, and the distortions in one direction need not be correlated with those in another.[135, 198] We use least-squares PDF refinement (a small-box technique) to compare the observed local structure to two models: the $Fd\bar{3}m$ Rietveld-derived average model with large ADPs, and the Cm ordered structure from first-principles calculations.

The average model fit to the experimental PDF is shown in Fig. 5.4(a). The large, disc-shaped ADPs on the Bi positions cause the peak at 2.2 Å to flatten and disappear, and the fit does not significantly improve as r increases. The short-range fit up to $r = 3.4$ Å and the medium-range fit from $3.4 \leq r \leq 6$ Å both give high χ^2 values. The polar, ordered model fit in Fig. 5.4(b) describes the low-r region very well. Here, a single Bi–O′ distance is well-defined, so the peak at 2.2 Å appears. The medium-range fit is poorer than the short-range fit, but still much better than the average model. Rietveld, MEM, and least-squares

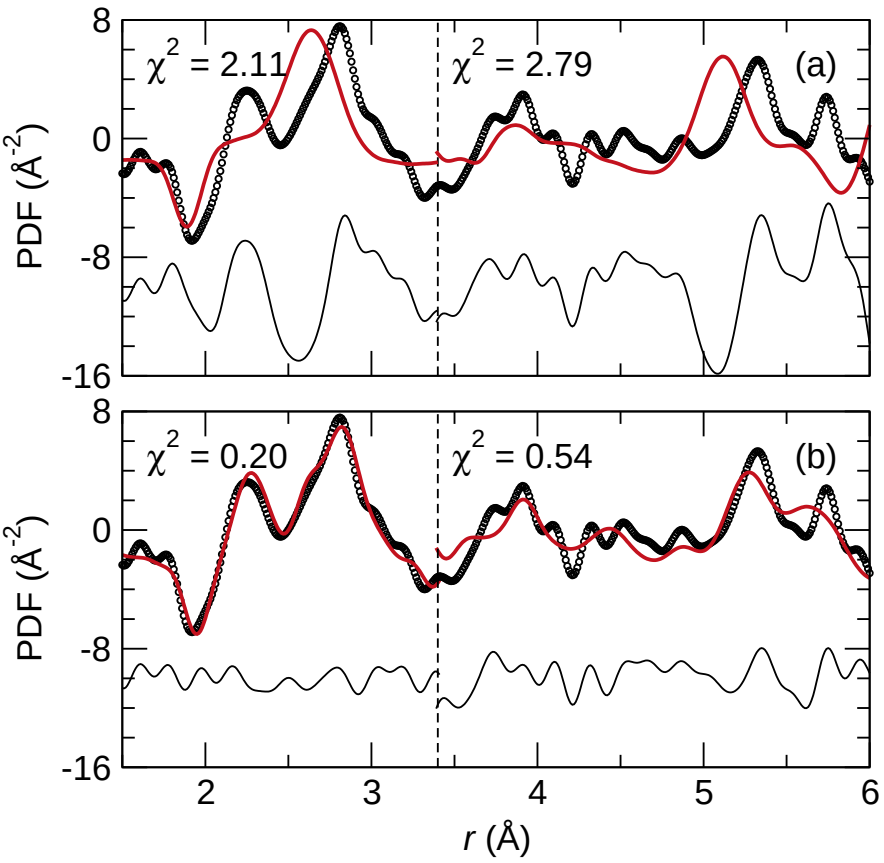

Figure 5.4: Least-squares refinements of the $Bi_2Ti_2O_6O'$ PDF at 14 K. Panel (a) shows the fit to an ideal average structure (Bi centered on $16c$ sites with disc-shaped thermal parameters) as shown in Fig. 5.1(a). Panel (b) is the Cm structure from first-principles . The χ^2 is shown for two fits per model: a fit up to 3.4 Å and a fit from 3.4 Å to 6 Å. Difference curves are shown below. Reproduced from reference 103, © 2010 by the American Physical Society.

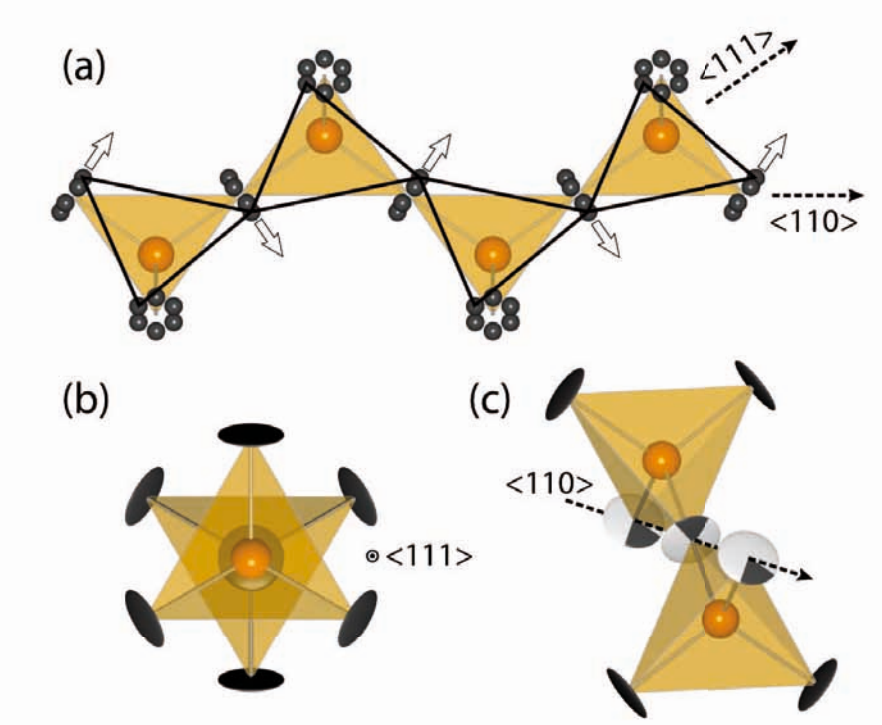

Figure 5.5: (Color online) In (a), the ideal O Bi_4 sublattice (orange tetrahedra) with split-atom Bi positions (black) can cooperatively order in a zig-zag (arrowed), χ-cristobalite-like pattern ordering seen as solid black lines. We use a double-tetrahedral model viewed along the O O direction in (b) to investigate local correlations. This shape is viewed in (c) near the Bi Bi direction with the most-probable wedges of the circular Bi ADPs shown schematically for zig-zag ordering.

PDF analyses show that the structure of $Bi_2Ti_2O_6O'$ shares some attributes of the average structure (lattice parameters, averaged positions) and the local Cm model (bond distances and angles at low r). Analysis by least-squares refinement of the PDF is limited because one must construct a model that resembles both $Fd\bar{3}m$ and Cm. The complex disorder present in $Bi_2Ti_2O_6O'$ makes it an excellent candidate for reverse Monte Carlo simulations.

5.3.4 Reverse Monte Carlo simulations

RMC simulations utilize large-box modeling with periodic boundary conditions and are not constrained by symmetry.[18, 176, 199] This provides two principal advantages when simulating crystalline materials: the ability to model nuclear positions with arbitrary shapes, and the ability to investigate correlations between atoms on the Å length-scale. We profit from both when modeling $Bi_2Ti_2O_6O'$. First, the true shapes of Bi and O′ displacements must be elucidated. Second, Bi–Bi nearest-neighbor correlations may lead to cooperative distortions of the $O'Bi_4$ sublattice. This type of short-range order would be a signature of local regions where the lone-pair-active Bi displacements effect polar domains.

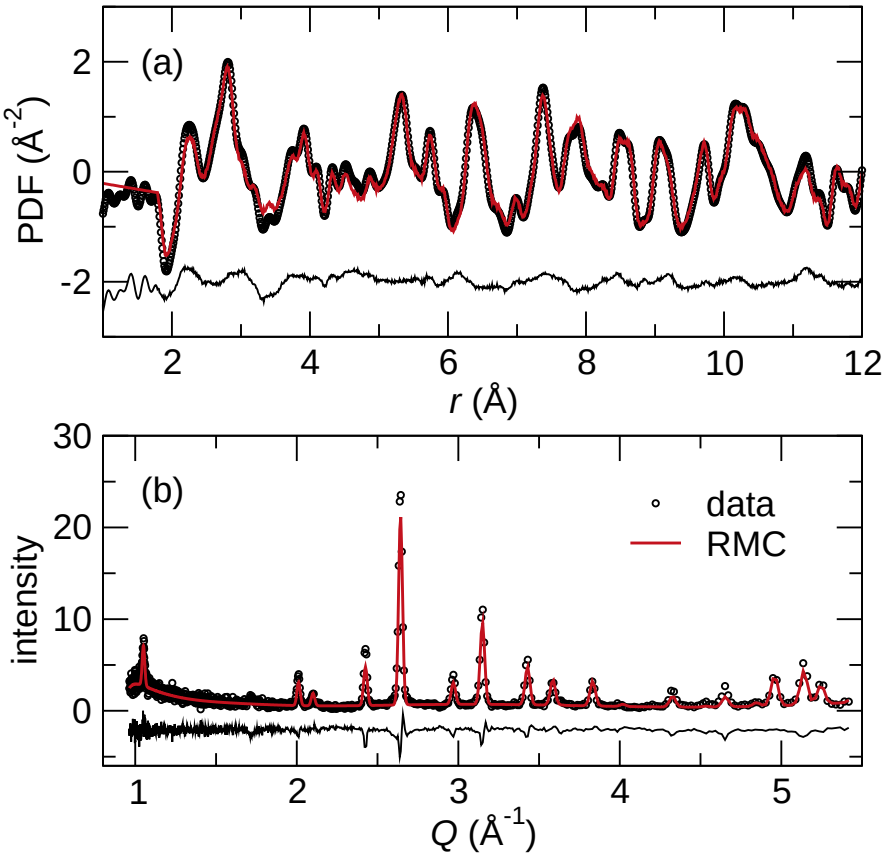

Figure 5.6: RMC fits to 14 K $Bi_2Ti_2O_6O'$ experimental data shown for (a) the PDF $G(r)$ and (b) the Bragg profile. The RMC simulations employ supercells ($5 \times 5 \times 5$, ≈ 52 Å per side) that fit both data sets simultaneously. Reproduced from reference 103, © 2010 by the American Physical Society.

Average atomic displacements

The real-space local structure (coordination environments, short-range correlations, *etc*.) of the RMC supercell is driven by the fit to the PDF, while the Bragg fit constrains the long-range periodicity of the structure (or lack thereof) and ensures reliable displacement parameters. In the case of $Bi_2Ti_2O_6O'$, the agreement of Rietveld and RMC ADPs (calculated as the mean-square displacement from ideal positions) was monitored as a merit of agreement with the long-range structure. RMC simulations were started with the ideal pyrochlore lattice with all Bi atoms on $16c$ positions. As the simulation progresses, Bi atoms are always observed to move off the central position to form a ring that resembles the Rietveld split-atom model. The fits to the 14 K PDF and Bragg profile are shown in Fig. 5.6(a,b).

A comparison of the ideal unit cell with a folded RMC supercell is shown in Fig. 5.7. In Fig. 5.7(b) the 125 unit cells of a supercell are folded into a single unit cell. The result is a cell with "point clouds" on each atomic position that represent a map of the nuclear scattering density on each site in $Bi_2Ti_2O_6O'$. Of particular note is the large spread of Bi and O′ point clouds in Fig. 5.7(b) in comparison to those of Ti and O. These distributions agree quantitatively with the ADPs from Rietveld refinement.

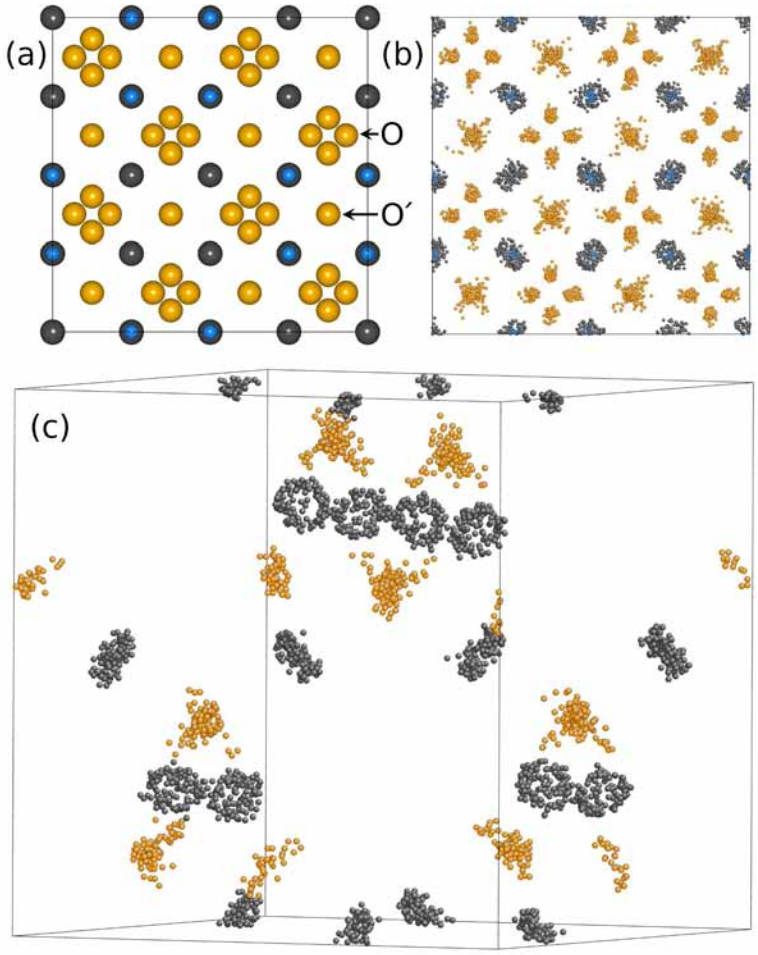

Figure 5.7: The ideal, isotropic $Bi_2Ti_2O_6O'$ unit cell is plotted in (a) along the a direction, with Bi atoms in black, Ti blue, and O orange. This unit cell can be visually compared with the folded 14 K RMC supercell in (b). Positional disorder is much greater in Bi and O′ (which appear X-shaped in this projection) than in Ti and O (appear as clusters of four O). In (c), the $O'Bi_4$ sublattice is plotted near $\langle 110 \rangle$ to show the Bi rings. Reproduced from reference 103, © 2010 by the American Physical Society.

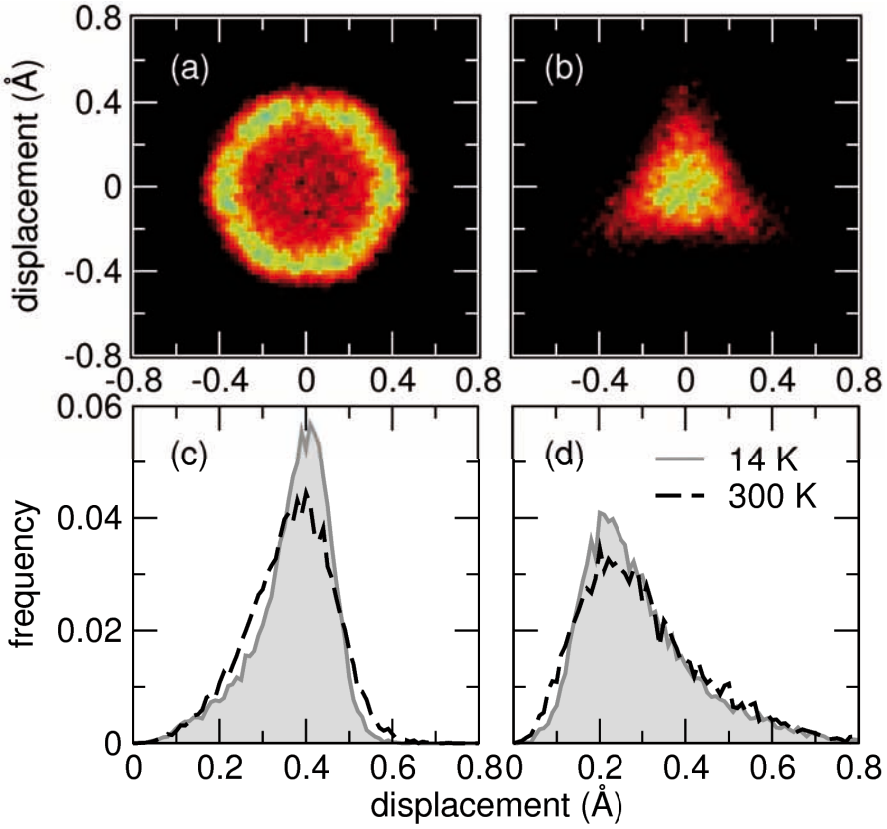

Figure 5.8: Atomic positions for (a) Bi and (b) O at 14 K from 14 independent RMC simulations are plotted in the 111 plane normal to the O Bi O bond. Histograms of displacement distances are plotted for 14 K and 300 K simulations in (c) and (d), with the 14 K histograms shaded for clarity. The Bi median displacement of 0.4 A agrees with the Bi Rietveld ADP. Reproduced from reference 103, c 2010 by the American Physical Society.

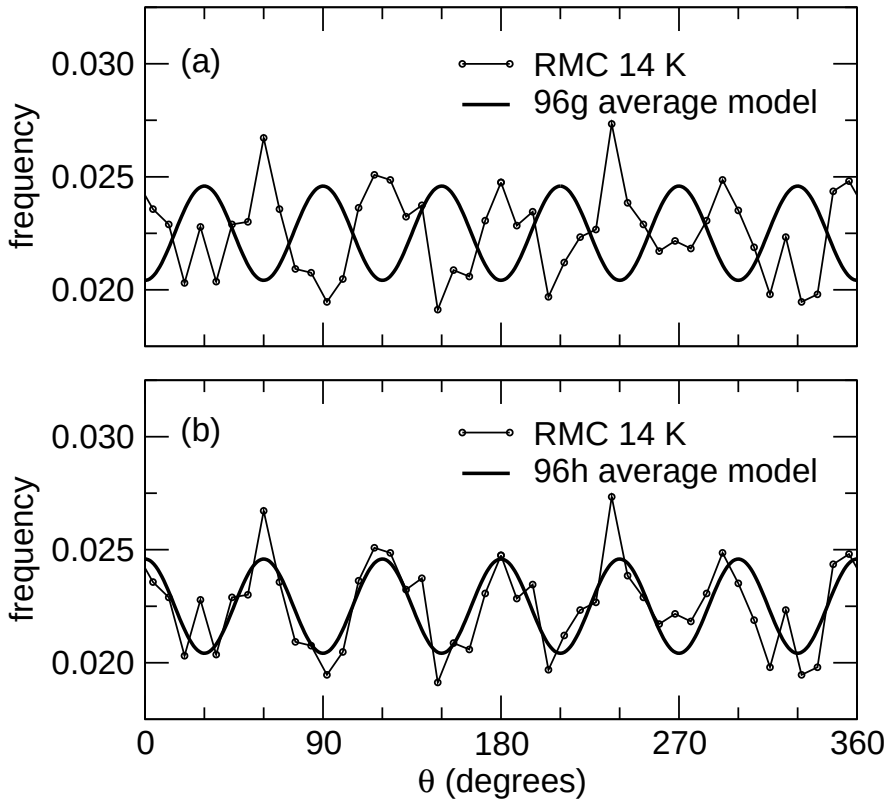

Figure 5.9: Histogram of the average Bi displacement angle θ around the O′–Bi–O′ bond at 14 K. Solid lines show the expected six-fold cosine curves that indicate preference for (a) $96g$ or (b) $96h$ hexagonal ring symmetry. Reproduced from reference 103, © 2010 by the American Physical Society.

The O′Bi_4 sublattice from a 14 K RMC simulation is shown in Fig. 5.7(c), viewed close to the $\langle 110 \rangle$ direction. From this viewpoint, Bi rings are evident. These rings open normal to the O′–Bi–O′ bonds, as expected from Rietveld ADPs and MEM. The average shape of a Bi ring is seen in Fig. 5.8(a). Viewed along the O′–Bi–O′ direction, it appears circular with a radius of about 0.4 Å. A histogram of Bi distances from the ideal $16c$ site is given in Fig. 5.8(c), with a clear maximum at the ring radius. The same procedure applied to O′ yields a tetrapodal object. Seen in Fig. 5.8(b), the arms of this tetrapod point away from the four neighboring Bi atoms. One arm of the tetrapod is in the center of the plot, pointing normal to the page. A key distinction between O′ and Bi is that the dense cluster of O′ positions is still centered on the ideal $8a$ position, seen as a bright cluster in the center of Fig. 5.8(b). In contrast, Bi intensity is low at the center and most intensity lies on the ring perimeter. The displacement histograms in Figs. 5.8(c,d) reveal similar shapes in RMC simulations of 14 K and 300 K data, with a slight broadening at high temperature. This supports the idea that these displacements are frozen at high temperatures and do not fundamentally change with cooling.

The RMC model corroborates with Rietveld and MEM while providing further evidence for a tendency toward a sixfold Bi ring. In Fig. 5.9(a), a histogram of the the rotation angle θ of Bi around the $\langle 111 \rangle$ axis is fit to a sixfold cosine

curve. This curve, with a minimum at $\theta = 0°$, corresponds to the $96g$ sites and does not fit the data. Instead, Fig. 5.9(b) shows excellent agreement between the RMC result and the $96h$ six-fold curve, which is shifted by 30° from $96g$. Note however that the intensity at minima in the curves is not zero; there is still some tendency for Bi to lie at any θ. It is not known whether increased preference for the $96h$ site would push the minima to be nearly zero. It is possible that stronger ordering exists, but is obscured by the resolution of the data.

Correlated distortions: double-tetrahedral model

Cooperative β-cristobalite correlations can be visualized in the polyhedral configurations given in Fig. 5.5. The motif of two corner-linked O′Bi_4 tetrahedra is the basis of this analysis. The zig-zag pattern is comprised of Bi that are all in the same plane (denoted with arrows). This plane is defined by the displacement of any Bi atom in the chain, so the central Bi atom can only participate in zig-zag ordering in one direction at a time. The two inline nearest neighbors of the central atom should have a tendency to displace opposite from the central Bi displacement vector. The correlation can be quantified by examining the angle ϕ between the displacement vector of the central Bi versus the displacement vectors of the two relevant nearest neighbors. Each double-tetrahedral shape in the supercell is examined in this manner. A schematic showing selected orientations

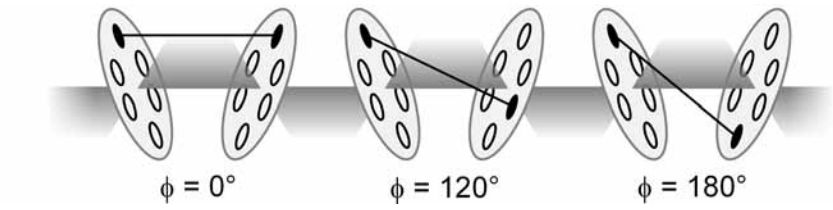

Figure 5.10: Schematic of possible values of ϕ, probing nearest-neighbor correlations of Bi displacements (not to scale). Reproduced from reference 103, © 2010 by the American Physical Society.

of neighboring Bi displacements and their corresponding values of ϕ is given in Fig. 5.10.

In Fig. 5.11(a), the relative angle ϕ histogram is plotted for the RMC simulations. It does not have the same six-fold modulation as the averaged Bi angles θ in Fig. 5.9(b) because ϕ is defined relative to its *neighbors*, while θ is defined relative to the *crystal axes*. We investigate the tendency for ordering by shuffling Bi displacements: the set of all individual Bi displacements from their ideal sites is preserved, but redistributed randomly among the Bi atoms. As a result, their orientations with respect to each other are disrupted. Note that, as a result of the removal of this local correlation, the shuffled ϕ curve is simply a six-fold cosine curve with modulation analogous to θ in Fig. 5.9(b). The difference between the RMC and shuffled ϕ, plotted in Fig. 5.11(b), shows a peak at $\phi = 180°$, indicating a preference for zig-zag ordering. Correlations where $60° < \phi < 120°$ are

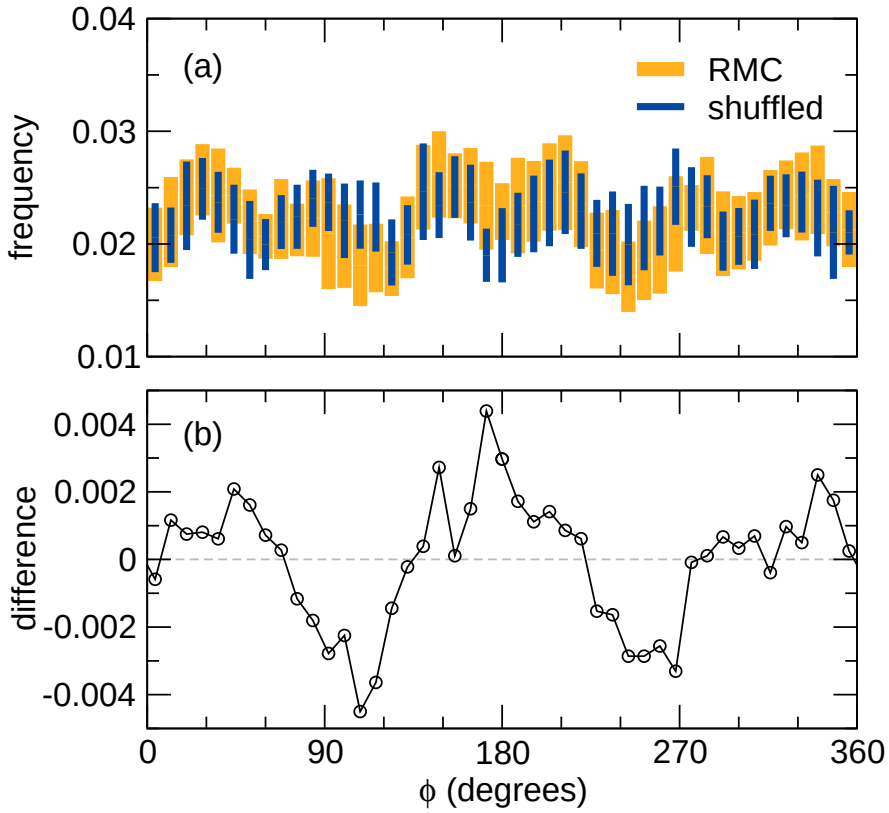

Figure 5.11: Histograms (a) of the Bi-Bi angle ϕ for neighboring displacements, with error bars of $\pm\sigma$. The difference between the RMC result and the same configurations with randomly shuffled Bi displacements is shown in (b). The difference curve peaks at $\phi = 180°$, indicating some zig-zag-like correlation. Angles around $\phi = 120°$ seem unfavorable. Reproduced from reference 103, © 2010 by the American Physical Society.

not preferred. While these results point to anti-alignment of Bi displacements, $Bi_2Ti_2O_6O'$ should not be considered to follow the β-cristobalite model strictly, since Bi would need to prefer the $96g$ site rather than $96h$.

Correlated distortions: continuous symmetry measures

The CSM provides a quantitative measure of a polyhedron's distortion, in the form of a "distance" from ideality.[73, 100, 101] A perfect tetrahedron would have tetrahedricity $S(T_d) = 0$, while distortions from ideality increase this value toward 1. As a point of reference, the Jahn-Teller distorted CuO_4 tetrahedron in $CuMn_2O_4$[59] has $S(T_d) = 0.0235$ while a square plane has $S(T_d) = \frac{1}{3}$.

Application of CSM to the $O'Bi_4$ sublattice is useful because $S(T_d)$ describes the correlations between four neighboring Bi atoms. Comparison between models and RMC simulations are shown in Fig. 5.12. For a model with ordered β-cristobalite-type ordering with a similar displacement magnitude, $S(T_d) = 0.008$. This is plotted as a vertical line in Fig. 5.12(b). In contrast, uncorrelated and evenly circular (with radius 0.4 Å) Bi displacements produce a wide distribution of $S(T_d)$, shown as a dotted line in Fig. 5.12(a), and again as a cumulative fraction in Fig. 5.12(b).

In a case where zig-zag (or otherwise correlated) distortions are present

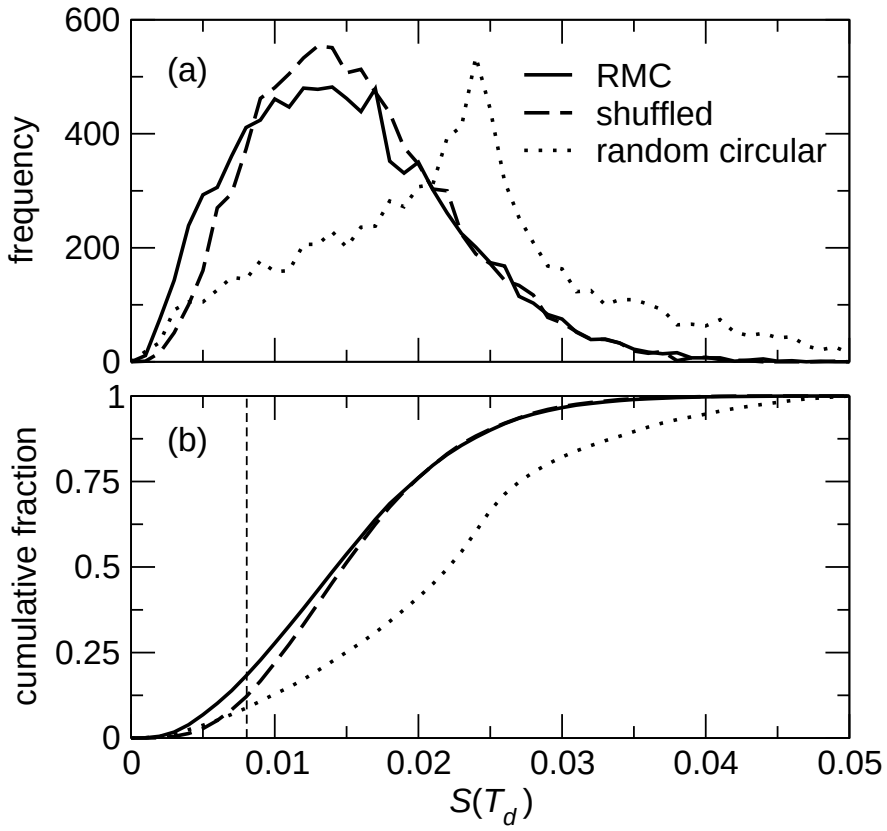

Figure 5.12: Histogram (a) of the CSM tetrahedricity $S(T_d)$ for three supercells: the RMC supercell, the same RMC supercell with Bi displacements randomly swapped, and a model with random circular Bi rings of equal radius. The peak at higher $S(T_d)$ in the circular model indicates more deviation from ideality than in the RMC supercells. These histograms are plotted as cumulative probability functions in (b), where the agreement between the RMC and swapped supercells suggest little evidence for cooperative short-range Bi ordering within tetrahedra. A fully-ordered model is denoted by a vertical line at $S(T_d) = 0.008$. Reproduced from reference 103, © 2010 by the American Physical Society.

on most O′Bi_4 tetrahedra in the supercell, Bi displacements should be correlated with their nearest neighbors, and a polyhedral rigidity reminiscent of SiO_4 tetrahedra might exist. If these displacements from ideal positions were randomly swapped among Bi atoms, the ordering would be destroyed and $S(T_d)$ would increase toward the random circular model. In a case where there is no short-range Bi–Bi ordering, randomly swapping the displacements should have no effect on the $S(T_d)$ distribution.

In Fig. 5.12 we compare the $S(T_d)$ distributions for the RMC supercell and the same supercell with Bi displacements randomly swapped. The distributions are shown as histograms of $S(T_d)$ in (a) and cumulative fractions in (b). The random swapping slightly increases $S(T_d)$ for the RMC supercell, seen as a shift to the right in Fig. 5.12(b). This curve is still quite separated from the random circular model.

Two aspects of the Bi distribution can be gleaned from this comparison. First, the Bi displacements of the RMC supercell are more strongly tetrahedral than the random circular model. This could be due to rigidity of the O′Bi_4 tetrahedra, or the fact that the RMC has a distribution of Bi displacements [Fig. 5.8(c)] whereas the circular model has strictly $r = 0.4$ Å. The separation between RMC and shuffled CSM points to rigidity that may be explained by correlated Bi displacements. Just as shuffling Bi displacements disrupts the ordering between

pairs of Bi as viewed by ϕ in Fig. 5.11(b), it also disrupts ordering between sets of *four* Bi displacements as viewed by CSM in Fig. 5.12(b).

5.4 Conclusions

This structural investigation of the strongly disordered pyrochlore $Bi_2Ti_2O_6O'$ benefits from modeling real- and reciprocal space structure simultaneously. The combination of Rietveld refinement, MEM, least-squares PDF refinement, and RMC simulations provide a description of the structure over many length scales. Of particular interest is the behavior of the displaced lone-pair active Bi^{3+} cation. Average structure models indicate a preference for static displacements. MEM and RMC show that Bi prefers the $96h$ (pointing between nearby O from the TiO_6 sublattice) rather than $96g$ sites (pointing toward neighboring O). Statistical measures of these displacements are extracted from RMC supercells.

RMC simulations show that Bi displacements lie at all angles θ in a ring normal to the O′–Bi–O′ bond with radius $r \sim 0.4$ Å, but there is a preference for θ corresponding to $96h$ positions. O′ atoms are centered on the ideal site, but in a tetrapodal shape with arms pointing away from neighboring Bi. Comparing the RMC result with an identical supercell with shuffled Bi displacements reveals that neighboring Bi displacements show some correlation with each other, with a

preference for $\phi = 180^\circ$ alignment. This corresponds to a zig-zag type ordering that merits further investigation. Measures of the tetrahedricity $S(T_d)$ of the O′Bi_4 sublattice indicate that neighboring displacements are weakly correlated, thus the sublattice may exhibit some rigidity. The results are consistent with the idea that these nonmagnetic lone-pair containing pyrochlore compounds can be regarded as highly *structurally* frustrated systems.

Chapter 6

Incoherent Bi off-centering in $Bi_2Ti_2O_6O'$ and $Bi_2Ru_2O_6O'$: Insulator versus metal

The previous chapter explained that oxides in the pyrochlore structure are often home to large atomic displacements of the A cation off its ideal position. This effect was seen also seen in Fourier maps of $La_2Zr_2O_7$ [175] and pyrochlores $Bi_2M_2O_7$ (B = Zn, Ru, Nb). [195, 200] In this chapter, the differences between insulating $Bi_2Ti_2O_6O'$ and metallic $Bi_2Ru_2O_6O'$ are examined with a focus on the difference in Bi displacements. While static displacements are present in both

samples, $Bi_2Ru_2O_6O'$ shows a much smaller effect. We attribute this to decreased ionicity of the Ru–O bond compared to Ti–O, and to screening conduction electrons in the metallic compound.

6.1 Introduction

Among $Bi_2^{3+}B_2O_7$ pyrochlores, B = Ti, Sn are insulators, while B = Ru, Rh, Ir, and Pt are metals. [201] The behavior of Bi^{3+} is starkly different in insulating versus metallic pyrochlores. In insulating $Bi_2Ti_2O_6O'$ the Bi is offset by 0.4 Å from the ideal site. Cubic $Bi_2Sn_2O_7$ is unstable below 900 K and transforms into a lower-symmetry cell. In both cases, the offcentering of Bi is analogous with the correlated motion of lone-pair-active Bi^{3+} in the ionic conductor Bi_2O_3 [202] or multiferroic $BiFeO_3$. [170] The metallic pyrochlores have smaller Bi displacements and have a slight volume contraction shown by Kennedy. [203] Theoretical studies have attributed static displacements (and lone pair activity) to hybridization of the Bi s state with O′ p orbitals near the Fermi energy.[204–206] Increased ionicity of the B cation (Ti or Sn) draws in charge from the 48f O, and Bi obtains a larger portion of its charge from O'. When the B–O bond is more covalent, the strength of the Bi–O′ bond is decreased and no off-centering is seen in calculations. However, Rietveld refinements show that Bi offcentering

is still present in experiment. [195, 207]

Here we present studies of insulating $Bi_2Ti_2O_6O'$ and metallic $Bi_2Ru_2O_6O'$ using pair distribution function (PDF) analysis with least-squares and reverse Monte Carlo (RMC) modeling. These techniques reveal the precise structural tendencies of Bi^{3+} off-centering, even in the case of incoherent ice-like disorder seen in $Bi_2Ti_2O_6O'$. [103] Specific details of bond distances, angles, and real-space shapes can be extracted from the large-box RMC model because it is predicated on fits to the atom-atom distances in the PDF.

6.2 Methods

Synthesis and a detailed average structural analysis of $Bi_2Ti_2O_6O'$ powder used in this study (including verification of purity) has been reported by Hector and Wiggin.[169] $Bi_2Ru_2O_6O'$ was prepared as single crystals by Tachibana [207] and ground prior to measurement. Time-of-flight (TOF) neutron powder diffraction was collected at the NPDF instrument at Los Alamos National Laboratory at 298 K and 14 K. NPDF is designed to collect high-resolution, high-momentum-transfer data suitable for production of the PDF, as well as traditional Rietveld refinement. We performed Rietveld refinement using GSAS.[53]. Extraction of the PDF with PDFGETN [8] used $Q_{max} = 35\,\text{Å}^{-1}$, and

least-squares refinements of the PDF were performed with PDFGUI.[10] Reverse Monte Carlo simulations were run using RMCPROFILE version 6. [18] on the HP Opteron QSR cluster at the California NanoSystems Institute. The densities of states (DOS) were produced using linear muffin-tin orbital calculations within the atomic sphere approximation using version 47C of the Stuttgart TB-LMTO-ASA program. [208] Bond valence sums (BVS) were extracted the RMC supercell as described in our previous work on $CuMn_2O_4$,[59] using the R_0 values of Brese and O'Keeffe.[56]

6.3 Results and discussion

Time-of-flight neutron diffraction Rietveld refinements for $Bi_2Ti_2O_6O'$ and $Bi_2Ru_2O_6O'$ at 14 K are shown in Fig. 6.1. These refinements were performed using the ideal pyrochlore model with unsplit Bi on the 16c sites and anisotropic atomic displacement parameters (ADPs). No siginificant differences were found from the the analysis of Hector [169] or Tachibana, [207] including the occupancy, with stoichiometric $Bi_2Ti_2O_6O'$ and a Bi occupancy of 0.97 for $Bi_2Ru_2O_6O'$. However, the strongest peak of $Bi_2Ti_2O_6O'$ (the $\{331\}$ reflection at $Q = 2.64$ Å^{-1}) is poorly fit. This is a consequence of significant diffuse intensity at its base. The diffuse scattering suggests that large atomic displacements exist

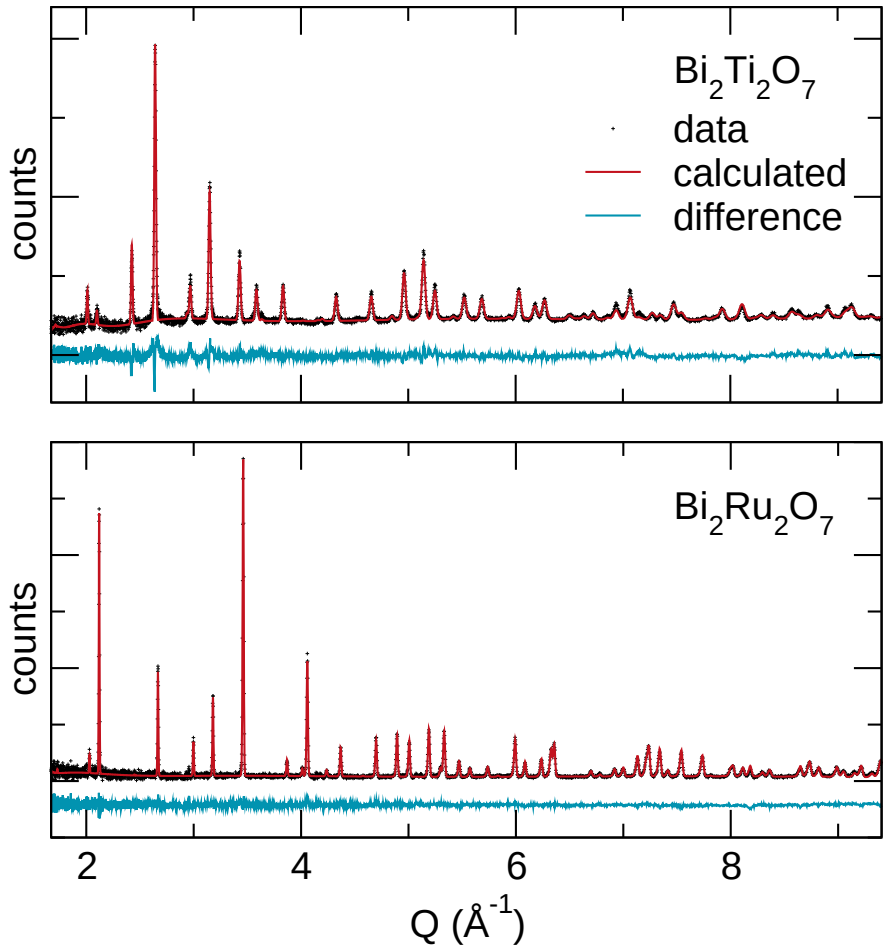

Figure 6.1: Time-of-flight neutron diffraction Rietveld refinement of $Bi_2Ti_2O_6O'$ (top) and $Bi_2Ru_2O_6O'$ (bottom) at 14 K using the ideal pyrochlore structure with anisotropic thermal parameters. The fit to $Bi_2Ti_2O_6O'$ is visibly worse due to large amounts of diffuse shoulder intensity. This diffuse scattering is a result of large local Bi and O′ displacements.

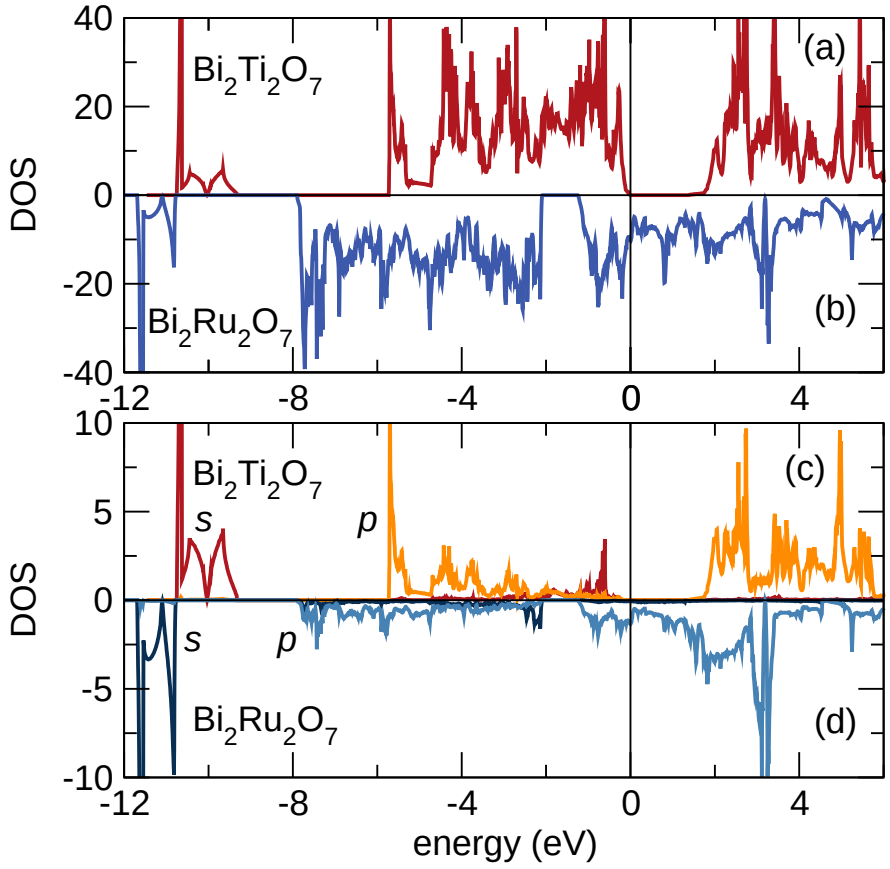

Figure 6.2: The computed total densities of states (DOS) (a,b) for $Bi_2Ti_2O_6O'$ and $Bi_2Ru_2O_6O'$. Below, Bi s (dark) and p (light) states are shown.

in the structure.

The total DOS for $Bi_2Ti_2O_6O'$ and $Bi_2Ru_2O_6O'$ are shown in Fig. 6.2(a,b). The features are similar, with metallic $Bi_2Ru_2O_6O'$ shifted approximately 2 eV downward. The partial Bi s and p DOS are shown in Fig. 6.2(b,c). In both cases, some Bi s states are present at the top of the filled Bi p and B d bands. Bi s states are

plotted as electron localization functions with 0.65 isosurfaces in Fig. 6.3(a,b). With Bi in their ideal 16c positions, the ELFs both show essentially identical lobes, corresponding to circularly averaged lone pairs. However, the ADPs from Rietveld refinement are distinctly different, seen below in Figs. 6.3(c,d).

For the sake of simplicity, each is represented as an *ideal* pyrochlore, with A cations centered on the 16c sites and O′ on the 8b sites. Atoms are shown as 80% ADP ellipsoids. The most obvious difference between the two structures is the large, disk-shaped ellipsoid representing Bi positions in $Bi_2Ti_2O_6O'$. Bi is known to be off-centered from the ideal 16c position in a ring normal to the O′–Bi–O′ bond. [103, 169, 187] The large anisotropic ADP of the Bi atoms envelops this ring. A split Bi position can be used to produce a better fit to the diffraction data. Our previous study found that there is a slight tendency for Bi to prefer the 96h positions.[103] This represents a six-fold splitting of the Bi into sites that are displaced ~ 0.4 Å from the ideal site, and pointing *between* nearby O atoms on 48f sites. Bi in $Bi_2Ru_2O_6O'$ is also anisotropic, with a slightly flattened ellipse.

The ELFs and ADPS in Fig. 6.3 seem, at first glance, to imply a circularly symmetric distribution of charge around each Bi. Because these calculations assume that Bi lies on its ideal site, the high symmetry of the unit cell prevents the true anisotropic charge density from being manifested in this model. In fact,

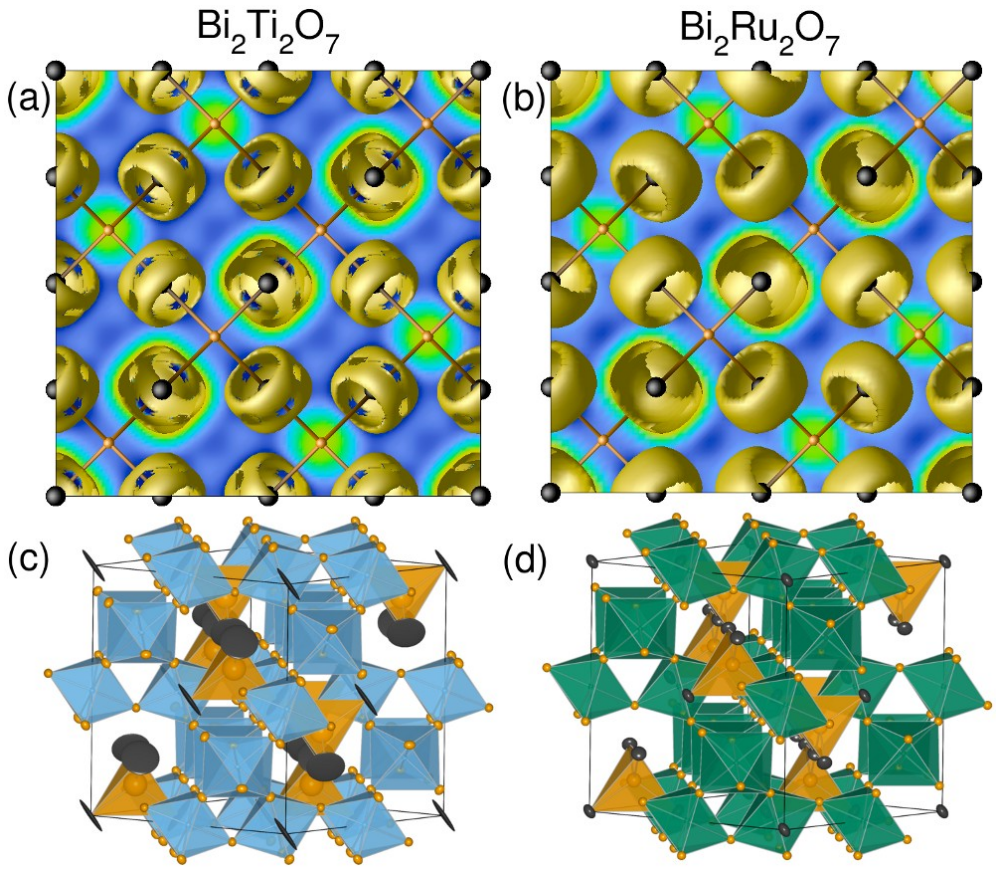

Figure 6.3: Electron localization functions (ELFs) for both compounds are shown in (a) and (b) as gold lobes around black Bi atoms. Both ideal structures show circles of lone pairs around Bi atoms. In (c) and (d), the unit cells from Rietveld refinement to neutron scattering data are shown with 80% ellipsoids. Bi = black, Ti = light blue, Ru = green, O = orange.

the lone pair in $Bi_2Ti_2O_6O'$ is displaced opposite the nucleus itself and each Bi offsets in a distinct direction. These offsets do not order over long ranges, so the disk seen in Fig. 6.3(c) envelops all possible orientations of the offset.

Average structural analysis of these disordered materials can only provide a partial view of the true structure. Both the average structure and ELFs show a Bi distribution that is symmetric around the O′–Bi–O′ bond (as required by $Fd\bar{3}m$). A better fit can be achieved using split Bi positions in the Rietveld refinement, but this does not reflect the fact that one Bi atom can only occupy one position. The ring itself is only manifested when a collection of discrete Bi positions is averaged over space.

Structural analysis of $Bi_2Ti_2O_6O'$ has shown that the ADP disk and split site are both poor approximations of the true structure and significantly more information can be gleaned by PDF analysis. [103]. We performed least-squares PDF refinements using the unit cells obtained by Rietveld refinement as a measure of agreement between the average and local structures. The fits for both compounds are shown in Fig. 6.4. Two issues should be considered. First, the fit for $Bi_2Ti_2O_6O'$ is significantly worse overall than $Bi_2Ru_2O_6O'$. This implies that the local structure of $Bi_2Ti_2O_6O'$ is poorly described by the $Fd\bar{3}m$ unit cell, while $Bi_2Ru_2O_6O'$ seems to be described fairly well. Second, the fit for $Bi_2Ti_2O_6O'$ is poorest at low r, which contains details of nearest-neighbor atomic distances (of

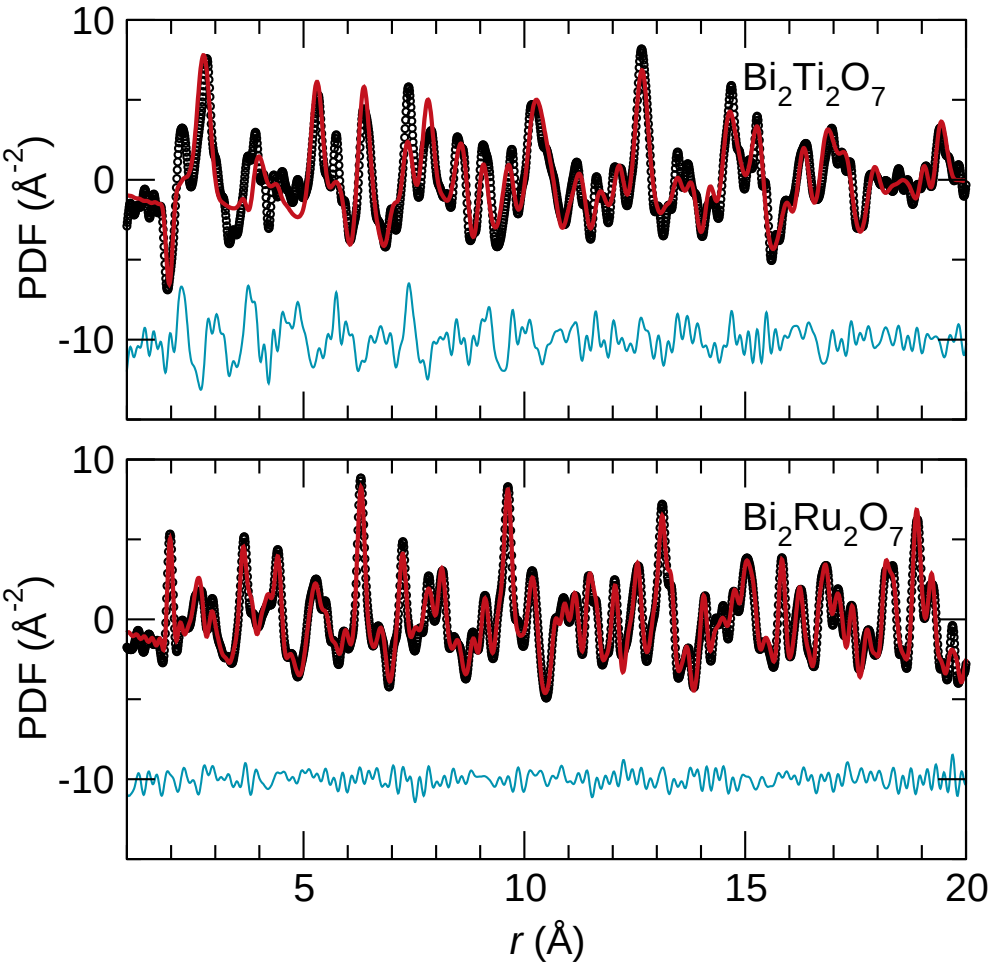

Figure 6.4: Least-squares PDF fits (using the unit cell from Rietveld refinement) do not reproduce the low-r structure of $Bi_2Ti_2O_6O'$ due to the inability of a small-box model to accommodate incoherent static displacements. The fit to $Bi_2Ru_2O_6O'$ is significantly better because the static displacements are smaller.

particular importance are Bi–O and Bi–O′). The fit improves at higher r because a larger number of pairs are being included. The fit for $Bi_2Ru_2O_6O'$ is equally decent at all r values up to 20 Å.

These fits do not give the exact positions of atoms in either compound. However, they quickly reveal valuable information about the *presence* of local atomic displacements (more apparent in $Bi_2Ti_2O_6O'$ than $Bi_2Ru_2O_6O'$) and the correlations between them (still unable to be averaged for $r < 20$ Å). Extracting structural tendencies of geometrically frustrated compounds via least-squares refinement is inherently difficult because there is no straightforward way to model the large, complex collection of discrete displacements need to reproduce the disorder. Least-squares is not a suitable algorithm for determining so many free Bi positions, especially when their interactions may be correlated. Instead, we remove symmetry constraints and use the large-box technique of reverse Monte Carlo to investigate how Bi are distributed within a large supercell.

The RMC fits to the PDF and Bragg intensity for $Bi_2Ru_2O_6O'$ are shown in Fig. 6.5. Reproduction of the PDF ensures that the pairwise distances between atoms are reasonable, while the Bragg pattern constrains the lattice parameters and average ADPs. The RMC algorithm is driven to find the best fit to data that can be allowed by the model. Its advantage lies in the ability to extract metrics of atomic correlations from the final supercell.

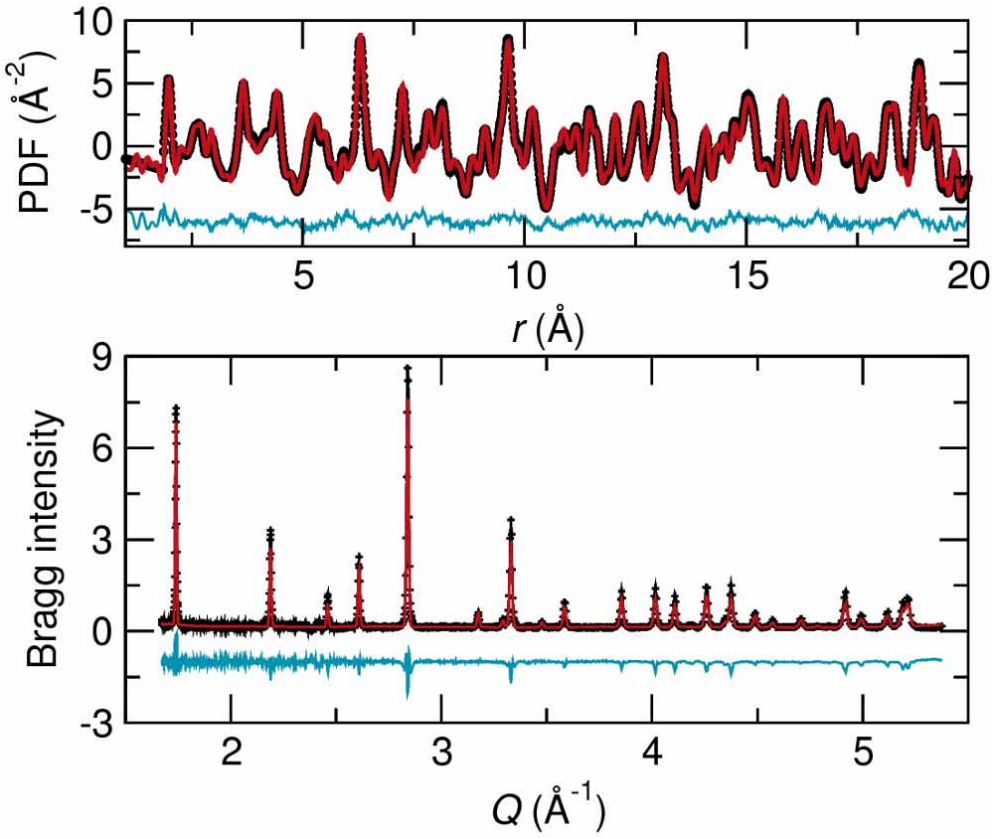

Figure 6.5: RMC fits to the PDF and Bragg profile of $Bi_2Ru_2O_6O'$ at 14 K constrain the local structure (atom–atom distances) and long-range periodicity (cell parameter, ADPs).

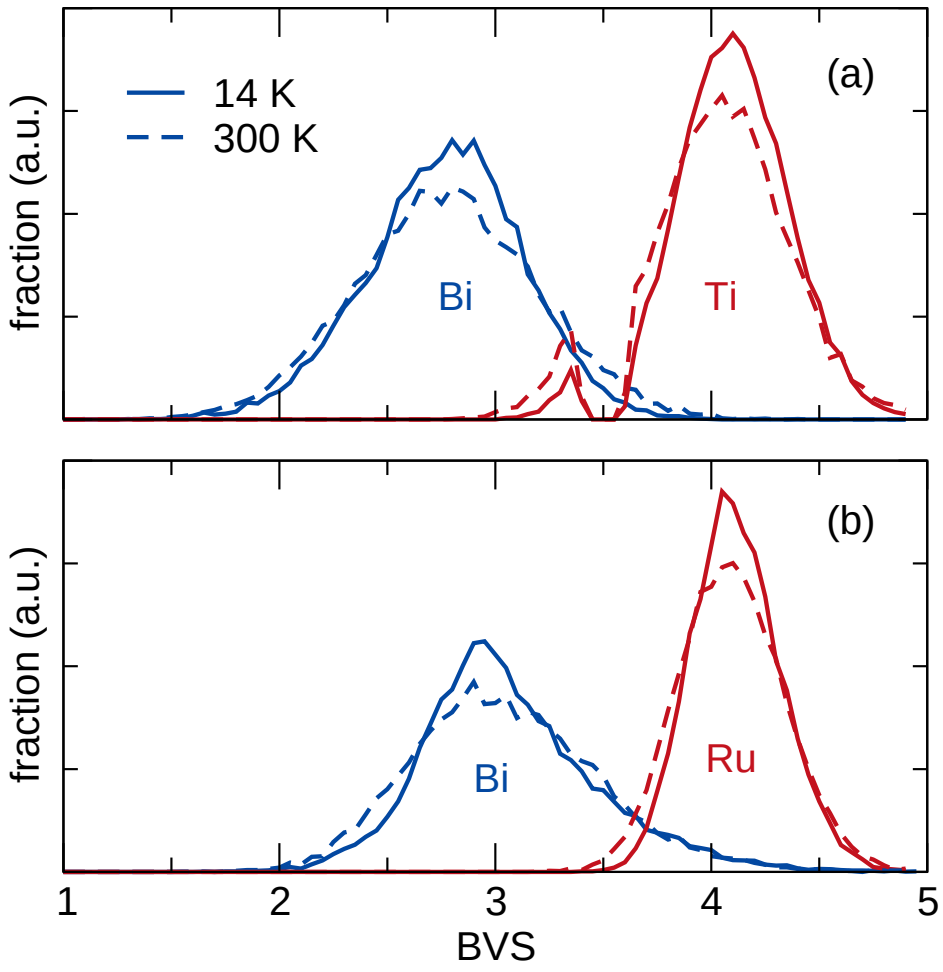

Figure 6.6: Bond valence sums (BVS) extracted from the RMC supercells show chemically reasonable bond lengths with entirely Bi^{3+}. The small shoulder of Ti^{3+} is a consequence of peak broadening. We expect only Ti^{4+} (note peak center) to exist in the sample.

Each supercell contains thousands of atoms of each type. Each Bi, for example, has a unique coordination of two O′ and six O 48f. Bond valence sums are calculated for each atom and a histogram of bond valence values is produced for each atom type. This histogram is normalized by stoichiometry and shown in Fig. 6.6 for $Bi_2Ti_2O_6O'$ and $Bi_2Ru_2O_6O'$ at T = 14 and 300 K. In all cases, only single values of the oxidations states are found: Bi^{3+}, Ti^{4+}, Ru^{4+}, and O^{2-}. A slight sharpening is seen for the low-temperature measurement. These distributions reveal that the RMC simulations contain chemically resonable bond lengths (no such constraints are applied during the simulation). They also reveal that there is no tendency for disproportionation to Bi^{5+}.

Folding the RMC supercell into a single unit cell produces "point clouds" of atoms at each crystallographic site. These clouds represent the tendency of an atom to displace from its ideal position. Taken in total, the mean squared displacement of points are in quantitative agreement with the average ADPs obtained from Rietveld refinement. These point clouds can be combined to create a probability distribution in two or three dimensions. Two-dimensional histograms (Fig. 6.7) show the tendency of Bi nuclei to offset in $Bi_2Ti_2O_6O'$ and $Bi_2Ru_2O_6O'$. The clouds are viewed normal to the O′–Bi–O′ bond (top) and perpendicular (bottom) for two temperatures.

The Bi ring in $Bi_2Ti_2O_6O'$ is clearly evident from Fig. 6.7 and has a diameter

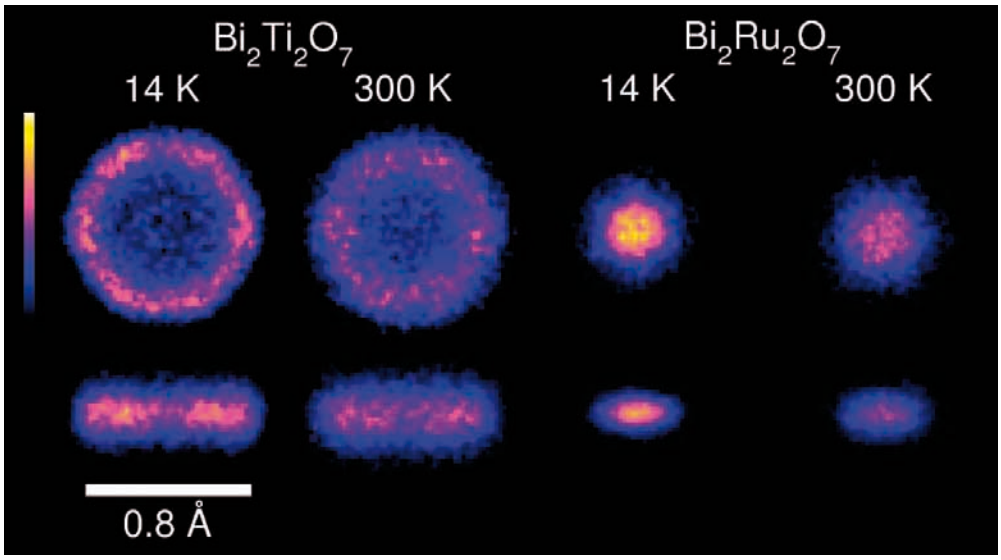

Figure 6.7: Clouds of Bi nuclear intensity for $Bi_2Ti_2O_6O$ and $Bi_2Ru_2O_6O$ are viewed along (top) and normal to (bottom) the O Bi O bond. Static disorder in both produces hexagonal ring or disk shapes centered on the ideal position.

of $\sim$0.8 Å. This is the distance between the nucleus and the lone pair. At 300 K, the ring is more diffuse. We attribute this to thermal broadening. There is no fundamental change in the shape or size of the ring. Interestingly, the ring is not a perfect circle. It has a slight hexagonal shape, with flat edges on the top and bottom. This six-fold symmetry corresponds to the tendency for Bi to occupy the 96h positions (corners of the hexagon), which point between the six neighboring 48f O atoms in the TiO_6 network.

The Bi distribution in $Bi_2Ru_2O_6O'$ is radically different. Probability is more densely clustered close to the ideal position and there is no obvious hollow center as in $Bi_2Ti_2O_6O'$. However, the perpendicular view reveals that the Bi distribution is still roughly disk-shaped. The disk is significantly wider than it is thick. Again, there is no fundamental change in the shape with temperature, only thermal broadening. Most surprising is the symmetry of the disk. It also has a hexagonal shape but the hexagon is rotated 30° with respect to $Bi_2Ti_2O_6O'$ with flat edges on the left and right, and corners on the top and bottom. This implies that Bi is displacing *toward* the nearby 48f O.

The hexagonal displacement of the Bi distributions can be probed quantitatively by plotting a histogram of the Bi nuclear density as a function of the angle θ around a ring normal to the O′–Bi–O′ bond. These curves are shown in Fig. 6.8. Both compounds show sixfold modulation, fit by a cosine curve with a

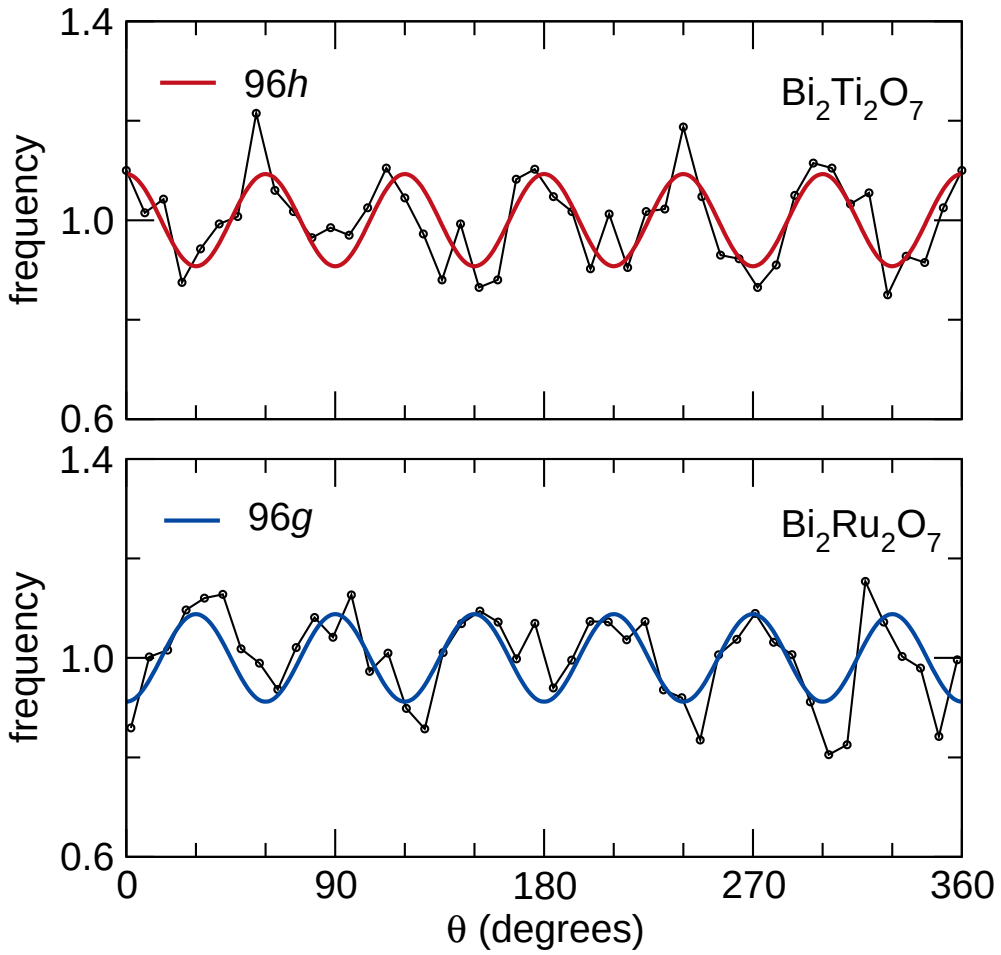

Figure 6.8: Bi symmetry around the ring normal to the O′–Bi–O′ bond reveals six-fold modulation for both compounds, but with opposite intensity. This implies a preference for 96h in $Bi_2Ti_2O_6O'$ and 96g in $Bi_2Ru_2O_6O'$.

period of 60°. However, their oscillations are offset by 30°. From the point of view of split sites in Rietveld refinement, this would refer to $96h$ positions for $Bi_2Ti_2O_6O'$ and $96g$ sites for $Bi_2Ru_2O_6O'$.

Reverse Monte Carlo fits to the PDF and Bragg profile show that $Bi_2Ti_2O_6O'$ and $Bi_2Ru_2O_6O'$ both exhibit Bi^{3+} off-centering with frustrated local dipoles. They are displaced in different directions (*between* versus *toward* the $48f$ O) and with different magnitudes. The differences should be reconciled by electronic structure. First, the Ti–O bonds are more strongly ionic than Ru–O due simply to electronegativity differences. Second, the metallic nature of $Bi_2Ru_2O_6O'$ produces mobile carriers that may cause charge screening. Hinojosa has proposed that Bi^{3+} in $Bi_2Ti_2O_6O'$ are displaced toward three $48f$ O and away from three others. [205] This would imply a $96g$ position, which is opposite our findings. This offcentering may help separate the Bi lone pair from $48f$ O. In $Bi_2Ru_2O_6O'$, covalent Ru–O (moreso than Ti–O) should increase the amount of Bi–O bonding and would decrease the Bi–O′ interactions that Walsh, *et al.* have claimed give rise to static displacments. [204] At the same time, metallic screening should decrease repulsion of the lone pair from nearby O $48f$ and loss of that rigidity should allow Bi to stay closer to the ideal position.

6.4 Conclusions

Significant progress remains to reconcile the electronic structure of these two compounds with their tendency for disorder on the OBi_4 sublattice and the differences in magnitude and direction of these displacements. As electronic structure calculations and scattering technqiues continue to improve, we expect a greater systematic understanding of the pyrochlores should emerge. Local structural analysis is a step in this direction, providing real-space maps of static displacements that solve the question of ambiguous $96g/96h$-type preference in $Bi_2Ti_2O_6O'$ and $Bi_2Ru_2O_6O'$.

Chapter 7

Summary and Future Directions

The work presented here has examined the nature of atomic disorder in polar and magnetic oxides with the intent of understanding their observable properties. Real-space analysis of crystal structures and RMC simulations are young techniques, and with each new system come new metrics of describing local atomic behavior. Statistical extraction and evaluation of these metrics is an ongoing process.

Since the RMC method can, in theory, accommodate any data that is calculable from the supercell, more exotic forms of data should find their way into analyses as the software is developed. Calculation of diffuse electron scattering intensity has been demonstrated on a qualitative level. [22] For polycrystalline

samples including $Bi_2Ti_2O_6O'$, this may be an invaluable way to probe correlated atomic displacements and short-range chemical order.

Increased computing power should enable convolution of the supercell structure with experimental broadening functions. This should solve the problem of modeling entire PDF peak widths using actual atomic positions in the unit cell. It should also aid simultaneous fits to X-ray and neutron PDFs, which is today hampered by their different resolution and attenuation. Addition of magnetic contributions to $S(Q)$ and Bragg profiles is in its infancy, but has been demonstrated as a proof of concept. [209]

There are only two published examples of RMCPROFILE fits to X-ray total scattering: bulk VO_2, [136] presented here, and an amorphous metal-organic framework. [21] This number is bound to increase soon due to fast measurements, temperature control, and small sample sizes allowed by synchrotron measurements.

Bibliography

[1] W. Friedrich, P. Knipping, and M. Laue. Interferenzerscheinungen bei röntgenstrahlen. *Ann. Physik*, 346(10):971–988, 1913.

[2] P. J. Mohr, B. N. Taylor, and D. B. Newell. CODATA recommended values of the fundamental physical constants: 2006. *Rev. Mod. Phys.*, 80(2):633, 2008.

[3] J. D. Watson and F. H. C. Crick. Molecular structure of nucleic acids: A structure for deoxyribose nucleic acid. *Nature*, 171(4356):737–738, 1953.

[4] H. M. Rietveld. A profile refinement method for nuclear and magnetic structures. *J. Appl. Crystallogr.*, 2:65–71, 1969.

[5] P. Debye. Zerstreuung von röntgenstrahlen. *Ann. Physik*, 351(6):809–823, 1915.

[6] T. R. Welberry. Diffuse x-ray scattering and models of disorder. *Rep. Prog. Phys.*, 48(11):1543, 1985.

[7] R. L. McGreevy and L. Pusztai. Reverse Monte Carlo simulation: A new technique for the determination of disordered structures. *Mol. Simulat.*, 1(6):359, 1988.

[8] P. F. Peterson, M. Gutmann, Th. Proffen, and S. J. L. Billinge. Pdfgetn: a user-friendly program to extract the total scattering structure factor and the pair distribution function from neutron powder diffraction data. *J. Appl. Cryst.*, 33:1192, 2000.

[9] X. Qiu, J. W. Thompson, and S. J. L. Billinge. PDFgetX2: a GUI-driven program to obtain the pair distribution function from x-ray powder diffraction data. *J. Appl. Cryst.*, 37(4):678, 2004.

[10] C. L. Farrow, P. Juhas, J. W. Liu, D. Bryndin, E. S. Bozin, J. Bloch, Th Proffen, and S. J. L. Billinge. Pdffit2 and pdfgui: computer programs for studying nanostructure in crystals. *J. Phys. Cond. Mat.*, 19:335219, 2007.

[11] X. Qiu, Th. Proffen, J. F. Mitchell, and S. J. L. Billinge. Orbital correlations in the pseudocubic O and rhombohedral R phases of $LaMnO_3$. *Phys. Rev. Lett.*, 94:177203–4, 2005.

[12] H.L. Anderson. Metropolis, Monte Carlo and the MANIAC. *Los Alamos Science*, (14):96–108, 1953.

[13] N. Metropolis, A. W. Rosenbluth, M. N. Rosenbluth, A. H. Teller, and E. Teller. Equation of state calculations by fast computing machines. *J. Chem. Phys.*, 21(6):1087, 1953.

[14] R. L. McGreevy and M. A. Howe. The structure of molten LiCl. *J. Phys. Cond. Mat.*, 1(49):9957, 1989.

[15] V. M. Nield, D. A. Keen, W. Hayes, and R. L. McGreevy. Structural changes in silver bromide at the melting point. *J. Phys. Cond. Mat.*, 4(32):6703, 1992.

[16] L. Pusztai and E. Svab. Modelling the structure of $Ni_{65}B_{35}$ metallic glass by reverse Monte Carlo simulation. *J. Phys. Cond. Mat.*, 5(47):8815, 1993.

[17] Th. Proffen and R. B. Neder. DISCUS: A program for diffuse scattering and defect-structure simulation. *J. Appl. Cryst.*, 30(2):171–175, 1997.

[18] M. G. Tucker, D. A. Keen, M. T. Dove, A. L. Goodwin, and Q. Hui. RMCProfile: reverse Monte Carlo for polycrystalline materials. *J. Phys. Cond. Mat.*, 19:335218, 2007.

[19] R. B. Neder and Th. Proffen. *Diffuse Scattering and Defect Structure Simulations: A Cook Book Using the Program DISCUS*. Oxford University Press, 2009.

[20] D. A. Keen. A comparison of various commonly used correlation functions for describing total scattering. *J. Appl. Cryst.*, 34:172–177, 2001.

[21] T. D. Bennett, A. L. Goodwin, M. T. Dove, D. A. Keen, M. G. Tucker, E. R. Barney, A. K. Soper, E. G. Bithell, J.-C. Tan, and A. K. Cheetham. Structure and properties of an amorphous metal-organic framework. *Phys. Rev. Lett.*, 104(11):115503, 2010.

[22] A. L. Goodwin, R. L. Withers, and H.-B. Nguyen. Real-space refinement of single-crystal electron diffuse scattering and its application to $Bi_2Ru_2O_{7-\delta}$. *J. Phys. Cond. Mat.*, 19(33):335216, 2007.

[23] J. G. Bednorz and K. A. Müller. Possible high T_c superconductivity in the Ba–La–Cu–O system. *Z. Phys. B.*, 64:189–193, 1986.

[24] R.M. Kusters, J. Singleton, D. A. Keen, R. McGreevy, and W. Hayes. Magnetoresistance measurements on the magnetic semiconductor $Nd_{0.5}Pb_{0.5}MnO_3$. *Physica B Cond. Mat.*, 155:362–365, 1989.

[25] S. Jin, T. H. Tiefel, M. McCormack, R. A. Fastnacht, R. Ramesh, and L. H.

Chen. Thousandfold change in resistivity in magnetoresistive La–Ca–Mn–O films. *Science*, 264:413–415, 1994.

[26] A. J. Millis, P. B. Littlewood, and B. I. Shraiman. Double exchange alone does not explain the resistivity of $La_{1-x}Sr_xMnO_3$. *Phys. Rev. Lett.*, 74:5144–5147, 1995.

[27] A. B. Lamb, C. C. Scalione, and G. Edgar. The preferential catalytic combustion of carbon monoxide in hydrogen. *J. Am. Chem. Soc.*, 44(4):738–757, 1922.

[28] S. Vepřek, D. L. Cocke, S. Kehl, and H. R. Oswald. Mechanism of the deactivation of hopcalite catalysts studied by XPS, ISS, and other techniques. *J. Catal.*, 100(1):250–263, 1986.

[29] D. Dollimore and K. H. Tonge. The constitution and oxidizing properties of materials in the copper (II) oxide–manganese (III) oxide system. *J. Chem. Soc. A*, pages 1728–1731, 1970.

[30] C. Jones, K. J. Cole, S. H. Taylor, M. J. Crudace, and G. J. Hutchings. Copper manganese oxide catalysts for ambient temperature carbon monoxide oxidation: Effect of calcination on activity. *J. Mol. Catal. A*, 305(1-2):121–124, 2009.

[31] A. Yoshiasa, Y. Inoue, F. Kanamaru, and K. Koto. Local structure and spin state of Co^{4+} ions in the perovskite-type $SrCo_{1-x}Mn_xO_3$ solid-solution. *J. Solid State Chem.*, 86(1):75–81, 1990.

[32] J. C. Mikkelsen and J. B. Boyce. Atomic-scale structure of random solid solutions: Extended x-ray-absorption fine-structure study of $Ga_{1-x}In_xAs$. *Phys. Rev. Lett.*, 49(19):1412, 1982.

[33] J. B. Boyce and J. C. Mikkelsen. Local structure of ionic solid solutions: Extended x-ray-absorption fine-structure study. *Phys. Rev. B*, 31(10):6903, 1985.

[34] J. B. Boyce and J. C. Mikkelsen. Local structure of pseudobinary semiconductor alloys: An x-ray absorption fine structure study. *J. Crys. Growth*, 98(1-2):37–43, 1989.

[35] J. Pellicer-Porres, A. Polian, A. Segura, V. Munoz-Sanjose, A. Di Cicco, and A. Traverse. X-ray-absorption fine-structure study of $ZnSe_xTe_{1-x}$ alloys. *J. Appl. Phys.*, 96(3):1491–1498, 2004.

[36] V. Petkov, I-K. Jeong, J. S. Chung, M. F. Thorpe, S. Kycia, and S. J. L. Billinge. High real-space resolution measurement of the local structure of $Ga_{1-x}In_xAs$ using x-ray diffraction. *Phys. Rev. Lett.*, 83(20):4089, 1999.

[37] P. F. Peterson, Th. Proffen, I.-K. Jeong, S. J. L. Billinge, K.-S. Choi, M. G. Kanatzidis, and P. G. Radaelli. Local atomic strain in $ZnSe_{1-x}Te_x$ from high real-space resolution neutron pair distribution function measurements. *Phys. Rev. B*, 63(16):165211, 2001.

[38] S. J. L. Billinge and I. Levin. The problem with determining atomic structure at the nanoscale. *Science*, 316:561–565, April 2007.

[39] X. Qiu, Emil S Božin, Pavol Juhas, Thomas Proffen, and Simon J. L Billinge. Reciprocal-space instrumental effects on the real-space neutron atomic pair distribution function. *J. Appl. Cryst.*, 37:110–116, 2004.

[40] J. B. Goodenough and A. L. Loeb. Theoretical model for the tetragonal-to-cubic phase transformations in transition metal spinels. *Phys. Rev.*, 116:32–45, 1955.

[41] L. E. Orgel and J. D. Dunitz. Stereochemistry of cupric compounds. *Nature*, 179:462–465, 1957.

[42] H. A. Jahn and E. Teller. Stability of polyatomic molecules in degenerate electronic states. i. orbital degeneracy. *Proc. R. Soc. A*, 161:220–235, 1937.

[43] P. J. Wojtowicz. Theoretical model for the tetragonal-to-cubic phase transformations in transition metal spinels. *Phys. Rev.*, 116:32–45, 1959.

[44] G. Felsenfeld. The structure of the chlorocuprate anion. *Proc. R Soc. (Lond.) A*, 236:506–514, 1956.

[45] A. P. B. Sinha, N. R. Sanjana, and A. B. Biswas. The crystal structure of copper manganite. *J. Phys. Chem.*, 62:191–194, 1958.

[46] R. Buhl. Manganites spinelles purs d'elements de transition preparations et structures cristallographiques. *J. Phys. Chem. Solids*, 30:805–812, 1969.

[47] G. G. Robbrecht and C. M. Henriet-Iserentant. On the lattice parameters and the tetragonal distortion of the copper and cadmium manganite systems. *Phys. Stat. Sol.*, 41:K43–K46, 1970.

[48] R. Metz, J. P. Caffin, R. Legros, and A. Rousset. The preparation, characterization and electrical properties of copper manganite spinels $Cu_xMn_{3-x}O_4$, $0 \leq x \leq 1$. *J. Mater. Sci.*, 24:83–87, 1989.

[49] B. Gillot, S. Buguet, and E. Kester. Oxidation mechanism and the valence states if copper and manganese in tetragonal $CuMn_2O_4$. *J. Mater. Chem.*, 7:2513–2517, 1997.

[50] F. C. M. Driessens and G. D. Rieck. Phase equilibria in the system cu–mn–o. *Z. Anorg. Allg. Chem.*, 351:48–62, 1967.

[51] Th. Proffen, T. Egami, S. J. L. Billinge, A. K. Cheetham, D. Louca, and J. B. Parise. Building a high resolution total scattering powder diffractometer – Upgrade of NPD at MLNSC. *Appl. Phys. A*, 74:S163–S165, 2002.

[52] J.-F. Bérar and G. Baldinozzi. XND code: From x-ray laboratory data to incommensurately modulated phases. Rietveld modelling of complex materials. *IUCr-CPD Newsletter*, 20:3–5, 1998.

[53] A.C. Larson and RB Von Dreele. General Structure Analysis System (GSAS). *Los Alamos National Laboratory Report LAUR*, 86:748, 2000.

[54] R. L. McGreevy. RMC: progress, problems and prospects. *Nucl. Instrum. Meth. A*, 354:1–16, 1995.

[55] R. L. McGreevy. Reverse Monte Carlo modelling. *J. Phys. Cond. Mat.*, 13:R877–R913, 2001.

[56] N. E. Brese and M. O'Keeffe. Bond-valence parameters for solids. *Acta Crys. B*, 47(2):192–197, 1991.

[57] Ju Li. AtomEye: an efficient atomistic configuration viewer. *Modelling and Simul. Mater. Sci. Eng.*, 11:173–177, 2003.

[58] K. Momma and F. Izumi. VESTA: a three-dimensional visualization system for electronic and structural analysis. *J. Appl. Cryst.*, 41:653–658, 2008.

[59] D. P. Shoemaker, J. Li, and R. Seshadri. Unraveling atomic positions in an oxide spinel with two Jahn–Teller ions: Local structure investigation of $CuMn_2O_4$. *J. Am. Chem. Soc*, 131(32):11450–11457, 2009.

[60] B. C. Melot, J. E. Drewes, R. Seshadri, E. M. Stoudenmire, and A. P. Ramirez. Magnetic phase evolution in the spinel compounds $Zn_{1-x}Co_xCr_2O_4$. *J. Phys. Condensed Matter*, 2009.

[61] P. F. Peterson, E. S. Bozin, Th. Proffen, and S. J. L. Billinge. Improved measures of quality for the atomic pair distribution function. *J. Appl. Cryst.*, 36:53–64, 2003.

[62] M. G. Tucker, D. A. Keen, J. S. O. Evans, and M. T. Dove. Local structure in ZrW_2O_8 from neutron total scattering. *J. Phys. Cond. Mat.*, 19:335215, 2007.

[63] N. N. Greenwood and A. Earnshaw. *Chemistry of the Elements, II Edn.* Butterworth-Heinemann, London, 1997.

[64] M. C. Day and J. Selbin. *Theoretical inorganic chemistry*. Rheinhold, New York, 1962.

[65] P. Steiner, V. Kinsinger, I. Sander, B. Siegwart, S. Hüfner, C. Politis, R. Hoppe, and H. P. Müller. The Cu valence in the high Tc superconductors and in monovalent, divalent and trivalent copper oxides determined from XPS core level spectroscopy. *Z. Phys. B*, 67(4):497–502, 1987.

[66] M. Lenglet, A. D'Huysser, J. Kasperek, J.P. Bonnelle, and J. Durr. Caracterisation des etats d'oxydation du cuiver et du manganese dans quelques manganites par analyse des spectres XPS, d'emission x et des seuils d'absorption x. *Mat. Res. Bull,*, 20(7):745–757, 1985.

[67] M Beley, L Padel, and J C Bernier. Studies and properties of copper manganese oxide $Cu_xMn_{3-x}O_4$ compounds with x = 1.0, 1.2, and 1.4. *Ann. Chim.*, 3:429–52, 1979.

[68] R. E. Vandenberghe, G. G. Robbrecht, and V. A. M. Brabers. Structure and ionic configuration of oxidic copper-manganese spinels ($Cu_xMn_{3-x}O_4$). *Phys. Status Solidi A*, 34:583–592, 1976.

[69] Piero Porta, Giuliano Moretti, Monica Musicanti, and Alessandro Nardella. Copper-manganese mixed oxides: formation, characterization

and reactivity under different conditions. *Solid State Ionics*, 63-65:257–267, 1993.

[70] K. Hestermann and R. Hoppe. Die kristallstruktur von $KCuO_2$, $RbCuO_2$ und $CsCuO_2$. *Z. Anorg. Allg. Chem.*, 367(5-6):249–260, 1969.

[71] R. Berger and L. Tergenius. Room temperature synthesis and structural characterization of monoclinic $LiCuO_2$ by X-ray and neutron diffraction. *J. Alloys and Comp.*, 203:203–207, 1994.

[72] S. D. Guest and J. W. Hutchinson. On the determinacy of repetitive structures. *J. Mech. Phys. Solids*, 51:383–391, 2003.

[73] Mark Pinsky and David Avnir. Continuous symmetry measures. 5. The classical polyhedra. *Inorg. Chem.*, 37(21):5575–5582, 1998.

[74] S. Alvarez, P. Alemany, D. Casanova, J. Cirera, M. Llunell, and D. Avnir. Shape maps and polyhedral interconversion paths in transition metal chemistry. *Coord. Chem. Rev.*, 249(17-18):1693–1708, 2005.

[75] J. G. Bednorz and K. A. Müller. Possible high T_c superconductivity in the Ba–La–Cu–O system. *Z. Phys. B.*, 64:189–193, 1986.

[76] E. Pavarini, I. Dasgupta, T. Saha-Dasgupta, O. Jepsen, and O. K. Ander-

sen. Band-structure trend in hole-doped cuprates and correlation with T_{cmax}. *Phys. Rev. Lett.*, 87(4):047003, 2001.

[77] H. A. Jahn and E. Teller. Stability of polyatomic molecules in degenerate electronic states. I. orbital degeneracy. *Proc. R. Soc. A*, 161:220–235, 1937.

[78] M. Gerloch. The sense of Jahn-Teller distortions in octahedral copper(II) and other transition-metal complexes. *Inorg. Chem.*, 20(2):638–640, 1981.

[79] E. Dagotto. *Nanoscale phase separation and colossal magnetoresistance: the physics of manganites and related compounds*. Springer, 2003.

[80] A. Sartbaeva, S. A. Wells, M. F. Thorpe, E. S. Božin, and S. J. L. Billinge. Quadrupolar ordering in $LaMnO_3$ revealed from scattering data and geometric modeling. *Phys. Rev. Lett.*, 99:155503–4, October 2007.

[81] J. B. Goodenough and A. L. Loeb. Theoretical model for the tetragonal-to-cubic phase transformations in transition metal spinels. *Phys. Rev.*, 116:32–45, 1955.

[82] R. Englman and B. Halperin. Cooperative dynamic Jahn-Teller effect. I. molecular field treatment of spinels. *Phys. Rev. B*, 2(1):75–94, 1970.

[83] M. Uehara, S. Mori, C. H. Chen, and S.-W. Cheong. Percolative phase separation underlies colossal magnetoresistance in mixed-valent manganites. *Nature*, 399:560–563, 1999.

[84] S. Yeo, Y. Horibe, S. Mori, C. M. Tseng, C. H. Chen, A. G. Khachaturyan, C. L. Zhang, and S.-W. Cheong. Solid state self-assembly of nanocheckerboards. *Appl. Phys. Lett.*, 89(23):233120, 2006.

[85] C. L. Zhang, S. Yeo, Y. Horibe, Y. J. Choi, S. Guha, M. Croft, S.-W. Cheong, and S. Mori. Coercivity and nanostructure in magnetic spinel $Mg(Mn,Fe)_2O_4$. *Appl. Phys. Lett.*, 90(13):133123, 2007.

[86] S. Park, Y. Horibe, T. Asada, L. S. Wielunski, N. Lee, P. L. Bonanno, S. M. O'Malley, A. A. Sirenko, A. Kazimirov, M. Tanimura, T. Gustafsson, and S.-W. Cheong. Highly aligned epitaxial nanorods with a checkerboard pattern in oxide films. *Nano Lett.*, 8(2):720–724, 2008.

[87] C. Leroux, A. Loiseau, D. Broddin, and G. Vantendeloo. Electron microscopy study of the coherent two-phase mixtures $L1_0$–$L1_2$, in Co–Pt alloys. *Phil. Mag. B*, 64:57–82, 1991.

[88] Y. Le Bouar, A. Loiseau, and A. G. Khachaturyan. Origin of chessboard-like structures in decomposing alloys. theoretical model and computer simulation. *Acta Mater.*, 46:2777–2788, 1998.

[89] P. Fratzl, O. Penrose, and J. L. Lebowitz. Modeling of phase separation in alloys with coherent elastic misfit. *J. Stat. Phys.*, 95:1429–1503, 1999.

[90] J. L. MacManus-Driscoll. Self-assembled heteroepitaxial oxide nanocomposite thin film structures: Designing interface-induced functionality in electronic materials. *Adv. Func. Mater.*, 20(13):2035–2045, 2010.

[91] Y. Kino and S. Miyahara. Crystal deformation of copper and nickel chromite system. *J. Phys. Soc. Japan*, 21:2732–2732, 1966.

[92] L. Q. Yan, Z. W. Jiang, X. D. Peng, L. H. He, and F. W. Wang. Powder x-ray diffraction and Rietveld analysis of $Cd_{1-x}Cu_xCr_2O_4 (0.1 \leq x \leq 0.7)$. *Powder Diffraction*, 22(4):340–343, 2007.

[93] L.-Q. Yan, F. Maciá, Z.-W. Jiang, J. Shen, L.-H. He, and F.-W. Wang. Glassy magnetic behavior induced by Cu^{2+} substitution in the frustrated antiferromagnet $ZnCr_2O_4$. *J. Phys. Cond. Mat.*, 20(25):255203, 2008.

[94] S. Waplak and W. Bednarski. Jahn-Teller glass formation in β-lithium ammonium sulfate monocrystals studied by means of the electron paramagnetic resonance of Mn^{2+} and Cu^{2+} ions. *J. Phys. Cond. Mat.*, 14(47):12529–12536, 2002.

[95] H.-J. Noh, S. Yeo, J.-S. Kang, C. L. Zhang, S.-W. Cheong, S.-J. Oh, and

P. D. Johnson. Jahn-Teller effect in spinel manganites probed by soft x-ray absorption spectroscopy. *Appl. Phys. Lett.*, 88(8):081911, 2006.

[96] Stefan T. Norberg, I. Ahmed, S. Hull, D. Marrocchelli, and P. A. Madden. Local structure and ionic conductivity in the $Zr_2Y_2O_7$-Y_3NbO_7 system. *J. Phys. Cond. Mat.*, 21:5401, 2009.

[97] O. Cambon, J. Haines, M. Cambon, D. A. Keen, M. G. Tucker, L. Chapon, N. K. Hansen, M. Souhassou, and F. Porcher. Effect of Ga content on the instantaneous structure of $Al_{1-x}Ga_xPO_4$ solid solutions at high temperature. *Chem. Mater.*, 21(2):237–246, 2009.

[98] S. Wells, M. T. Dove, and M. G. Tucker. Reverse Monte Carlo with geometric analysis - RMC+GA. *J. Appl. Cryst.*, 37(4):536–544, 2004.

[99] A. L. Goodwin, S. Redfern, M. T. Dove, D. A. Keen, and M. G. Tucker. Ferroelectric nanoscale domains and the 905 K phase transition in $SrSnO_3$: A neutron total-scattering study. *Phys. Rev. B*, 76(17), 2007.

[100] H. Zabrodsky, S. Peleg, and D. Avnir. Continuous symmetry measures. *J. Am. Chem. Soc.*, 114(20):7843–7851, 1992.

[101] S. Keinan and D. Avnir. Studies in copper(II) complexes: correlations be-

tween quantitative symmetry and physical properties. *J. Che. Soc., Dalton Trans.*, (6):941–947, 2001.

[102] K. M. Ok, P. S. Halasyamani, D. Casanova, M. Llunell, P. Alemany, and S. Alvarez. Distortions in octahedrally coordinated d^0 transition metal oxides: A continuous symmetry measures approach. *Chem. Mater.*, 18(14):3176–3183, 2006.

[103] Daniel P. Shoemaker, Ram Seshadri, Andrew L. Hector, Anna Llobet, Thomas Proffen, and Craig J. Fennie. Atomic displacements in the charge ice pyrochlore $Bi_2Ti_2O_6O'$ studied by neutron total scattering. *Phys. Rev. B*, 81(14):144113, 2010.

[104] A. Miller. Distribution of cations in spinels. *J. Appl. Phys.*, 30(4):S24, 1959.

[105] R. D. Shannon. Revised effective ionic radii and systematic studies of interatomic distances in halides and chalcogenides. *Acta Cryst. A*, 32(5):751–767, 1976.

[106] W. A. Dollase and H. St. C. O'Neill. The spinels $CuCr_2O_4$ and $CuRh_2O_4$. *Acta Cryst. C*, 53(6):657–659, 1997.

[107] N. N. Greenwood and A. Earnshaw. *Chemistry of the Elements, II Edn.* Butterworth-Heinemann, London, 1997.

[108] M. C. Day and J. Selbin. *Theoretical inorganic chemistry*. Rheinhold, New York, 1962.

[109] E. J. W. Verwey and E. L. Heilmann. Physical properties and cation arrangement of oxides with spinel structures I. Cation arrangement in spinels. *J. Chem. Phys.*, 15(4):174, 1947.

[110] B. J. Kennedy and Q. Zhou. The role of orbital ordering in the tetragonal-to-cubic phase transition in $CuCr_2O_4$. *J. Solid State Chem.*, 181(9):2227–2230, 2008.

[111] M. Tovar, R. Torabi, C. Welker, and F. Fleischer. Structural and magnetic properties of Cu-Ni-Cr spinel oxides. *Physica B*, 385-386:196–198, 2006.

[112] H. Ehrenberg, M. Knapp, C. Baehtz, and S. Klemme. Tetragonal low-temperature phase of $MgCr_2O_4$. *Powder Diffr.*, 17(3):230–233, 2002.

[113] S. Klemme and M. Ahrens. Low-temperature heat capacities of $MgAl_2O_4$ and spinels of the $MgCr_2O_4$–$MgAl_2O_4$ solid solution. *Phys. Chem. Minerals*, 34(2):59–72, 2007.

[114] L. Ortega-San-Martín, A. J. Williams, C. D. Gordon, S. Klemme, and J. P.

Attfield. Low temperature neutron diffraction study of $MgCr_2O_4$ spinel. *J. Phys. Cond. Mat.*, 20(10):104238, 2008.

[115] Z. Zhang, D. Louca, A. Visinoiu, S.-H. Lee, J. Thompson, T. Proffen, A. Llobet, Y. Qiu, S. Park, and Y. Ueda. Local order and frustration in the geometrically frustrated spinels $Cd1-xZn_xV_2O_4$. *Phys. Rev. B*, 74(1), 2006.

[116] D. Reinen, M. Atanasov, G. Nikolov, and F. Steffens. Local and cooperative Jahn-Teller distortions of Ni^{2+} and Cu^{2+} in tetrahedral coordination. *Inorg. Chem.*, 27(10):1678–1686, 1988.

[117] Y. Kino, B. Lüthi, and M. E. Mullen. Cooperative Jahn-Teller phase transition in the Nickel-Zinc-Chromite system. *J. Phys. Soc. Japan*, 33:687–697, 1972.

[118] M. O'Keeffe. Cation valencies and distributions in spinel structures containing manganese. *J. Phys. Chem. Solids*, 21(3-4):172–178, 1961.

[119] P. Holba, M. Nevriva, and E. Pollert. Tetragonal distortion of spinel solid solutions $MnCr_2O_4$–Mn_3O_4. *Mater. Res. Bull.*, 10(8):853–860, 1975.

[120] D. G. Wickham and W. J. Croft. Crystallographic and magnetic properties

of several spinels containing trivalent ja-1044 manganese. *J. Phys. Chem. Solids*, 7(4):351–360, 1958.

[121] G. T. Bhandage and H. V. Keer. Magnetic properties of the $ZnMn_2O_4$–$NiMn_2O_4$ system. *J. Phys. C Solid State Phys.*, 11:L219–L221, 1978.

[122] H.-P. Walter, I. Schulz, and J. Scheve. Magnetische untersuchungen am CuO/Cr_2O_3-katalysator. *Z. Anorg. Allg. Chem.*, 352(5-6):241–245, 1967.

[123] H. Shaked, J. M. Hastings, and L. M. Corliss. Magnetic structure of magnesium chromite. *Phys. Rev. B*, 1(7):3116–3124, 1970.

[124] W. H. Meiklejohn and C. P. Bean. New magnetic anisotropy. *Phys. Rev.*, 102(5):1413–1414, 1956.

[125] A. E. Berkowitz and Kentaro Takano. Exchange anisotropy – a review. *J. Magn. Magn. Mat.*, 200(1-3):552–570, 1999.

[126] J. Nogués, J. Sort, V. Langlais, V. Skumryev, S. Suriñach, J. S. Muñoz, and M. D. Baró. Exchange bias in nanostructures. *Physics Reports*, 422(3):65–117, 2005.

[127] S. A. Makhlouf, F. T. Parker, and A. E. Berkowitz. Magnetic hysteresis anomalies in ferritin. *Phys. Rev. B*, 55(22):R14717–R14720, 1997.

[128] B. Martínez, X. Obradors, Ll. Balcells, A. Rouanet, and C. Monty. Low temperature surface spin-glass transition in γ-Fe_2O_3 nanoparticles. *Phys. Rev. Lett.*, 80(1):181–184, 1998.

[129] M. Ali, P. Adie, C. H. Marrows, D. Greig, B. J. Hickey, and R. L. Stamps. Exchange bias using a spin glass. *Nat. Mater.*, 6(1):70–75, 2007.

[130] D. P. Shoemaker, E. E. Rodriguez, R. Seshadri, I. Sabaj Abumohor, and Th. Proffen. Intrinsic exchange bias in $Zn_xMn_{3-x}O_4$ ($x \leq 1$) solid solutions. *Phys. Rev. B*, 80(14):144422–9, 2009.

[131] V. A. M. Brabers. Cation migration, cation valencies and the cubic-tetragonal transition in $Mn_xFe_{3-x}O_4$. *J. Phys. Chem. Solids*, 32(9):2181–2191, 1971.

[132] E. S. Božin, M. Schmidt, A. J. DeConinck, G. Paglia, J. F. Mitchell, T. Chatterji, P. G. Radaelli, Th. Proffen, and S. J. L. Billinge. Understanding the insulating phase in colossal magnetoresistance manganites: Shortening of the Jahn-Teller long-bond across the phase diagram of $La_{1-x}Ca_xMnO_3$. *Phys. Rev. Lett.*, 98:137203–4, 2007.

[133] D. Louca and J. Sarrao. Dynamical disorder of spin-induced Jahn-Teller orbitals with the insulator-metal transition in cobaltites. *Phys. Rev. Lett.*, 91(15), 2003.

[134] V. F. Sears. Neutron scattering lengths and cross sections. *Neutron News*, 3(3):26, 1992.

[135] M. G. Tucker, M. P. Squires, M. T. Dove, and D. A. Keen. Dynamic structural disorder in cristobalite: neutron total scattering measurement and reverse Monte Carlo modelling. *J. Phys. Cond. Mat.*, 13(3):403–423, 2001.

[136] S. A. Corr, D. P. Shoemaker, B. C. Melot, and R. Seshadri. Real-Space investigation of structural changes at the metal-insulator transition in VO_2. *Phys. Rev. Lett.*, 105(5):056404, 2010.

[137] F. J. Morin. Oxides which show a metal-to-insulator transition at the Néel temperature. *Phys. Rev. Lett.*, 3:34–36, 1959.

[138] J. B. Goodenough. Direct cation–cation interactions in several oxides. *Phys. Rev.*, 117:1442–1451, 1960.

[139] C. N. Berglund and H. J. Guggenheim. Electronic properties of VO_2 near the semiconductor-metal transition. *Phys. Rev.*, 185:1022–1033, 1969.

[140] A. Zylbersztejn and N. F. Mott. Metal-insulator transition in vanadium dioxide. *Phys. Rev. B*, 11:4383–4395, 1975.

[141] M. Imada, A. Fujimori, and Y. Tokura. Metal-insulator transitions. *Rev. Mod. Phys.*, 70:1039–1263, 1998.

[142] J. M. Tomczak, F. Aryasetiawan, and S. Biermann. Effective band-structure in the insulating phase versus strong dynamical correlations in metallic VO_2. *Phys. Rev. B*, 78:115103, 2008.

[143] K. L. Holman, T. M. McQueen, A. J. Williams, T. Klimczuk, P. W. Stephens, H. W. Zandbergen, Q. Xu, F. Ronning, and R. J. Cava. Insulator to correlated metal transition in $V_{1-x}Mo_xO_2$. *Phys. Rev. B*, 79:245114, 2009.

[144] A. Cavalleri, M. Rini, H. H. W. Chong, S. Fourmaux, T. E. Glover, P. A. Heimann, J. C. Kieffer, and R. W. Schoenlein. Band-selective measurements of electron dynamics in VO_2 using femtosecond near-edge x-ray absorption. *Phys. Rev. Lett.*, 95(6):067405, Aug 2005.

[145] M. M. Qazilbash, M. Brehm, B.-G. Chae, P.-C. Ho, G. O. Andreev, B.-J. Kim, S. J. Yun, A. V. Balatsky, M. B. Maple, F. Keilmann, H.-T. Kim, and D. N. Basov. Mott transition in VO_2 revealed by infrared spectroscopy and nano-imaging. *Science*, 318:1750–1753, 2007.

[146] S. Shin, S. Suga, M. Taniguchi, M. Fujisawa, H. Kanzaki, A. Fujimori, H. Daimon, Y. Ueda, K. Kosuge, and S. Kachi. Vacuum-ultraviolet re-

flectance and photoemission study of the metal-insulator phase transitions in VO_2, V_6O_{13}, and V_2O_3. *Phys. Rev. B*, 41:4993–5009, 1990.

[147] P. Baum, D.-S. Yang, and A. H. Zewail. 4D visualization of transitional structures in phase transformations by electron diffraction. *Science*, 318:788, 2007.

[148] S. A. Corr, M. Grossman, J. D. Furman, B. C. Melot, A. K. Cheetham, K. R. Heier, and R. Seshadri. Controlled reduction of vanadium oxide nanoscrolls: Crystal structure, morphology, and electrical properties. *Chem. Mater.*, 20:6396, 2008.

[149] J. I. Sohn, H. J. Joo, D. Ahn, H. H. Lee, A. E. Porter, K. Kim, D. J. Kang, and M. E. Welland. Surface-stress-induced Mott transition and nature of associated spatial phase transition in single crystalline VO_2 nanowires. *Nano. Lett.*, 9:3392, 2009.

[150] S. Zhang, J. Y. Chou, and L. J. Lauhon. Direct correlation of structural domain formation with the metal insulator transition in a VO_2 nanobeam. *Nano. Lett.*, 9:4527, 2009.

[151] D. B. McWhan, M. Marezio, J. P. Remeika, and P. D. Dernier. X-ray diffraction study of metallic VO_2. *Phys. Rev. B*, 10:490–495, 1974.

[152] B. Poumellec, J. F. Marucco, and B. Touzelin. X-ray-absorption near-edge structure of titanium and vanadium in (Ti,V)O_2 rutile solid solutions. *Phys. Rev. B*, 35:2284–2294, 1987.

[153] G. Andersson. Studies on vanadium oxides. II. the crystal structure of vanadium dioxide. *Acta. Chem. Scand.*, 10:623–628, 1956.

[154] Ch. Leroux, G. Nihoul, and G. Van Tendeloo. From $VO_2(B)$ to $VO_2(R)$: Theoretical structures of VO_2 polymorphs and in situ electron microscopy. *Phys. Rev. B*, 57(9):5111–5121, Mar 1998.

[155] H. S. Choi, J. S. Ahn, J. H. Jung, T. W. Noh, and D. H. Kim. Mid-infrared properties of a VO_2 film near the metal-insulator transition. *Phys. Rev. B*, 54(7):4621–4628, Aug 1996.

[156] H.-T. Kim, Y. W. Lee, B.-J. Kim, B.-G. Chae, S. J. Yun, K.-Y. Kang, K.-J. Han, K.-J. Yee, and Y.-S. Lim. Monoclinic and correlated metal phase in VO_2 as evidence of the Mott transition: Coherent phonon analysis.

[157] V. Petkov. Nanostructure by high-energy x-ray diffraction. *Materials Today*, 11:28–38, 2008.

[158] P. J. Chupas, S. Chaudhuri, J. C. Hanson, X. Qiu, P. L. Lee, S. D. Shastri, S. J. L. Billinge, and C. P. Grey. Probing local and long-range structure

simultaneously: An in situ study of the high-temperature phase transition of α-AlF_3. *J. Am. Chem. Soc.*, 126:4756–4757, 2004.

[159] K. Page, T. Kolodiazhnyi, T. Proffen, A. K. Cheetham, and R. Seshadri. Local structural origins of the distinct electronic properties of Nb-substituted $SrTiO_3$ and $BaTiO_3$. *Phys. Rev. Lett.*, 101:205502, 2008.

[160] A. P. Hammersley. FIT2D: An introduction and overview. Technical report, European Synchrotron Radiation Facility, 1997.

[161] A. P. Ramirez. Strongly geometrically frustrated magnets. *Ann. Rev. Mater. Sci.*, 24:453–80, 1994.

[162] A. P. Ramirez, A. Hayashi, R. J. Cava, R. Siddharthan, and B. S. Shastry. Zero-point entropy in 'spin ice'. *Nature*, 399(6734):333–335, 1999.

[163] D. J. P. Morris, D. A. Tennant, S. A. Grigera, B. Klemke, C. Castelnovo, R. Moessner, C. Czternasty, M. Meissner, K. C. Rule, J.-U. Hoffmann, K. Kiefer, S. Gerischer, D. Slobinsky, and R. S. Perry. Dirac strings and magnetic monopoles in the spin ice $Dy_2Ti_2O_7$. *Science*, 326(5951):411–414, 2009.

[164] H. Kadowaki, N. Doi, Y. Aoki, Y. Tabata, T. J. Sato, J. W. Lynn, K. Mat-

suhira, and Z. Hiroi. Observation of magnetic monopoles in spin ice. *J. Phys. Soc. Japan*, 78:103706, 2009.

[165] S. Yonezawa, Y. Muraoka, and Z. Hiroi. New β-pyrochlore oxide superconductor $CsOs_2O_6$. *J. Phys. Soc. Japan*, 73:1655–1656, 2004.

[166] C. A. Kendziora, I. A. Sergienko, R. Jin, J. He, V. Keppens, B. C. Sales, and D. Mandrus. Goldstone-mode phonon dynamics in the pyrochlore $Cd_2Re_2O_7$. *Phys. Rev. Lett.*, 95(12):125503, 2005.

[167] S. Onoda and N. Nagaosa. Spin chirality fluctuations and anomalous Hall effect in itinerant ferromagnets. *Phys. Rev. Lett.*, 90(19):196602, 2003.

[168] R. Seshadri. Lone pairs in insulating pyrochlores: Ice rules and high-k behavior. *Solid State Sci.*, 8(3-4):259–266, 2006.

[169] A. L. Hector and S. B. Wiggin. Synthesis and structural study of stoichiometric $Bi_2Ti_2O_7$ pyrochlore. *J. Solid State Chem.*, 177(1):139–145, 2004.

[170] N. A. Hill. Density functional studies of multiferroic magnetoelectrics. *Ann. Rev. Mater. Res.*, 32(1):1–37, 2002.

[171] B. C. Melot, R. Tackett, J. O'Brien, A. L. Hector, G. Lawes, R. Seshadri,

and Arthur P. Ramirez. Large low-temperature specific heat in pyrochlore $Bi_2Ti_2O_7$. *Phys. Rev. B*, 79(22):224111–5, 2009.

[172] C. J. Fennie, R. Seshadri, and K. M. Rabe. Lattice instabilities in cubic pyrochlore $Bi_2Ti_2O_7$. *0712.1846*, 2007.

[173] R. L. Withers, T. R. Welberry, A. -K. Larsson, Y. Liu, L. Norn, H. Rundlf, and F. J. Brink. Local crystal chemistry, induced strain and short range order in the cubic pyrochlore $(Bi_{1.5-\alpha}Zn_{0.5-\beta})(Zn_{0.5-\gamma}Nb_{1.5-\delta})O_{(7-1.5\alpha-\beta-\gamma-2.5\delta)}$ (BZN). *J. Solid State Chem.*, 177(1):231–244, 2004.

[174] Y. Liu, R. L. Withers, H. B. Nguyen, K. Elliott, Q. Ren, and Z. Chen. Displacive disorder and dielectric relaxation in the stoichiometric bismuth-containing pyrochlores, $Bi_2M^{III}NbO_7$ (M=In and Sc). *J. Solid State Chem.*, 182(10):2748–2755, 2009.

[175] Y. Tabira, R. L. Withers, T. Yamada, and N. Ishizawa. Annular dynamical disorder of the rare earth ions in a $La_2Zr_2O_7$ pyrochlore via single crystal synchrotron x-ray diffraction. *Z. Kristallogr.*, 216(2):92–98, 2001.

[176] M. G. Tucker, M. T. Dove, and D. A. Keen. Application of the reverse Monte Carlo method to crystalline materials. *J. Appl. Cryst.*, 34(5):630–638, 2001.

[177] S. Adams and J. Swenson. Bond valence analysis of reverse Monte Carlo produced structural models; a way to understand ion conduction in glasses. *J. Phys. Cond. Mat.*, 17:S87–S101, 2005.

[178] D. Yogev-Einot and D. Avnir. Pressure and temperature effects on the degree of symmetry and chirality of the molecular building blocks of low quartz. *Acta Cryst. B*, 60(2):163–173, 2004.

[179] J. D. Bernal and R. H. Fowler. A theory of water and ionic solution, with particular reference to hydrogen and hydroxyl ions. *J. Chem. Phys.*, 1(8):515–548, 1933.

[180] G. Kresse and J. Hafner. Ab initio molecular dynamics for liquid metals. *Phys. Rev. B*, 47(1):558–561, 1993.

[181] G. Kresse and J. Furthmüller. Efficient iterative schemes for ab initio total-energy calculations using a plane-wave basis set. *Phys. Rev. B*, 54(16):11169–11186, 1996.

[182] P. Blöchl. Projector augmented-wave method. *Phys. Rev. B*, 50(24):17953–17979, 1994.

[183] G. Kresse and D. Joubert. From ultrasoft pseudopotentials to the projector augmented-wave method. *Phys. Rev. B*, 59(3):1758–1775, 1999.

[184] Bilbao crystallographic server. http://www.cryst.ehu.es.

[185] D. M. Hatch H. T. Stokes and B. J. Campbell. Isotropy, 2007. http://stokes.byu.edu/isotropy.html.

[186] F. Izumi and A. Dilanian. *Recent Research Developments in Physics*, volume 3. Transworld Research Network, Trivandrum, India, 2002.

[187] I. Radosavljevic, J. S. O. Evans, and A. W. Sleight. Synthesis and structure of pyrochlore-type bismuth titanate. *J. Solid State Chem.*, 136(1):63–66, 1998.

[188] I. Radosavljevic Evans, J. A. K. Howard, and J. S. O. Evans. α-$Bi_2Sn_2O_7$–a 176 atom crystal structure from powder diffraction data. *J. Mater. Chem.*, 13(9):2098–2103, 2003.

[189] J. Cagnon, D. S. Boesch, N. H. Finstrom, S. Z. Nergiz, S. P. Keane, and S. Stemmer. Microstructure and dielectric properties of pyrochlore $Bi_2Ti_2O_7$ thin films. *J. Appl. Phys.*, 102(4):044102–5, 2007.

[190] E. T. Jaynes. Information theory and statistical mechanics. *Phys. Rev.*, 106(4):620, 1957.

[191] E. T. Jaynes. Information theory and statistical mechanics. II. *Phys. Rev.*, 108(2):171, 1957.

[192] M. Sakata and M. Sato. Accurate structure analysis by the maximum-entropy method. *Acta Cryst. A*, 46(4):263–270, 1990.

[193] M. Sakata, R. Mori, S. Kumazawza, M. Takata, and H. Toraya. Electron-density distribution from x-ray powder data by use of profile fits and the maximum-entropy method. *J. Appl. Cryst.*, 23(6):526–534, 1990.

[194] S. Kumazawa, Y. Kubota, M. Takata, M. Sakata, and Y. Ishibashi. MEED: a program package for electron-density-distribution calculation by the maximum-entropy method. *J. Appl. Cryst.*, 26(3):453–457, 1993.

[195] M. Avdeev, M. K. Haas, J. D. Jorgensen, and R. J. Cava. Static disorder from lone-pair electrons in $Bi_{2-x}M_xRu_2O_{7-y}$ (M=Cu,Co; x=0,0.4) pyrochlores. *J. Solid State Chem.*, 169(1):24–34, 2002.

[196] Y. Tabira, R. Withers, J. Thompson, and S. Schmid. Structured diffuse scattering as an indicator of inherent cristobalite-like displacive flexibility in the rare earth zirconate pyrochlore $La_\delta Zr_{1-\delta}O_{2-\delta/2}$, $0.49 < \delta < 0.51$. *J. Solid State Chem.*, 142(2):393–399, 1999.

[197] B. Nguyen, Y. Liu, and R. L. Withers. The local crystal chemistry and dielectric properties of the cubic pyrochlore phase in the $Bi_2O_3M^{2+}ONb_2O_5$ (M^{2+} =Ni^{2+} and mg^{2+}) systems. *J. Solid State Chem.*, 180(2):549–557, 2007.

[198] R. Withers, J. Thompson, and T. Welberry. The structure and microstructure of α-cristobalite and its relationship to β-cristobalite. *Phys. Chem. Miner.*, 16(6):517–523, 1989.

[199] Th. Proffen and T. R. Welberry. Analysis of diffuse scattering via the reverse Monte Carlo technique: a systematic investigation. *Acta Cryst. A*, 53(2):202–216, 1997.

[200] T. A. Vanderah, I. Levin, and M. W. Lufaso. An unexpected crystal-chemical principle for the pyrochlore structure. *European Journal of Inorganic Chemistry*, 2005(14):2895–2901, 2005.

[201] M. A. Subramanian, G. Aravamudan, and G. V. Subba Rao. Oxide pyrochlores – a review. *Prog. Solid State Chem.*, 15(2):55–143, 1983.

[202] Comparison of short-range ion-ion correlations in the α, β and δ phases of Bi_2O_3. 2010.

[203] B. J. Kennedy. Structural trends in Bi containing pyrochlores: The structure of $Bi_2Rh_2O_{7-\delta}$. *Mater. Res. Bull.*, 32(5):479–483, 1997.

[204] A. Walsh, G. W. Watson, D. J. Payne, R. G. Edgell, J. Guo, P. Glans, T. Learmonth, and K. E. Smith. Electronic structure of the α and δ phases of

Bi_2O_3: A combined ab initio and x-ray spectroscopy study. *Phys. Rev. B*, 73(23):235104, 2006.

[205] B. Brooks Hinojosa, J. C. Nino, and A. Asthagiri. First-principles study of cubic Bi pyrochlores. *Phys. Rev. B*, 77(10):104123–14, 2008.

[206] B. Brooks Hinojosa, P. M. Lang, and A. Asthagiri. The influence of sulfur substitution on the atomic displacement in $Bi_2Ti_2O_7$. *J. Solid State Chem.*, 183(1):262–269, 2010.

[207] M. Tachibana, Y. Kohama, T. Shimoyama, A. Harada, T. Taniyama, M. Itoh, H. Kawaji, and T. Atake. Electronic properties of the metallic pyrochlore ruthenates $Pb_2Ru_2O_{6.5}$ and $Bi_2Ru_2O_7$. *Phys. Rev. B*, 73(19):193107, 2006.

[208] O. Jepsen and O. K. Andersen. The Stuttgart TB-LMTO-ASA program version 47. *MPI für Festkörperforschung, Stuttgart, Germany*, 2000.

[209] A. L. Goodwin, M. G. Tucker, M. T. Dove, and D. A. Keen. Magnetic structure of MnO at 10 K from total neutron scattering data. *Physical Review Letters*, 96(4):047209, 2006.